UNIVERSIDADE DE SÃO PAULO
INSTITUTO DE FÍSICA DE SÃO CARLOS

Lucas Vieira Pupim

Chiral Majoranas morphing into corner states in ordinary QAH/SC systems

São Carlos

2022

Lucas Vieira Pupim

Chiral Majoranas morphing into corner states in ordinary QAH/SC systems

Dissertation presented to the Graduate Program in Physics at the Instituto de Física de São Carlos da Universidade de São Paulo, to obtain the degree of Master in Science.

Concentration area: Theoretical and Experimental Physics

Advisor: Prof. Dr. José Carlos Egues de Menezes

Corrected version
(Original version available on the Program Unit)

São Carlos
2022

I AUTHORIZE THE REPRODUCTION AND DISSEMINATION OF TOTAL OR PARTIAL COPIES OF THIS DOCUMENT, BY CONVENTIONAL OR ELECTRONIC MEDIA FOR STUDY OR RESEARCH PURPOSE, SINCE IT IS REFERENCED.

Pupim, Lucas
Chiral Majoranas morphing into corner states in ordinary QAH/SC systems / Lucas Pupim; advisor J. Carlos Egues - corrected version -- São Carlos 2022.
95 p.

Dissertation (Master's degree - Graduate Program in Theoretical and Experimental Physics) -- Instituto de Física de São Carlos, Universidade de São Paulo - Brasil , 2022.

1. Majorana fermion. 2. Topological superconductivity. 3. High-order topological superconductivity. 4. Majorana corner states. I. Egues, J. Carlos, advisor. II. Title.

Ao meu avô Milton, que foi ver se eu estava ali na esquina. (in memoriam)

ACKNOWLEDGEMENTS

Gostaria de começar estes agradecimentos me desculpando. Me desculpo porque não consegui encontrar (às vezes eu me convenço de que não existe) uma combinação de palavras que seja fidedigna à gratidão que sinto pelas pessoas que discriminarei em seguida.

Agradeço à minha família, na qual sempre encontro conforto e inspiração. Em especial, aos meus pais por seu carinho e apoio incondicional, e ao meu irmão por sempre me alegrar com sua companhia. Acredito que seja impossível retribuir todo o amor que recebi e recebo. De toda forma, essa é uma dívida da qual não pretendo me desfazer, espero poder retribuir em longas prestações.

Para meus amigos, roubo um punhado de palavras da última carta de Goethe: “Sem dúvida nenhuma teria imenso prazer em dedicar e transmitir esses gracejos muito sérios aos meus caros amigos, que agradecidamente reconheço existirem em grande número e em muitos recantos, já da para sentir a sua reação e receptividade.” De particular importância para que estes gracejos muito sérios (aviso que nas páginas abaixo não há nenhum Fausto) existam, destaco quatro que me acompanharam de maneira muito próxima durante essa jornada: Arthur, Aurélio, Rodrigo e Wilson.

Num lugar de fundamental importância para esse período de muito aprendizado e amadurencimento se encontram duas pessoas as quais sou grato: meu orientador José Carlos Egues e nosso colaborador Matthew Gilbert. Aprendi muito sob a supervisão de ambos; além de física, tive a oportunidade de aprender imensamente sobre como expressar as minhas ideias, e sobre boas práticas acadêmicas e científicas. Por motivos muito semelhantes, também gostaria de agradecer aos demais membros do grupo de São Carlos (Poliana, Warlley, Julian e Ronaldo), com os quais sempre pude contar para grandes (enormes) discussões.

Por último, mas não menos importante, gostaria de agradecer ao Mauro, que se encontra em algum lugar razoavelmente engraçado entre familiar, amigo e mentor. Agradeço por sua incrível determinação e competência para ajudar pessoas. Qualidades das quais sou testemunha em primeira mão.

“Esta reflexión me animó, y luego me infundió una especie de vértigo. En el ámbito de la tierra hay formas antiguas, formas incorruptibles y eternas; cualquiera de ellas podía ser el símbolo buscado. Una montaña podía ser la palabra del dios, o un río o el imperio o la configuración de los astros. Pero en el curso de los siglos las montañas se allanan y el camino de un río suele desviarse y los imperios conocen mutaciones y estragos y la figura de los astros varía. En el firmamento hay mudanza. La montaña y la estrella son individuos, y los individuos caducan. Busqué algo más tenaz, más invulnerable.”

Jorge Luis Borges

ABSTRACT

PUPIM, L. **Chiral Majoranas morphing into corner states in ordinary QAH/SC systems**. 2022. 95p. Dissertation (Master in Science) - Instituto de Física de São Carlos, Universidade de São Paulo, São Carlos, 2022.

Today, the realization of Majorana states is one of the most sought after results in condensed matter. The focused attention on this issue comes from the desire of using these states to create robust topological quantum computers. This quest may be accomplished through many paths as there are several proposals for Majorana platforms. One of the most recent paths involves high-order topological superconductivity. Here, we study a junction formed by a quantum anomalou Hall system and an s-wave superconductor, known for hosting chiral Majorana edge states, and show that by tuning parameters this system can exhibit a 2^{nd}-order phase with Majorana corner states. We model this system via a single Dirac cone describing the surface state of a 3D topological insulator in close proximity to a superconductor. We characterize this system through the lens of the symmetries of the Hamiltonian and electronic transport within the non-equilibrium Green's function formalism. Our results extend the previous analysis from Qi *et al.* (1), which only found first-order topological phases in a similar system. We show that four Majorana corner states can emerge our QAH-SC setup within the previously proposed chiral phase. In addition, we conjecture that these corner states are correlated to the formation of "domain walls" in the pairing function due to the presence of boundaries (edges *and* corner). We also show that these states are protected by a pair of magnetic mirror symmetries. Moreover, in the absence of a topological invariant to characterize this high-order phase, we determine an effective phase diagram for our finite system by looking at the zero-bias conductance peaks. Through a characteristic e^2/h zero-bias peak and looking at the lowest energy states wave-function, we find a wide region in the (μ, Δ) parameter space corresponding to the 2^{nd}-order phase with Majorana corner states. This work extends our knowledge not only about this particular model Hamiltonian but also about how we can find high-order topological superconductor phases.

Keywords: Majorana fermion. Topological superconductivity. High-order topological superconductivity. Majorana corner states.

RESUMO

PUPIM, L. **Transformando Majoranas quirais em *corner states* em sistemas QAH/SC ordinários**. 2022. 95p. Dissertação (Mestrado em Ciência) - Instituto de Física de São Carlos, Universidade de São Paulo, São Carlos, 2022.

Hoje, a criação de estados de Majorana é um dos resultados mais procurados em matéria condensada. A grande atenção para essa questão decorre da ideia de usar esses estados para a criação de um computador quântico topológico. Existem diversos caminhos para completar essa missão, uma vez que existem diversas plataformas para os estados de Majorana. Um dos caminhos mais recente envolve supercondutividade topológica de alta ordem. Neste trabalho, nós estudamos a junção entre uma superfície no regime de efeito Hall quântico anômalo (QAH) e um supercondutor (SC) do tipo s, conhecida por possuir estados quirais de Majorana nas bordas, e mostramos que variando os parâmetros desse sistema, ele exibe uma fase topológica de segunda ordem com *Majorana corner states*. Nós modelamos esse sistema através de um único cone de Dirac descrevendo o estado de superfície de um isolante topológico 3D em proximidade com um supercondutor. Através da análise das simetrias do Hamiltoniano e propriedades do transporte eletrônico usando o formalismo das funções de Green de não-equilíbrio, nós caracterizamos esse sistema. Nossos resultados estendem a análise feita por Qi *et al.* (1), que encontrou apenas fases de primeira ordem em um sistema similar. Mostramos que quatro *Majorana corner states* emergem no nosso sistema, dentro da fase ordinária proposta anteriormente. Além disso, nós conjecturamos que esses estados estão correlacionados com a formação de domínios de massa na função de pareamento do supercondutor devido a presença de bordas (arestas e vértices). Nós também mostramos que esses estados são protegidos por um par de simetrias de reflexão magnética. Além disso, na ausência de um invariante topológico para caracterizar essa fase de alta ordem, nós determinamos um diagrama de fases efetivo para o nosso sistema finito através de picos de condutância em *zero-bias*. Através de um pico caracteristico de e^2/h e do perfil da função de onda, encontramos uma região larga no espaço de parâmetros (μ, Δ) que corresponde a fase de segunda ordem com *Majorana corner states*. Além do conhecimento sobre este particular Hamiltoniano, este trabalho estende nosso conhecimento sobre como obter supercondutores topológicos de alta ordem.

Palavras-chave:Férmion de Majorana. Supercondutividade topológica. Supercondutividade topológica de alta ordem. Majorana corner states.

LIST OF FIGURES

Figure 1 – Number of times that the term “Majorana” was used either in the abstract or title in APS journals over a given period of time. The white part of the 2020-2024 bar is a projection (through an exponential fitting) for the next couple of years. Source: By the author. 21

Figure 2 – Diagram of two nonequivalent braid operations between two Majorana states. If we braid the “strings”, the left operation ends up crossed “strings”, while the right operation will have the “strings” separated. Source: By the author. 22

Figure 3 – Schematic of a 2D system showing the usual “prescription” to engineer a HOTSC phase with Majorana corner states. The idea is to gap out edge states with an anisotropic gap, such that the mass gaps have opposite signs along adjacent edges, thus forming domain walls. Source: By the author. 25

Figure 4 – Panels **a.** and **b.** show, respectively, the spatial probability density $|\psi_{BdG}(\vec{r})|^2$ of the lowest energy eigenstates and the real phase $\varphi(r)$ of our calculated pairing gap $|\langle c_{\uparrow,\vec{r}}\, c_{\downarrow,\vec{r}}\rangle| e^{i\varphi(r)}$ for distinct points in the phase-diagram **d.**. As one moves along the black dashed arrow (see symbols), the four lowest energy chiral Majorana modes (lowest plane in a.) evolve into four fully localized MCSs at zero energy. The probability densities of the MCSs strongly correlate with the emergence of the phase domains, cf. topmost planes in **a.** and **b.**. **c.** Schematic of our square-shaped QAH-SC setup with one corner source (S) and three corner drains (D). The arrows indicate the allowed transport processes, i.e., direct tunneling and (local) Andreev reflection. **d.** Zero-bias conductance $\mathcal{G}$ map as an effective (μ,Δ) phase diagram. The white dashed lines roughly define a subregion with a 2^{nd}-order topological superconducting phase hosting MCSs within the $\mathcal{N} = 1$ chiral phase of Ref. (1). Here the lattice has 70×70 sites. Source: By the author. 27

Figure 5 – LDOS from *ab initio* calculations for the [111] surface in Bi_2Se_3 and Sb_2Te_3, respectively. The red parts indicate available states, i.e. the electronic bands. Near the $\overline{\Gamma}$ point, we see the bulk bands separated by a gap and the linear dispersion of the surface states. Source: Adapted from ZANG *et al.* (41). 30

Figure 6 – **a** quintuple layer structure of Bi_2Se_3 and its top (**b**) and side (**c**) views, respectively, with respect to the z axis. Due to the small interaction (compared to the other interactions in the crystal) between the $Se1$ and $Se1'$ layers, we can arrange the crystal in quintuple layers. Source: Adapted from ZANG *et al.* (41). 31

Figure 7 – (**a**) illustrates how the energy levels near the valence orbitals shift as we turn on: (I) chemical bonding; (II) crystal field splitting and (III) atomic spin-orbit coupling, where we followed a decreasing order in energy scale. The third coupling leads to the inversion of levels with *opposite* parity, for certain SOC strength. (**b**), shows the energies of $P1_z^+$ and $P2_z^-$ as a function of the SOC strength x. For $x > x_c \sim 0.6$, we have a level inversion. Source: Adapted from ZANG *et al.* (41). . . . 32

Figure 8 – Wave function profile in the z direction for the surface state with spin ↑, $\psi_\uparrow(z)$. These wave functions correspond to the surface state in Bi_2Se_3 (yellow) and Bi_2Te_3 (blue). We can see that both of them are localized near z=0. The oscillations on the yellow plot are due to the non-zero imaginary part in its λ solutions. In both cases, $A_1/B_1 > 0$. The parameters used (Eq. 2.6) are taken from *ab initio* calculations and can be found at Table II in (17). Source: By the author. 35

Figure 9 – Sketch of the energy dispersions $E = \pm A_2 k$ and spin texture (arrows) of the surface states. Each of the cones has a well defined helicity/chirality (here they are the same because we have a massless Dirac Hamiltonian). Source: Adapted from LIU *et al.* (42). 36

Figure 10 – Zero-energy solution (blue) for $H_{\text{surf+Zeeman}}$ and the Zeeman field profile (mass domain) $m_z(x)/\hbar v_F = tanh(x)$ (orange). The solution is localized at the domain wall. Source: By the author. 39

Figure 11 – Energy dispersions of a continuum Dirac Hamiltonian (blue) and its lattice version (red). At any given energy, the lattice model shows four states, while the continuum model only has two, this is the so-called fermion doubling problem. Source: By the author. 45

Figure 12 – Energy dispersion for the continuum Dirac model in dotted blue, and for the lattice model with the Wilson mass $W = \hbar v_F a^2/2$ in red. Now the states near $k_i a = \pi$ have been lifted and both models agree for small energy. Source: By the author. 46

Figure 13 – Dispersion relation for different Zeeman fields m_z showing the closing points of the gap at $m_z = \pm\Delta$ (as $\mu = 0$) and the gapped regions in between, which are in different topological phases: a pair of chiral Majoranas ($m_z = -2\Delta$); a single chiral Majorana ($m_z = 0$) and trivial phase ($m_z = 2\Delta$). Here $\Delta = \hbar v_F/2a$ and $W = \hbar v_F a/2$. Source: By the author. 48

Figure 14 – Phase diagram showing the possible topological phases and their topological index (*c.f.* Appendix B). The blue cones show the condition $\mu^2 + \Delta^2 = m_z^2$, where the system is gapless. Source: Adapted from QI *et al.*(1). 49

Figure 15 – Illustration of the four possible reflections symmetries in a square. It can also be seen that reflections of a 2D object can be viewed as a rotation if that object is embedded in the 3D space. Source: By the author. 54

Figure 16 – The three possible processes in an N/S/N junction. All three figures show the occupation levels in the left and right normal regions (N) and the gap Δ in the superconducting region (S). **a.** shows the direct tunneling of an electron through the superconductor. This process is equal to what happens in a usual potential barrier. **b.** is the Andreev reflection, i.e. we create a Cooper pair in the superconductor by using the incident electron and another electron from the left normal region. This other electron will leave a vacancy and create a reflected hole. **c.** is similar to **b.** and shows us the cross Andreev reflection. Now the vacancy creates a hole moving forward in the right normal region. Source: By the author. 65

Figure 17 – Density of state for two different set of parameters. **a.** The DOS exhibits a profile with several peaks within the gap (i.e., $E < \Delta$), which correspond to Majorana chiral edge states. **b.** The DOS shows one expressive peak at $E = 0$ with a DOS 10 time bigger than the DOS of the chiral edge states in **a.** This second set of parameters is in a 2^{nd}-order TSC phase that gives us four Majorana corner states. Source: By the author. 68

Figure 18 – Local density of states (LDOS) at zero energy showing chiral Majorana edge states (left) morphing into four Majorana corner states (right) as we move in the parameter space (μ, Δ). In this case, only the chemical potential μ vary. Source: By the author. 68

Figure 19 – Dependence of the lowest eigenenergies of our planar QAH-SC setup with the square lattice size N ($N \times N$ sites) for **a.** the chiral phase [($\mu = 0.5t$,$\Delta = 0.7t$)] and **b.** the phase hosting MCSs [($\mu = 1.5t$, $\Delta = t/4$)]. In contrast with the chiral regime, in the phase with corner states **b**, corner-mode hybridizations decrease as N increases and all the energies approach zero. This behavior indicates that these four modes become MCS for large lattice sizes. Note the difference in scale of the vertical axes in **a.** and **b.** Source: By the author. 69

Figure 20 – Spin texture of the chiral Majorana edge states (left side) and spin texture of a Majorana corner state (right side). The arrow at a given position $\vec{r}$ represent the vector $(\langle S_x^{\vec{r}}\rangle, \langle S_y^{\vec{r}}\rangle, \langle S_z^{\vec{r}}\rangle)$. Notice that the MCS has an out-of-plane spin component and a "hedgehog" configuration. The parameters are the same as in Fig. 18. Source: By the author. . . . 71

Figure 21 – On site singlet pairing function. The upper panels (**a.** and **b.**) show the complex phase $\varphi(\vec{r})$ and the lower panels (**c.** and **d.**) show the absolute value $|\langle c_{\uparrow,\vec{r}} c_{\downarrow,\vec{r}}\rangle|$. Furthermore, the left panels (**a.** and **c.**) correspond to the TSC ($\mathcal{N} = 1$) phase with chiral Majorana edge states and the right panels (**b.** and **d.**), to the 2^{nd}-order phase with Majorana corner states. The main difference between the TSC ($\mathcal{N} = 1$) and the 2^{nd}-order phase, in terms of the pairing function, is that: in high-order phase, a domain wall structure appears in the phase $\varphi(\vec{r})$ at the corners. Source: By the author. 72

Figure 22 – **a.** transformation from a square lattice into a rectangular lattice to reduce the rotational C_4 symmetry into C_2. **b.** Lowest energy state wave-function for $a_x = a_y/3$. We see that even though the C_4 symmetry is removed, the four corner states still exist; therefore, these states are not protected by this symmetry. Source: By the author. 74

Figure 23 – **a.** schematic to show the Zeeman field direction as a function of the polar angle θ. **b.** six lowest enegy states as a function of the Zeeman field angle. We can see that for odd multiples of 45°, we have two zero-energy states, corresponding to the scenarios where either $\mathcal{M}_{x+y}\mathcal{T}$ or $\mathcal{M}_{x-y}\mathcal{T}$ is preserved. At the remaining angles, both symmetries are broken and all the Majorana corner states are removed. The parameters for the plot are $\mu = 1.4t$ $m_\theta = 0.4t$ $\Delta = t/4$ and the lattice has 90×90 sites. Source: By the author. 75

Figure 24 – **a.** wave-function of the zero energy states for the Zeeman field angle $\theta = 45°$ **b.** wave-function of the zero energy states for the Zeeman field angle $\theta = 135°$. For $\theta = 45°$ the $\mathcal{M}_{x+y}\mathcal{T}$ symmetry is preserved but not $\mathcal{M}_{x-y}\mathcal{T}$, hence only two of the corner states remain gapless. On the other hand (**b.**), for $\theta = 135°$ only $\mathcal{M}_{x-y}\mathcal{T}$ is preserved and the states switch corners. Source: By the author. 76

Figure 25 – Schematic of the system used in the transport calculation: a source (S) lead (1) and three drains (D), the at the zero-bias conductance is calculated between S and D. The possible transport processes are: direct tunneling between the source lead and each of the drains, indicated by solid arrows and local Andreev reflection at the source lead, indicated by the dashed arrow. A symmetric potential drop is used between the source and the drains so that cross Andreev reflection processes cancel out. Source: By the author. 79

Figure 26 – Color map of zero-bias conductance peak as a function of μ and Δ for a finite square lattice. The blue region corresponds to the ordinary TSC ($\mathcal{N} = 1$), which hosts chiral Majorana edge states. The 2^{nd}-order TSC region shows where we find Majorana corner states through its transport signature $\mathcal{G} = e^2/h$. The red part of the 2^{nd}-order phase show where we have hybridized corner modes due to spatial proximity. Source: By the author. 80

Figure 27 – Total transmission (Andreev reflection + direct tunneling) for a two terminal measurement within the chiral Majorana regime. As the system is finite in every direction, we see resonant peaks going to 0.5 rather than a constant plateau. Notice that there is no peak at E=0. Source: By the author. 81

Figure 28 – Chern number calculated for the upper (lower) 2×2 diagonal block of the Hamiltonian. If the mass $m_z \pm \Delta$ is negative we have a non-trivial phase and the Chern number is 1. Source: by the author. 94

CONTENTS

1 INTRODUCTION . . . 21

2 MODEL . . . 29
2.1 3D topological insulators and their surface states . . . 29
2.1.1 **3D TI (minimal) Hamiltonian model** . . . 30
2.1.2 **Surface states** . . . 33
2.1.3 **Quantum anomalous Hall effect** . . . 37
2.2 Topological superconductivity . . . 39
2.2.1 **Majorana edge states** . . . 40
2.3 Lattice model . . . 44
2.3.1 **Fermion doubling and Wilson mass** . . . 44
2.3.2 **Phase diagram** . . . 46
2.3.3 **Real space lattice model** . . . 49

3 METHODS . . . 51
3.1 Symmetry analysis of the lattice model . . . 51
3.2 Non-equilibrium Green's functions . . . 56
3.2.1 **Self-energies** . . . 57
3.2.2 **Density of states** . . . 60
3.2.3 **Spin texture** . . . 62
3.2.4 **Single particle coherent transport** . . . 62

4 RESULTS AND DISCUSSION . . . 67
4.1 New phase: corner states . . . 67
4.2 Symmetry protection . . . 73
4.3 Transport signatures . . . 78

5 CONCLUSION . . . 83

REFERENCES . . . 85

APPENDIX A – EFFECTS OF A SUPERCONDUCTING LEAD ON DIRAC HAMILTONIANS . . . 91

APPENDIX B – TOTAL CHERN NUMBER . . . 93

1 INTRODUCTION

The term “Majorana fermion” was coined after the italian physicist Ettore Majorana, who discovered this particular solution of the Dirac equation. The remarkable feature of his solution is its self-adjointness (2), i.e., the creation and annihilation operators for that solution are equal. In physical terms, this means that the particle and anti-particle represented by that solution are equal.

Although we are still looking for Majorana particles within the Standard Model zoo (3,4), the appearance of the word “Majorana” in the scientific literature has exponentially increased in the last couple of decades, as exemplified in Fig. 1 for APS journals. However, this popularity has nothing to do with high-energy physics. In fact, it was the condensed matter community that brought the term into vogue again.

In the next pages, I would like to introduce the concept of the condensed matter Majorana. To this end, I will answer *why* so many people are interested in this elusive particle and *how* people usually envision bringing it to reality. Moreover, I will present the main results and the structure of this work that aims to extend our knowledge on the *how* question.

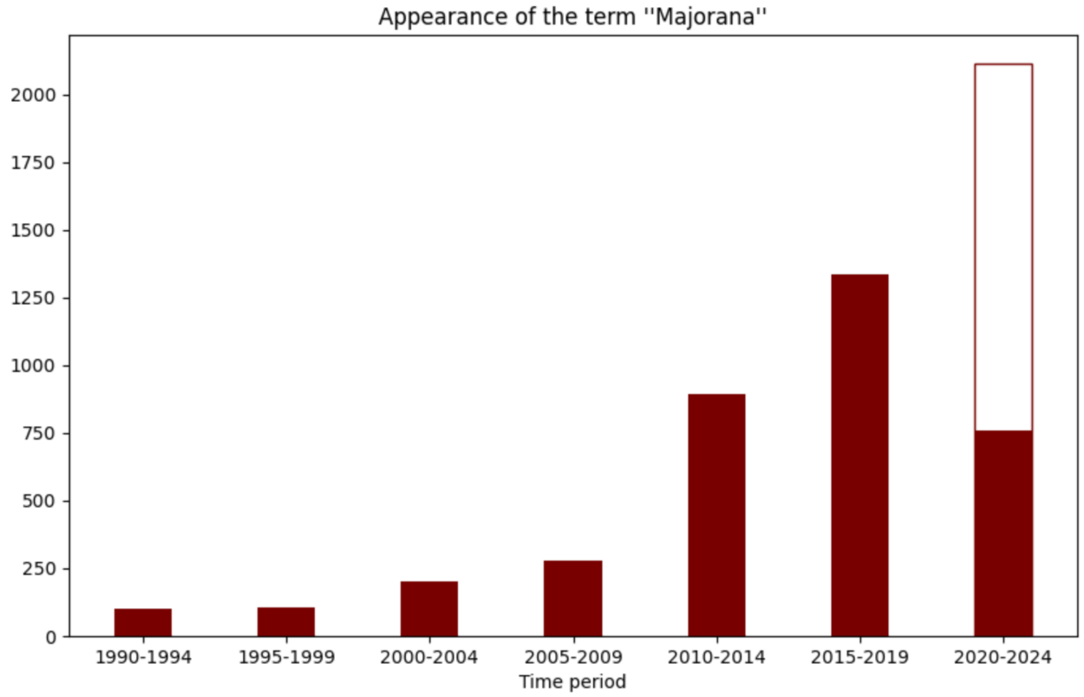

Figure 1 – Number of times that the term “Majorana” was used either in the abstract or title in APS journals over a given period of time. The white part of the 2020-2024 bar is a projection (through an exponential fitting) for the next couple of years. Source: By the author.

Why Majoranas?

The reason that brought Majorana particles into the spotlight in the 21st century, as mentioned, was the possibility of emulating these particles in the condensed matter realm. More specifically: the possibility of having Majorana quasi-particles (excitations) through the collective behavior of electrons. However, the condensed matter Majoranas are not predicted to exist as free propagating fermions as originally proposed by Ettore Majorana, but rather as non-abelian bound states in 1D (or 2D) (5–7).

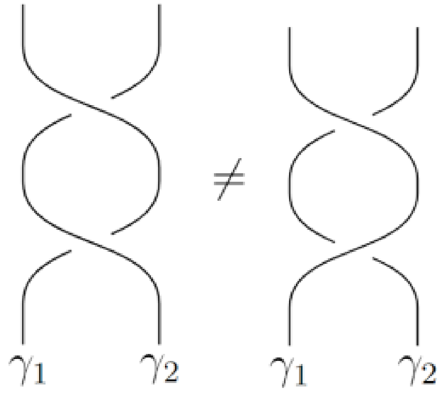

Figure 2 – Diagram of two nonequivalent braid operations between two Majorana states. If we braid the “strings”, the left operation ends up crossed “strings”, while the right operation will have the “strings” separated. Source: By the author.

Note that these Majorana bound states are not ordinary fermions, i.e. they do not follow the fermionic exchange (commutation) rules. Instead, their commutations are explained through a braiding group, *c.f.* Refs. (7-8). This unusual feature made Majoranas strong candidates to create topological qubits and therefore to devise a topological quantum computer (TQC) due to the possibility of performing logical operations by moving (and braiding) non-abelian anyons around each other (9–11).

Here, the term “topological” comes from the fact that the Majorana states are topological excitations, i.e., they live at the boundary between a topologically trivial and a non-trivial region (e.g., edge states) in a given system or bounded to a defect (e.g., a superconducting vortex). This topological nature guarantees robustness to these states, i.e., they should exist as long as the topology of the system does not change (which is equivalent to not closing the bulk gap). Furthermore, as we use spatially separated Majorana modes to create qubits and perform logical gates, local environment noise cannot create decoherence in the qubits (12-13).

“How Majoranas?”

Now that we briefly showed why Majoranas are getting the attention that they are getting, we will present how people often envision bringing them to reality and finally how this dissertation intends to extend our knowledge about this issue.

The main feature of Majorana modes is that its anti-particle is the particle itself, in terms of creation and annihilation operators $\gamma = \gamma^\dagger$, where (in condensed matter models) γ is a combination of electron creation and annihilation operators $c^\dagger$ and c, e.g. $\gamma = (c+c^\dagger)$. On the other hand, it is known (14) that the excitations of an s-wave superconducting phase (Bogoliubons) obey a similar relation $\gamma_{E\uparrow} = \gamma^\dagger_{-E\downarrow}$ for a given spin and energy E. Hence, if we can create a zero-energy* state and get rid of the spin condition, we would have a Majorana excitation.

The idea found to overcome this challenge was through chiral p-wave superconductivity, often associated with the break of time-reversal symmetry (TRS) and a non-trivial bulk topology, i.e., a topological superconducting (TSC) phase (15). Within this class of superconductors, the pairing occurs between electrons with the same spin and therefore the spin problem found in s-wave superconductors is solved. Now we need to make a zero-energy state, the idea is to create a Jackiw-Rebbi (16) like soliton mode, i.e., a state bounded to a domain wall. The first and more common ways to build this mode are: either as an edge state at the ends of a 1D chain (5) or as a state bounded to a topological defect, i.e., a vortex core (6).

The immediate question that arises from this idea is: in which systems do these zero-energy states emerge? The scientific community came up with many setup proposals, all of them with pros and cons. So far it seems that we do not have a definitive and unique path to create Majorana zero-modes. Below we mention some of the most common proposals†.

A straightforward path is to look for materials with intrinsic chiral p-wave pairing and then introduce a vortex core to bind a Majorana. The downside of this method is that intrinsic p-wave superconductivity is not easily found and, in addition, the experimental results for some propsed candidate materials, e.g., $\mathrm{Sr_2RuO_4}$ are still controversial (19–22). Moreover, another disadvantage, which is shared among all proposals that aim at creating Majorana modes through vortex cores, is the presence of other trivial sub-gap fermionic states with finite energy bounded to the vortex (18).

In contrast with materials with intrinsic p-wave pairing, other routes have been proposed by engineering non-trivial[‡] superconducting pairing. One of these routes was proposed by Fu and Kane in their seminal work (23) that studies the heterojunction between a trivial s-wave superconductor (SC) and a topological insulator (TI). This kind of setup provides a 2D platform, hence we can again use vortices to make Majorana states emerge. Moreover, When the TI is in a quantum anomalous Hall (QAH) phase, this setup also hosts Majorana fermion edge states (1), i.e. edge states with Fermi-Dirac statistics and $\gamma_E = \gamma^\dagger_{-E}$. Even though these edge states are ordinary fermions, they also can be used to perform topological quantum computation as proposed in Ref. (24).

---

*Here, zero-energy is not arbitrarily defined, i.e., the state cannot be shifted to another energy. This pin to zero-energy happens because the bound state will always be in the middle of the energy gap and the superconducting gap is around the Fermi energy, which defines the excitation spectra.

†this is not an exhaustive list, for a more complete review see Refs. (17-18).

Another "tricky" way to make topological superconductivity without resorting to intrinsic pairing is to gather the following ingredients: a semiconductor (either a 1D nanowire or a 2DEG) with spin-orbit coupling, a Zeeman field and a proximitized s-wave superconductor. Within this setup, it is possible to choose the Zeeman field, the chemical potential μ and the superconducting pairing to obtain a TSC phase with Majorana modes at the terminations of the wire (or bounded to a vortex in the 2DEG case) (25–28).

More recently, higher-order topological superconductivity (HOTSC) has been proposed as a path to Majorana zero-modes (29–38). As this path is of particular interest for this work, let us take a deeper look at it so we can compare what has been done in the literature with our results in this dissertation.

To produce HOTSC, a recipe, which we will call the "usual path", was designed and has been motivating several proposals. This recipe consists of using a TSC with helical edge states (Kramers pairs) and adding a spatially anisotropic mass gap to the system. Finding the appropriate mass term is the part that requires ingenuity because it must: (*i*) gap out the edge states and (*ii*) make adjacent edges have opposite signs of the "mass". When these conditions are satisfied, domain walls arise at the corners and hence trap zero-energy states, as we illustrate in Fig. 3. Alternatively, one can start with a topological insulator (e.g., a quantum spin Hall system) and add an anisotropic mass through the pairing function. i.e., a d-wave pairing (32,35).

[‡] in the topological sense of the word "trivial".

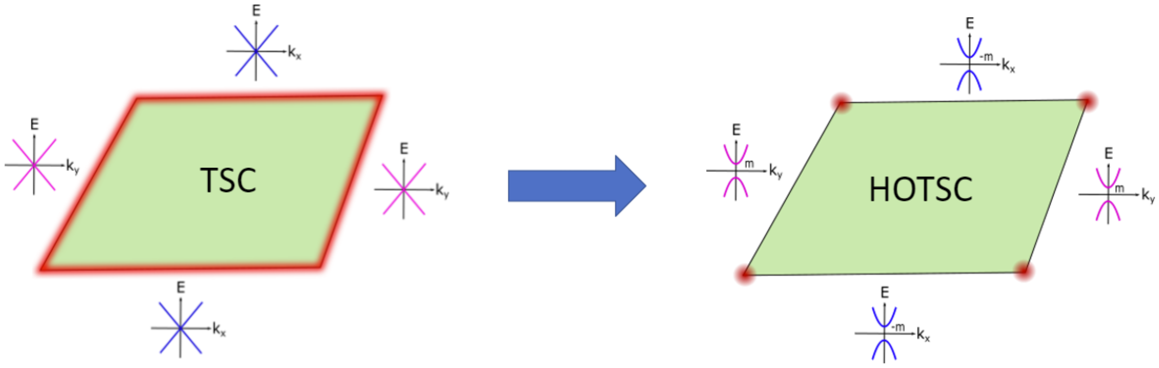

Figure 3 – Schematic of a 2D system showing the usual "prescription" to engineer a HOTSC phase with Majorana corner states. The idea is to gap out edge states with an anisotropic gap, such that the mass gaps have opposite signs along adjacent edges, thus forming domain walls. Source: By the author.

In this work, we will see that it is possible to obtain Majorana corner states (MCS) in a manner that does not require the anisotropic mass gap. These MCS appear in a QAH and s-wave superconductor junction, which is known for hosting chiral Majorana edge states (1). We conjecture that the emergence of this 2^{nd}-order topological phase happens due to the self arranging of the induced superconducting pairing function in the presence of boundaries (edges and corners). It is also important to mention that this work extends the work of *Qi et al.*(1) that presents the ordinary topological phases (i.e., phases with bulk-edge correspondence associated with a Chern number) of this junction. Here, we show that this system can host a 2^{nd}-order phase within the proposed chiral phase, not anticipated by *Qi et al.*(1).

To explore our findings, the remaining of this work is organized as follows: in Chapter 2, we look at the model Hamiltonian that we use and its known properties (e.g., edge states) and ordinary (bulk) phases. To this end, we will begin by introducing a possible candidate to realize the QAH part of the QAH/SC junction: a generic 3D topological insulator and its surface states. Then, we explore the QAH phase and what happens when we couple the QAH layer to an s-wave superconductor. Moreover, we introduce a lattice version of our QAH/SC Hamiltonian that will be useful as we consider finite systems later on.

In Chapter 3, we look at the two approaches that we have used to obtain and discuss our results: a symmetry analysis of our Hamiltonian and the non-equilibrium Green's functions (NEGF) technique. A detailed symmetry analysis is essential to determining the relevant symmetries for the 2^{nd}-order TSC phase. Green's functions allow us to perform consistent quantum transport calculations to obtain conductances and look at properties such as the (local) density of states.

With the model and tools to analyze it, in Chapter 4, we look at a finite square geometry where we see the emergence of four MCS and investigate their properties. The panels in Fig. 4 summarizes our most important findings. We visualize these states through their local density of states (LDOS), obtained using Green's functions, and also through their wave-functions, obtained via direct diagonalization of our Hamiltonian, Fig. 4 a. Furthermore, we conjecture that the Majorana corner states are associated to the formation of phase domain wall in the pairing function, i.e., a sign change in the phase of the superconducting pairing at the corners, Fig. 4 b., which we calculate tentatively calculate through a simplistic procedure (not self-consistently). We further conjecture that these phase domains appear due to the presence of boundaries (edges $4and$ corners).

We also show the corner states are protected by two magnetic reflection symmetries $\mathcal{M}_{x+y}\mathcal{T}$ and $\mathcal{M}_{x-y}\mathcal{T}$, where $\mathcal{M}_{x\pm y}$ is the reflection operation through the diagonals $x \pm y$ of the square system and $\mathcal{T}$ is the time-reversal operation. Last but not least, we discuss "when" (for which parameters) the MCS appear. In order to complete this last task, we perform a transport calculation in a corner geometry (i.e., one normal lead attached to each corner, Fig. 4 c) and a zero-bias conductance peak map (Fig. 4 d.) in the parameter space defined by the chemical potential μ and the pairing Δ, i.e. $\mathcal{G}(E = 0, \mu, \Delta)$, that allows us to separate the known phase with chiral Majorana edge states (from Qi *et al.* (1)) from the new phase with Majorana corner modes. The TSC phase with chiral Majorana edge states is characterized by the total Chern number (i.e., the sum of Chern numbers calculated in the particle and hole subspace) $\mathcal{N} = 1$ and a conductance $e^2/2h$ as shown by Chung *et al.* (39). In the absence of a topological invariant[§] we can only characterize the MCS through a zero-bias conductance peak of e^2/h and the shape of their wave-function and zero eigenenergies.

[§] which would represent either a bulk-corner or bulk-edge-corner correspondence

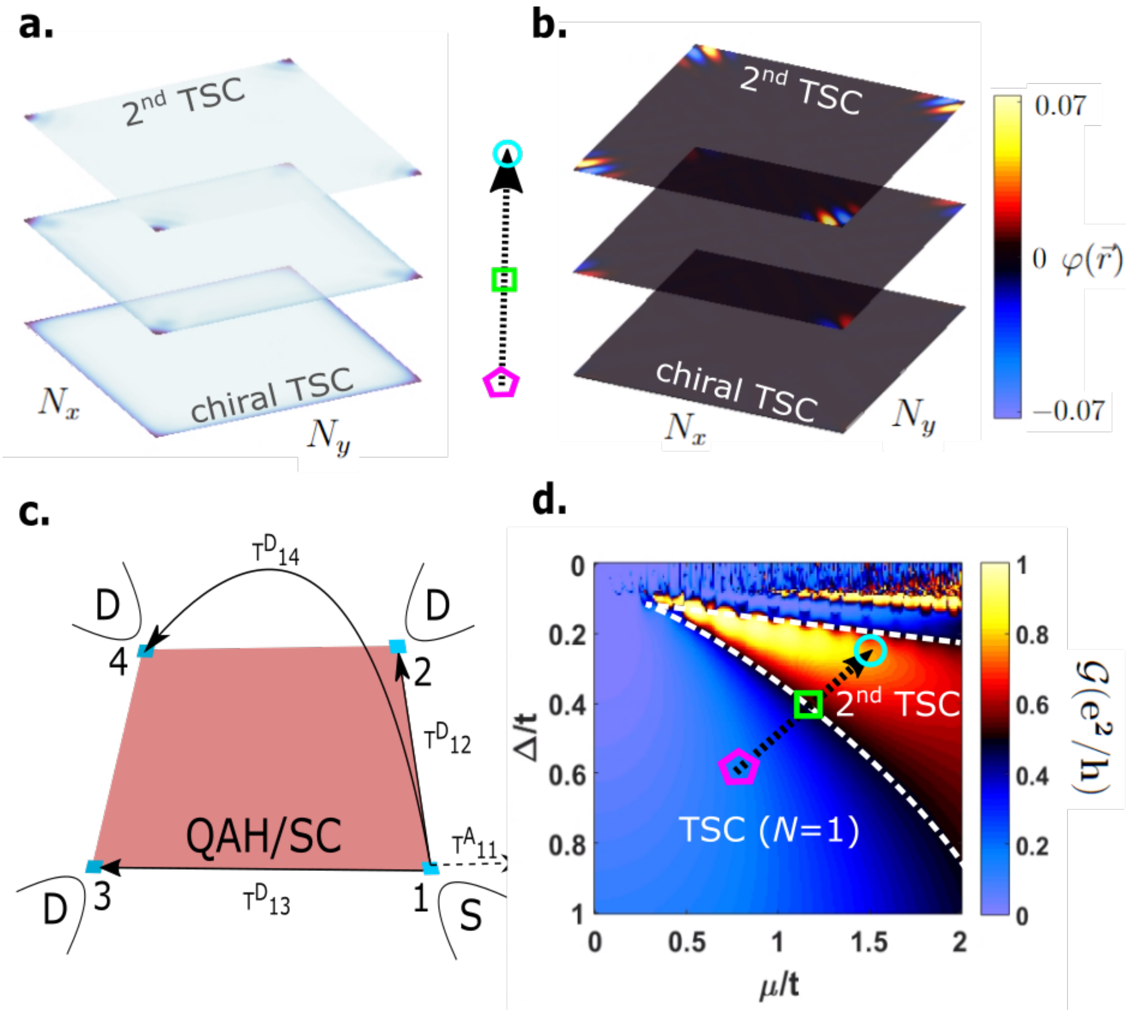

Figure 4 – Panels **a.** and **b.** show, respectively, the spatial probability density $|\psi_{BdG}(\vec{r})|^2$ of the lowest energy eigenstates and the real phase $\varphi(r)$ of our calculated pairing gap $|\langle c_{\uparrow,\vec{r}}\, c_{\downarrow,\vec{r}}\rangle|e^{i\varphi(r)}$ for distinct points in the phase-diagram **d.**. As one moves along the black dashed arrow (see symbols), the four lowest energy chiral Majorana modes (lowest plane in a.) evolve into four fully localized MCSs at zero energy. The probability densities of the MCSs strongly correlate with the emergence of the phase domains, cf. topmost planes in **a.** and **b.**. **c.** Schematic of our square-shaped QAH-SC setup with one corner source (S) and three corner drains (D). The arrows indicate the allowed transport processes, i.e., direct tunneling and (local) Andreev reflection. **d.** Zero-bias conductance $\mathcal{G}$ map as an effective (μ,Δ) phase diagram. The white dashed lines roughly define a subregion with a 2^{nd}-order topological superconducting phase hosting MCSs within the $\mathcal{N} = 1$ chiral phase of Ref. (1). Here the lattice has 70×70 sites. Source: By the author.

2 MODEL

This chapter presents the building blocks necessary for a QAH-SC junction and, eventually, an effective model for it. We start by looking at a candidate for the QAH layer of the junction: a 3D topological insulator and its surface states. We will look at their effective low-energy (continuum) Hamiltonian and at properties such as the spin texture of the surface states. By introducing a Zeeman field, we show how to obtain the QAH phase. Next, we introduce proximity s-wave superconductivity to the effective Hamiltonian of the surface states. With these two ingredients, we can obtain and study the topological superconductor phases found by Qi *et al.* (1). Finally, we introduce a lattice version of our effective Hamiltonian model. The lattice Hamiltonian is used to obtain a bulk phase diagram. Moreover, we transform the lattice Hamiltonian into the real space representation, which enables us to consider a finite square geometry where Majorana corner states, not anticipated by Qi *et al.* (1), can emerge.

2.1 3D topological insulators and their surface states

The discovery of a topological phase in HgTe quantum wells (40), that relies on the simple idea of inverting bulk bands with different symmetries (parity in the HgTe case); opened the route to many proposals based on the same principle. One of these proposals is the 3D topological insulator, which can undergo a band inversion and exhibit surface states. In this case, the band inversion is controlled by the strength of spin-orbit terms. Moreover, there are already materials that are verified* to be 3D TI, some of these materials are Bi_2Se_3, Bi_2Te_3 and Sb_2Te_3.

The main feature of these systems is the existence of a *protected* single Dirac cone on a singular surface when the parameters are tuned to the topological phase (inverted bands). It is worth commenting that "protected" in the previous sentence carries two meanings. The first one: protection of the surface state existence, guaranteed by the (inverted) bulk gap, ~ 0.3 eV for Bi_2Se_3 (41), i.e. while the gap is not closed, the surface state will remain there. The second meaning comes from time reversal symmetry and prevents backscattering, due to the Kramers degeneracy, unless we break TRS with a magnetic field or impurity. Note that, as the surface states are 2D, small angle scattering can still occur. Hence this second protection is not as strong as for 1D edge states such as observed in HgTe quantum wells (40).

---

*See (17) and references within.

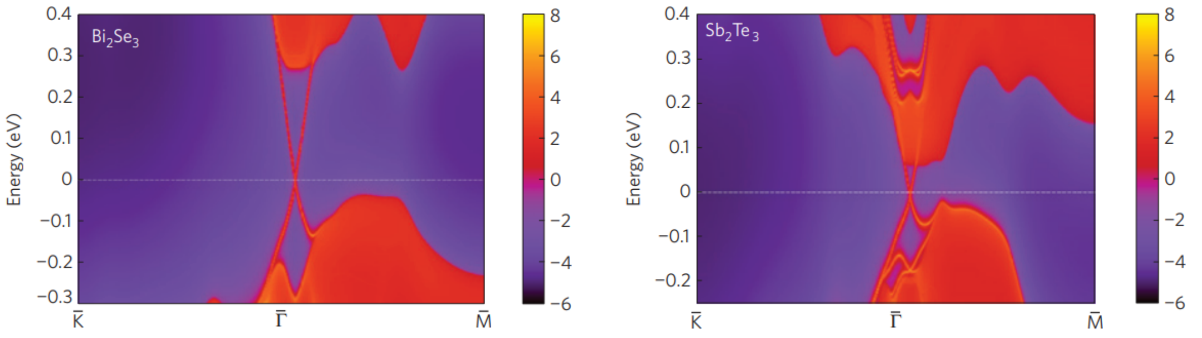

Figure 5 – LDOS from *ab initio* calculations for the [111] surface in Bi_2Se_3 and Sb_2Te_3, respectively. The red parts indicate available states, i.e. the electronic bands. Near the $\overline{\Gamma}$ point, we see the bulk bands separated by a gap and the linear dispersion of the surface states. Source: Adapted from ZANG *et al.* (41).

2.1.1 3D TI (minimal) Hamiltonian model

Now we introduce the low-energy model that effectively describes the phenomenon of band inversion and the emergence of a surface state. To this end, we need[†] to look at the four lowest energy electronic bands near the Γ point (k=0) of a 3D topological insulator. First let us glance over the idea behind the model, without going through the extensive calculations behind it (which can be found in (42)). Then, we will write down the Hamiltonian and discuss its relevant symmetries.

Microscopic background

The materials that were predicted to be 3D topological insulators in (41) share the same crystalline property of being organized in quintuple layers, with five atoms per unit cell, Fig. 6 a. Although we have only two types of atoms (e.g. Bi and Se), they play five different roles in the formation of the energy levels because the interaction between atoms depends on their position in the crystal. In the family of 3d TIs that we are considering here, there are two pairs of atoms that are equivalent under inversion through an inversion center and one atom that is at that inversion center and therefore has no counterpart. For example, as we illustrate in Fig. 6 c, Bi_2Se_3 has two equivalent Bismuth atoms under the inversion through the inversion center, which we identify as $Bi1$ and $Bi1'$. Two of the Selenium atoms are equivalent as well ($Se1$ and $Se1'$) and there is a third one ($Se2$) at the inversion center distinct from the other two.

[†] it is the minimum amount of bands that allow us to see the topological phase that preserves TRS

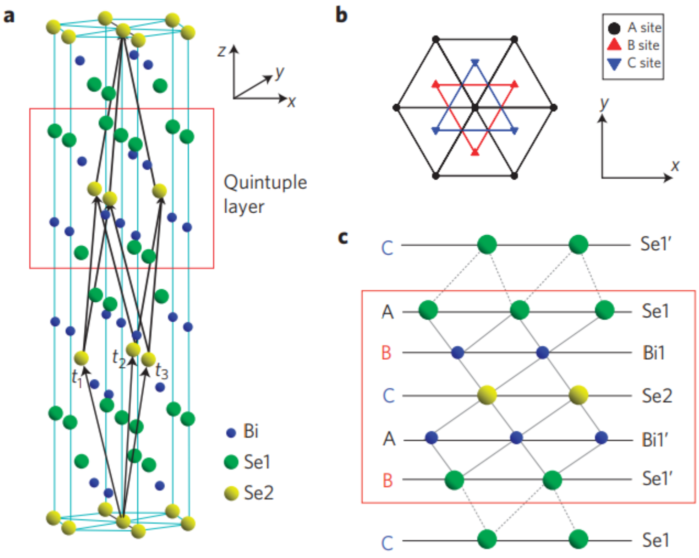

Figure 6 – **a** quintuple layer structure of Bi_2Se_3 and its top (**b**) and side (**c**) views, respectively, with respect to the z axis. Due to the small interaction (compared to the other interactions in the crystal) between the $Se1$ and $Se1'$ layers, we can arrange the crystal in quintuple layers. Source: Adapted from ZANG *et al.* (41).

The energy scale of the couplings linking two quintuple layers is Van-der-Walls like and small[‡] compared to the bonding energy between atom layers within the same quintuple layer (42). As the link between layers will introduce irrelevant energy shifts, we can focus on one quintuple layer and how the coupling in there will shift the orbitals energy. Furthermore, as an approximation, we only look at how the orbitals near the valence levels of Bi and Se, which are p orbitals[§], interact with each other and shift their energies. It is worth pointing out that this latter approximation is valid because the Fermi surface is near those orbitals, however there is no easy proof of this fact. To properly find the Fermi energy, one would need to do a complete band calculation (*ab initio*) as in Ref. (42).

We “turn on” the interactions one by one, beginning with the ones involving larger energy scales. We start with the chemical bonding between Bi and Se atoms, leading us to step (I) in Fig. 7, splitting the levels in such a way that the two that remain close to the Fermi level (dashed blue line in Fig. 7 **a**) are p orbitals from $Bi1$ ($Bi1'$) and $Se1$ ($Se1'$), with opposite parities. Notice that we can separate the states by their parity as there is inversion symmetry, i.e. the inversion symmetry eigenvalues that define whether a given state is an even (+) or odd (-) function are good quantum numbers. In Fig. 7**a.** we represent the p orbitals from $Bi1$ ($Bi1'$) and $Se1$ ($Se1'$) as $P1^{\pm}_{x,y,z}$ and $P2^{\pm}_{x,y,z}$ respectively. For notation clarity, we do not write the spin index.

[‡] Through density functional theory, Ref. (43) suggests a binding energy between $0.025 - 0.25$ eV but not the energy shift in the orbitals.

[§] e.g., the valence levels of Bi is $6s^2p^3$ and Se, $4s^24p^2$.

Then, we consider how the crystal symmetries affect the atomic levels, i.e. the crystal field splitting (44) (step (II) in Fig. 7). This energy splitting ($1.5 \sim 1$ eV (45)) can be seen as the breaking of the angular momentum degeneracy of an orbital level (of an isolated atom) due to the presence of a potential generated by the other atoms. As we see in Fig. 6, there is an asymmetry between z and the in-plane direction (x and y) that splits the $P^{\pm}_{z}$ orbitals towards the Fermi energy and $P^{\pm}_{x,y}$ away from it. This splitting process leaves only $P1^{+}_{z}$ and $P2^{-}_{z}$ (which have double degeneracy due to spin) near the Fermi level.

Using first-order perturbation theory, one can show (42) that the spin-orbit term $\propto \mathbf{s} \cdot \mathbf{L}$, coupling the spin $\mathbf{s}$ and orbital angular momentum $\mathbf{L}$, splits the orbitals $p_{x \pm iy}$ and p_z because of their different angular momentum. For the materials that are 3D TI, this splitting is strong enough ($0.5 \sim 0.9$ eV (45)) to invert the p_z levels (with opposite parities) from Bi and Se, as seen in **b** in Fig. 7, leading to what we call a topological phase. In practical terms "topological phase" is a synonym for inverted bands, but there is a deeper and formal meaning related to topology that associates the band inversion with the change of some topological invariant[¶] in the space defined by the Brillouin zone, we will not explore this aspect here but the interested reader should check references (17,46).

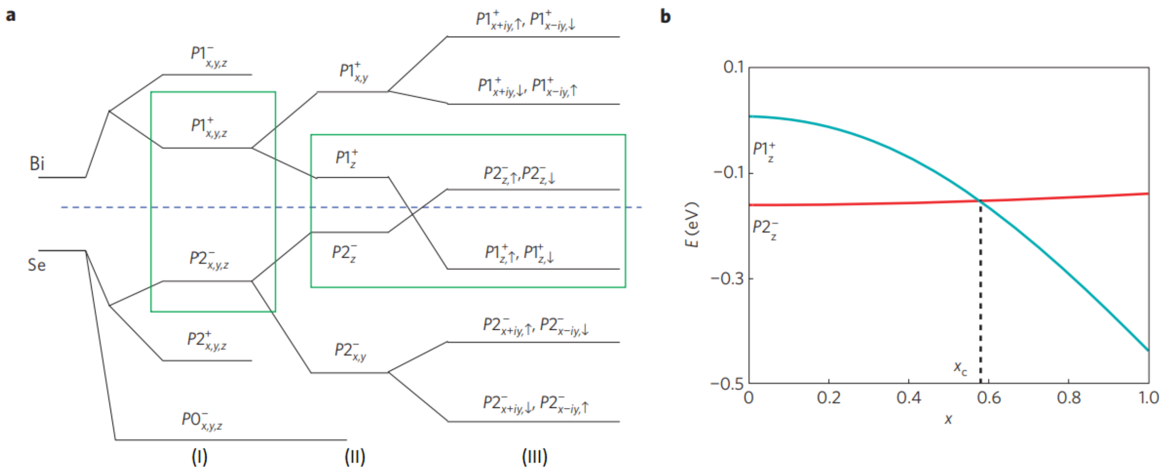
a
Bi
Se
$P1^{-}_{x,y,z}$
$P1^{+}_{x,y,z}$
$P2^{-}_{x,y,z}$
$P2^{+}_{x,y,z}$
$P0^{-}_{x,y,z}$
$P1^{+}_{x,y}$
$P1^{+}_{z}$
$P2^{-}_{z}$
$P2^{-}_{x,y}$
$P1^{+}_{x+iy,\uparrow}, P1^{+}_{x-iy,\downarrow}$
$P1^{+}_{x+iy,\downarrow}, P1^{+}_{x-iy,\uparrow}$
$P2^{-}_{z,\uparrow}, P2^{-}_{z,\downarrow}$
$P1^{+}_{z,\uparrow}, P1^{+}_{z,\downarrow}$
$P2^{-}_{x+iy,\uparrow}, P2^{-}_{x-iy,\downarrow}$
$P2^{-}_{x+iy,\downarrow}, P2^{-}_{x-iy,\uparrow}$
(I)
(II)
(III)
b
E (eV)
0.1
−0.1
−0.3
−0.5
$P1^{+}_{z}$
$P2^{-}_{z}$
x_c
0
0.2
0.4
0.6
0.8
1.0
x

Figure 7 – (**a**) illustrates how the energy levels near the valence orbitals shift as we turn on: (I) chemical bonding; (II) crystal field splitting and (III) atomic spin-orbit coupling, where we followed a decreasing order in energy scale. The third coupling leads to the inversion of levels with *opposite* parity, for certain SOC strength. (**b**), shows the energies of $P1^{+}_{z}$ and $P2^{-}_{z}$ as a function of the SOC strength x. For $x > x_c \sim 0.6$, we have a level inversion. Source: Adapted from ZANG *et al.* (41).

[¶] i.e., some property or quantity that is invariant under continuum transformations

Hamiltonian model

The minimal Hamiltonian where the topological phase emerges can be described through the electronic bands generated from the four atomic levels (p_z orbitals with ↑ and ↓ spin from *Bi* and *Se*) closest to the Fermi energy. This Hamiltonian model can be derived from either symmetry principles or **k.p** theory. However, these derivations are laborious and deviate from the idea of this chapter, which is to introduce and bring insight into the model to be used in this work. The more avid reader can enjoy those calculations over some coffee (probably more than some, to be realistic) reading Ref. (42).

In the basis of the atomic orbitals (see step (III) in Fig 7 **a**) $\{|P1_z^+\uparrow\rangle, |P2_z^-\uparrow\rangle, |P1_z^+\downarrow\rangle, |P2_z^-\downarrow\rangle\}$, where ↑ (↓) stands for the spin, and $P1_z$ and $P2_z$ for the p_z orbitals from *Bi* and *Se*, respectively, the low-energy (up to $\mathcal{O}(k^2)$) Hamiltonian is

$$\mathcal{H}_{3D} = \epsilon_0(\mathbf{k})\mathbf{I} + \begin{pmatrix} \mathcal{M}(\mathbf{k}) & A_1 k_z & 0 & A_2 k_- \\ A_1 k_z & -\mathcal{M}(\mathbf{k}) & A_2 k_- & 0 \\ 0 & A_2 k_+ & \mathcal{M}(\mathbf{k}) & -A_1 k_z \\ A_2 k_+ & 0 & -A_1 k_z & -\mathcal{M}(\mathbf{k}) \end{pmatrix}, \tag{2.1}$$

where $\epsilon_0(\mathbf{k}) = C + D_1 k_z^2 + D_2 k_\perp$, $k_\pm = k_x \pm i k_y$ and $\mathcal{M}(\mathbf{k}) = M - B_1 k_z^2 - B_2 k_\perp^2$. Here $\{A_{1,2}, B_{1,2}, C, D, M\}$ are material parameters (to be determined experimentally or through *ab initio* calculations) and $k_\perp \equiv \sqrt{k_x^2 + k_y^2}$.

Looking at the minimal Hamiltonian $\mathcal{H}_{3D}$ we see that it has inversion and time-reversal symmetries, with the corresponding operators defined by $\mathcal{I} = \mathbf{I} \otimes \tau_z$ and $\mathcal{T} = i\,\sigma_y \mathcal{K} \otimes \mathbf{I}$, respectively. Here $\mathcal{K}$ is the complex conjugation operator; $\sigma_i(\tau_i)$, $i \in \{x, y, z\}$, are the Pauli matrices acting on spin (orbital) degrees of freedom and $\mathbf{I}$ is the 2×2 identity. If $D_{1,2} = 0$, we also have a generalized particle-hole symmetry[‖] around energy E=C. Although this "accidental" symmetry seems not relevant, it allows us to perform a trick in the calculations ahead.

2.1.2 Surface states

Having the 3D bulk Hamiltonian defined in Eq. 2.1, we now create one planar interface with vacuum, i.e. a surface, solve $\mathcal{H}_{3D}\Psi = E\Psi$ and look for solutions localized at the "interface", i.e., surface state solutions. As we see below, the system parameters must obey a particular relation in order to surface states to occur.

More realistic calculations, taking into account a second surface (thin slab geometry), can be performed, *c.f.* (48). However, such calculations do not add much to

---

[‖] the generalized relation for the particle-hole operator takes into account energy shifts, so the electron and hole band can be symmetric around energies other than 0. In mathematical terms $\mathcal{P}$ is: $-\mathcal{P}^\dagger(\mathcal{H} - \frac{1}{4}Tr\mathcal{H})^*\mathcal{P} = \mathcal{H} - \frac{1}{4}\mathcal{H}$, where we generalized the definition from (47) to a 4×4 Hamiltonian.

understanding the appearance of the surface states. In what follows, we consider a single surface/interface. This can also be viewed as an approximation to describe the top surface of a “thick” slab or a semi-infinite system.

Let us consider an interface at z=0 while keeping the system infinite in the xy plane. In this scenario, k_x and k_y are still good quantum numbers but k_z is not. Hence we do the change $k_z \to -i\partial_z$.

For simplicity, we take $k_{x,y} = 0$ (later on, we can simply multiply the eigenvector by a free wave $e^{ik_x x + ik_y y}$). In addition, we make an *ansatz* for the solution in the form $e^{\lambda z}\psi$, where λ is to be found and ψ is a position-independent 4×1 spinor. Note that we can “choose” this form for the solutions because the variables are separable. The equation for the eigensolutions, with these considerations, reads

$$(C - D_1\partial_z^2) + \begin{pmatrix} M + B_1\partial_z^2 & -iA_1\partial_z & 0 & 0 \\ -iA_1\partial_z & -M - B_1\partial_z^2 & 0 & 0 \\ 0 & & M + B_1\partial_z^2 & iA_1\partial_z \\ 0 & 0 & iA_1\partial_z & -M - B_1\partial_z^2 \end{pmatrix} e^{\lambda z}\psi = E\, e^{\lambda z}\psi. \quad (2.2)$$

The 2×2 block-diagonal form of the Hamiltonian makes TRS explicit, i.e. they are related to each other through the time-reversal transformations $\tilde{\mathcal{T}} = i\sigma_y\mathcal{K}$. Therefore, we can look for the spin up (down) solutions $\psi_\uparrow$ ($\psi_\downarrow$) and obtain the other “automatically”, $\psi_\sigma = \mathcal{T}\psi_{\sigma'}$.

The upper block equation, which will give us solutions for spin $\uparrow$, is

$$(C - D_1\partial_z^2) + \begin{pmatrix} M + B_1\partial_z^2 & -iA_1\partial_z \\ -iA_1\partial_z & -M - B_1\partial_z^2 \end{pmatrix} e^{\lambda z}\psi_\uparrow e^{\lambda z}\psi = E\, e^{\lambda z}\psi_\uparrow. \quad (2.3)$$

Now we make one further simplification, i.e., we take $D_1 = 0$ to obtain the particle-hole symmetry. In this case, we look for a surface at energy E=C, i.e., in the middle of the gap,

$$\Big[(M + B_1\lambda^2)\tau_z - iA_1\lambda\tau_x\Big]\,\psi_\uparrow = 0. \quad (2.4)$$

Multiplying Eq. 2.4 by τ_x, we rewrite the eigenvalue equation as:

$$(M + B_1\lambda^2)\tau_y\psi_\uparrow = A_1\lambda\psi_\uparrow. \quad (2.5)$$

With this procedure (“trick”), we find immediately the two eigenstates of Eq. 2.5 to be the eigenstates of τ_y, $\psi_{\uparrow+}$ and $\psi_{\uparrow-}$ with 1 and -1 eigenvalues, respectively. Moreover, we find λ to be[**]

$$\begin{aligned} \psi_{\uparrow +} &: \lambda = \lambda_{1,2} = \frac{A_1 \pm \sqrt{A_1^2 - 4B_1 M}}{2B_1}; \\ \psi_{\uparrow -} &: \lambda = -\lambda_{1,2} \end{aligned}. \tag{2.6}$$

Thus the general solution (with spin $\uparrow$) is $\psi_\uparrow(z) = (ae^{-\lambda_1 z} + be^{-\lambda_2 z})\psi_{\uparrow -} + (ce^{\lambda_1 z} + de^{\lambda_2 z})\psi_{\uparrow +}$, where a,b,c,d are complex constants determined by the boundary conditions. Here, these conditions are the continuity of the wave-function at the interface $\psi_\uparrow(z=0) = 0$ and its normalizability $\psi_\uparrow(z \to \infty) = 0$. These constraints require that $M/B_1 > 0$ and imply that

- $\mathrm{Re}\{\lambda_{1,2}\} < 0$ for $A_1/B_1 < 0$ with a=-b and c=d=0;
- $\mathrm{Re}\{\lambda_{1,2}\} > 0$ for $A_1/B_1 > 0$ with a=b=0 and c=-d.

To obtain the solutions of the lower 2×2 block with spin $\downarrow$, we just apply the time-reversal operation to the solutions with spin $\uparrow$.

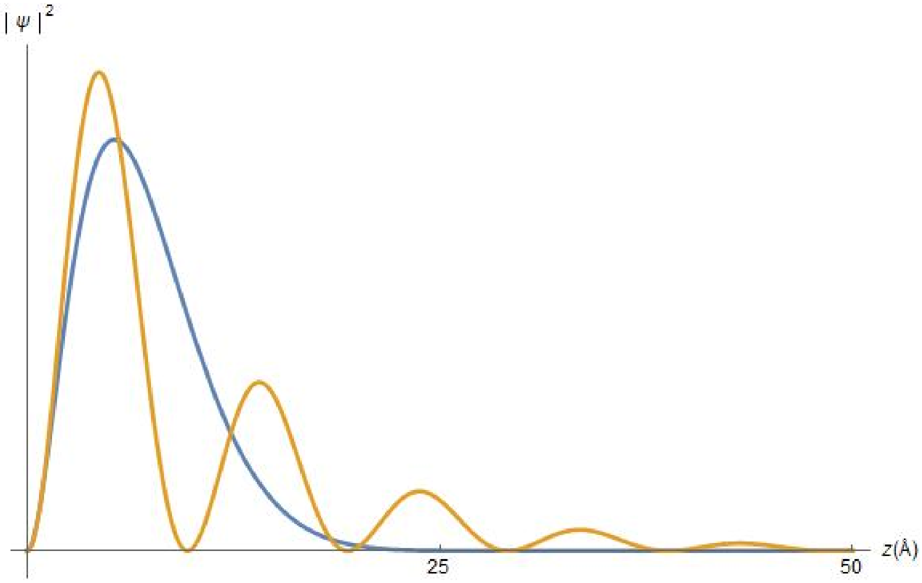

Figure 8 – Wave function profile in the z direction for the surface state with spin $\uparrow$, $\psi_\uparrow(z)$. These wave functions correspond to the surface state in Bi_2Se_3 (yellow) and Bi_2Te_3 (blue). We can see that both of them are localized near z=0. The oscillations on the yellow plot are due to the non-zero imaginary part in its λ solutions. In both cases, $A_1/B_1 > 0$. The parameters used (Eq. 2.6) are taken from *ab initio* calculations and can be found at Table II in (17). Source: By the author.

[**] Note that these solutions for λ are calculated for $k_{x,y} = 0$, otherwise, we would have $\lambda(k_x, k_y)$, *c.f.*, Appendix A on Ref. (49). However, as we will not need the explicit form of $\lambda(k_x, k_y)$, we will not calculate it.

Once we have both the spin up and down solutions $\psi_\uparrow$ ($\psi_\downarrow$), we can project our Hamiltonian $\mathcal{H}_{3D}$ into the subspace spanned by these vectors and create an effective 2D Hamiltonian that describes these surface states

$$H_{\text{surf}} = \begin{pmatrix} \langle\psi_\uparrow|\,\mathcal{H}_{3D}\,|\psi_\uparrow\rangle & \langle\psi_\uparrow|\,\mathcal{H}_{3D}\,|\psi_\downarrow\rangle \\ \langle\psi_\downarrow|\,\mathcal{H}_{3D}\,|\psi_\uparrow\rangle & \langle\psi_\downarrow|\,\mathcal{H}_{3D}\,|\psi_\downarrow\rangle \end{pmatrix} \Rightarrow H_{\text{surf}} = C + A_2(k_y\sigma_x - k_x\sigma_y). \tag{2.7}$$

The effective Hamiltonian H_{surf} is a massless Dirac Hamiltonian and its solutions are readily found to be $E = \pm A_2\sqrt{k_x^2 + k_y^2} = \pm A_2 k$, which define Dirac cones with positive and negative energy. The eigenvectors for these eigenenergies are $\xi(k_x, k_y) = \frac{1}{\sqrt{2}}\begin{pmatrix}\pm e^{-i\phi_k} & -i\end{pmatrix}^T$, where we define $\phi_k = tg^{-1}(k_y/k_x)$. Note that the absolute value of the velocity in these states is constant. Therefore, every state has the Fermi velocity $v_F = A_2/\hbar$. Furthermore, the eigenstates have a well defined spin texture in the k-space, as we can see by calculating the expectation values

$$\langle\sigma_x\rangle = \pm\sin\phi_k; \tag{2.8}$$

$$\langle\sigma_y\rangle = \mp\cos\phi_k; \tag{2.9}$$

$$\langle\sigma_z\rangle = 0. \tag{2.10}$$

Here the upper sign (either + or -) corresponds to the positive energy states and the lower sign, to the negative energy states. The spin texture can be plotted together with the dispersion relation, as we show in Fig. 9.

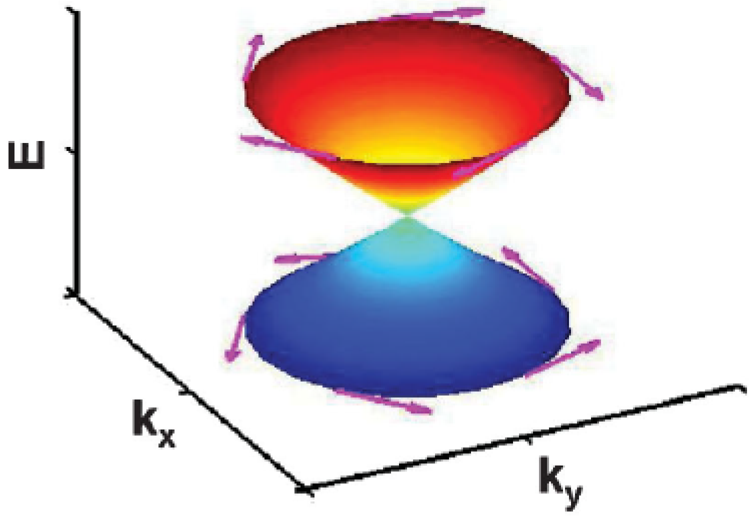

Figure 9 – Sketch of the energy dispersions $E = \pm A_2 k$ and spin texture (arrows) of the surface states. Each of the cones has a well defined helicity/chirality (here they are the same because we have a massless Dirac Hamiltonian). Source: Adapted from LIU *et al.* (42).

2.1.3 Quantum anomalous Hall effect

An important addition to our model is the possibility of breaking time-reversal symmetry and simultaneously adding a mass gap to the spectrum with a Zeeman field $\vec{m}\cdot\vec{\sigma}$, where $\vec{m}=(m_x,m_y,m_z)$ is a given constant vector. This addition will introduce the possibility of having the Quantum anomalous Hall (QAH) phase, which is one of the building blocks of our QAH-SC junction.

The quantum anomalous Hall phase is a topological phase with time-reversal symmetry broken but without a quantizing magnetic field (i.e., no Landau levels). This phase is characterized by a gaped bulk spectrum and the presence of gapless edge states with defined chirality[††] either at interfaces with a trivial material (or vacuum) or at a domain wall, i.e., a line where the mass gap changes sign.

Our Hamiltonian model $H_{\rm surf}(k)$ is a Dirac-like models with spin 1/2 and time-reversal symmetriy ($\tilde{\mathcal{T}}=i\sigma_y\mathcal{K}$), i.e., it satisfies $\tilde{\mathcal{T}}H_{\rm surf}(k)\tilde{\mathcal{T}}^{-1}=H_{\rm surf}(-k)$ (see (46)). Now, to show that a Zeeman field breaks TRS we will make a small digression.

More generally, any 2×2 Hamiltonian (with spin 1/2) can be written as $\vec{A}(k)\cdot\vec{\sigma}$, where $\vec{A}(k)$ is a generic vector and a function of k. As the TR condition implies that $\tilde{\mathcal{T}}\vec{A}(k)\cdot\vec{\sigma}\tilde{\mathcal{T}}^{-1}=\vec{A}(-k)\cdot\vec{\sigma}$, it is possible to show that this is equivalent to $\vec{A}(k)=-\vec{A}(-k)$, i.e. $A(k)$ being odd in k. Therefore, any even (in k) or k-independent terms added to the $\vec{A}(k)$ vector would break TRS. As an arbitrary Zeeman field $\vec{m}\cdot\vec{\sigma}$ is k-independent, it breaks TRS. However, note that not any term that breaks TRS will open a gap in the energy spectra, which is a requirement to obtain the QAH phase. For instance, if we consider the Zeeman field along the x direction (i.e., in-plane magnetization) $m_x\sigma_x$ in $H_{\rm surf}(k)$, we would have $C+A_2[(k_y+m_x)\sigma_x-k_x\sigma_y]$, which has the same spectrum but with the Dirac point shifted from $(k_x=0,k_y=0)$ to $(k_x=0,k_y=-m_x)$.

On the other hand, if the Zeeman term corresponds to an out-of-plane magnetization $m_z\sigma_z$ the effect on the spectrum is different; the bands of $H_{\rm surf}$ will be gaped and the dispersion becomes $E(k)=C\pm\sqrt{(\hbar v_F)^2\ k^2+m_z^2}$. Furthermore, by adding this term to our surface model $H_{\rm surf}$, we can identify it with the Chern insulator (46), which is known for having a QAH phase for $m_z<0$. Hence, we (indirectly) showed that adding an out-of-plane (z) Zeeman field introduces the possibility of having a QAH phase.

QAH edge state

Now, we will explicitly show the existence of the QAH edge states by performing a similar[‡‡] calculation to that of Sec. 2.1.2, i.e., we consider an interface between a (topological) region with inverted mass gap ($m_z<0$) and a trivial region, and look for in-gap states. However, here, instead of considering an interface with vacuum, we will consider a domain wall in an infinite system. We take m_z as a function of the spatial coordinate x, such that $x > 0$ corresponds to the trivial region and has $m_z(x) > 0$. For $x < 0$, we consider $m_z(x) < 0$, which corresponds to the topological region in the QAH phase. A possible profile for the Zeeman field that would describe our proposed mass domain would be $m_z \sim \tanh(x)$.

[††] i.e., the edge states momentum has direction and sign defined.

[‡‡] here, instead of starting with a 3D Hamiltonian to find 2D gapless states, we start from a 2D Hamiltonian to find 1D gapless states.

We use the substitution $k_x \to -i\partial_x$ (as we did to find the surface states) in the surface model with the Zeeman term

$$H_{\text{surf+Zeeman}}(x, k_y) = \hbar v_F(k_y\sigma_x + i\partial_x\sigma_y) + m_z(x)\,\sigma_z, \tag{2.11}$$

where we took the constant energy shift C=0 for simplicity. Note that, again, x and y are separable. Hence we can look for solutions at $k_y = 0$ that only depend on x, i.e., $\phi(x) = f(x)(a\ b)^T$, with a and b constants. At E=0,

$$(\hbar v_F i\,\partial_x\sigma_y + m_z(x)\,\sigma_z)\phi(x) = 0, \tag{2.12}$$

if we multiply this equation by σ_z (from the left), we obtain

$$(\hbar v_F\,\partial_x\sigma_x + m_z(x))\phi(x) = 0, \tag{2.13}$$

or, alternatively,

$$\begin{cases} \partial_x f(x)b + \frac{m_z(x)}{\hbar v_F} f(x)a = 0, \\ \partial_x f(x)a + \frac{m_z(x)}{\hbar v_F} f(x)b = 0, \end{cases} \tag{2.14}$$

which yields two solutions $\phi_\pm(x)$[§§] with $a = \pm b$, i.e., the two eigenstates of σ_x,

$$\phi_+(x) = e^{-\int\limits_0^x \frac{m_z(\xi)}{\hbar v_F}d\xi}\begin{pmatrix}1\\1\end{pmatrix} \tag{2.15}$$

$$\phi_-(x) = e^{+\int\limits_0^x \frac{m_z(\xi)}{\hbar v_F}d\xi}\begin{pmatrix}1\\-1\end{pmatrix}, \tag{2.16}$$

up to a normalization factor. As we considered an infinite system, only one of these solutions can be physical, i.e. has finite norm. Which one of the solutions is the “correct” depends on $m_z(x)$ and the sign of $\hbar v_F$.

[§§] the generalization to $k_y \neq 0$ is immediate; we just need to consider the full solution $\phi(x, y)_\pm = e^{\pm i k_y y}\phi(x)_\pm$

For illustrative purposes, let us look at $m_z(x)/\hbar v_F = tanh(x)$. We find the (physical) solution

$$\phi_+(x) = e^{-ln(cosh\ x)} \begin{pmatrix} 1 \\ 1 \end{pmatrix}, \tag{2.17}$$

centered at $x = 0$. By making $k_y \neq 0$, we see that an y dependence is added to our solution in the form of $e^{ik_y y}$, i.e., the edge state propagates along the domain wall as a free wave. On the other hand, the ϕ_- solution is proportional to $e^{ln(cosh\ x)}$ and diverges for $x \to \pm\infty$.

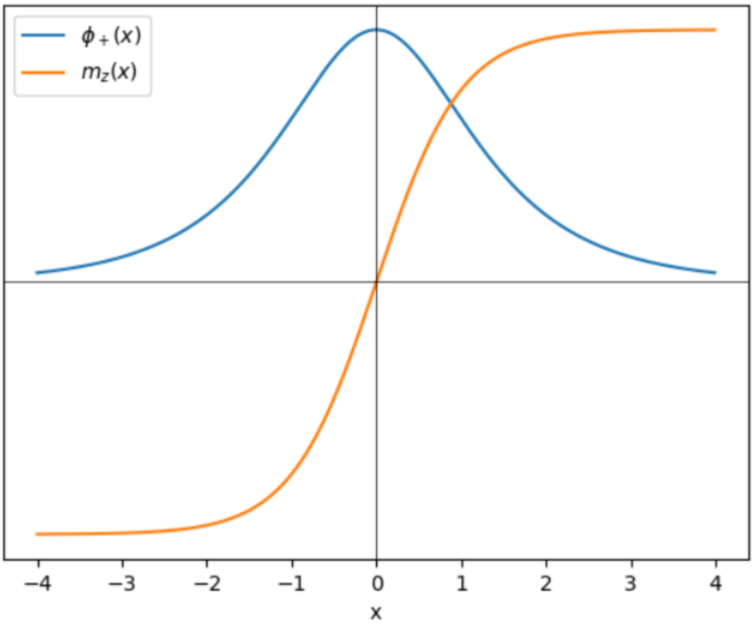

Figure 10 – Zero-energy solution (blue) for $H_{\text{surf+Zeeman}}$ and the Zeeman field profile (mass domain) $m_z(x)/\hbar v_F = tanh(x)$ (orange). The solution is localized at the domain wall. Source: By the author.

2.2 Topological superconductivity

Now we will show how we can obtain topological superconductivity in our QAH model. The (possibly anticlimactic) way to achieve TSC in this scenario is just to add trivial superconductivity to the model. More specifically, by adding trivial superconductivity to a topological system, through proximity effect, we can obtain topological superconductivity (15,23,50,51). In practical terms, we will add the s-wave superconducting pairing $\Delta\psi^\dagger_{k\uparrow}\psi^\dagger_{-k\downarrow} + \Delta^*\psi_{-k\downarrow}\psi_{p\uparrow}$ to our Hamiltonian model[¶¶].

To write the Hamiltonian with the pairing in a convenient (matrix) form we use the Boguliubov-de Gennes formalism. This method consists in extending the Hamiltonian basis by including the operators $\psi^\dagger_{-k\sigma}$ so the pairing $\Delta\psi^\dagger_{k\uparrow}\psi^\dagger_{-k\downarrow} + \Delta^*\psi_{-k\downarrow}\psi_{p\uparrow}$ becomes matrix elements of the Bloch Hamiltonian. With the addition of the creation operators, the basis becomes $\xi_k = \left(\psi_{k\uparrow}\ \psi_{k\downarrow}\ \psi^\dagger_{-k\uparrow}\ \psi^\dagger_{-k\downarrow}\right)^T$. In addition, we recall that $\{\psi_k, \psi_{-k}\} = 0$ to write the QAH Hamiltonian with s-wave superconductivity as

---

[¶¶] a detailed derivation that justifies this approach is given in Sec. 3.2.1.

$$\begin{aligned} H &= \frac{1}{2}\sum_k \xi_k^\dagger h_{BdG}(k)\xi_k, \\ h_{BdG}(k) &= \begin{pmatrix} H_{\text{surf+Zeeman}}(k) - \mu & i\Delta\sigma_y \\ -i\Delta\sigma_y & -H^*_{\text{surf+Zeeman}}(-k) + \mu \end{pmatrix}, \end{aligned} \tag{2.18}$$

where the $\frac{1}{2}$ factor comes to account for the extended (doubled) basis. Furthermore, We explicit wrote the chemical potential μ (which incorporates the term C). Here, we also choose a gauge such as $\Delta \in \mathbb{R}$. The upper and lower diagonal block in $h_{BdG}(k)$ are usually called the electron (or particle) and hole subspaces, which form the Nambu space.

To prove that h_{BdG} is indeed a topological superconductor we will show that this Hamiltonian is equivalent to a $p + ip$ superconductor, which is known for hosting topological modes at boundaries (5) or at vortices (7); then, we explicitly calculate these possible boundary modes and discuss some of their properties.

The first part is naturally done by performing a basis transformation. In particular, we go to the basis that diagonalize (15) the normal part H_{surf} of h_{BdG},

$$\psi_{k\pm} = \frac{\psi_{\uparrow k} \pm e^{-i\phi_k}\psi_{\uparrow k}}{\sqrt{2}}, \tag{2.19}$$

with $\phi_k = \tan^{-1}(k_x/k_y)$. Now we write the superconducting pairing $\Delta\psi^\dagger_{k\uparrow}\psi^\dagger_{-k\downarrow} + \Delta^*\psi_{-k\downarrow}\psi_{p\uparrow}$ in this new basis, using that

$$\psi_{\uparrow k} = \frac{\psi_{k+} + \psi_{k-}}{\sqrt{2}}, \tag{2.20}$$

$$\psi_{\downarrow k} = e^{i\phi_k}\frac{\psi_{k+} - \psi_{k-}}{\sqrt{2}}, \tag{2.21}$$

we have $\Delta\psi^\dagger_{k\uparrow}\psi^\dagger_{-k\downarrow} + h.c. \longrightarrow \frac{\Delta}{2}e^{i\phi_k}(c^\dagger_{k+}c^\dagger_{-k+} - c^\dagger_{k-}c^\dagger_{-k-}) + h.c.$. Through the identification $\sin\phi_k = p_x$ and $\cos\phi_k = p_y$ we see that we have a $p + ip$ superconducting pairing (15), i.e. $\Delta(k) \propto k_a + ik_b$ for two orthogonal directions a and b.

Next, we will show how to create chiral and helical Majorana edge states by creating domains using inhomogeneous Zeeman and/or superconducting pairings.

2.2.1 Majorana edge states

Here, we consider the possibility of having spatial dependence on the mass gap term, i.e., the superconducting pairing function $\Delta = \Delta(x')$. We will also keep the possibility of having an inhomogeneous Zeeman term $m_z(x')$. Again, taking $k_y = 0$, we look for zero-energy solutions for

$$h_{BdG}(x', k_y = 0) = \begin{pmatrix} \frac{m_z(x')}{\hbar v_F} & -\partial_{x'} & 0 & \frac{\Delta(x)}{\hbar v_F} \\ \partial_{x'} & -\frac{m_z(x')}{\hbar v_F} & -\frac{\Delta(x')}{\hbar v_F} & 0 \\ 0 & -\frac{\Delta(x')}{\hbar v_F} & -\frac{m_z(x')}{\hbar v_F} & \partial_{x'} \\ \frac{\Delta(x')}{\hbar v_F} & 0 & -\partial_{x'} & \frac{m_z(x')}{\hbar v_F} \end{pmatrix}. \tag{2.22}$$

Moreover, we will use an *ansatz* for the solutions. We require that the solutions have the form $\gamma = \zeta(x')\chi$, where χ is a constant 4×1 spinor $(a\ b\ c\ d)^T$ and $\zeta(x')$ a function of x to be determined. We also impose that the solutions represent a Majorana state, i.e. $\gamma = \gamma^\dagger$. Combining both conditions, we obtain that the spinor must be either

$$\left(\psi_{\pm\nu} + \psi^\dagger_{\pm\nu}\right), \tag{2.23}$$

or

$$i\left(\psi_{\pm\nu} - \psi^\dagger_{\pm\nu}\right), \tag{2.24}$$

where $\psi_{\pm\nu}$ is a linear combination of $\psi_\uparrow$ and $\psi_\downarrow$ that is a solution of $\sigma_\nu \psi_{\pm\nu} = \pm\psi_{\pm\nu}$ for $\nu = x, y, z$, e.g. $\psi_{+x} = \psi_\uparrow + \psi_\downarrow$.

By using this *ansatz*, we write $h_{BdG}\gamma(x', k_y = 0) = 0$ as

$$b\partial_{x'}\zeta(x') = (a\frac{m_z(x')}{\hbar v_F} + d\frac{\Delta(x')}{\hbar v_F})\zeta(x'); \tag{2.25}$$

$$a\partial_{x'}\zeta(x') = (b\frac{m_z(x')}{\hbar v_F} + c\frac{\Delta(x')}{\hbar v_F})\zeta(x'); \tag{2.26}$$

$$d\partial_{x'}\zeta(x') = (c\frac{m_z(x')}{\hbar v_F} + b\frac{\Delta(x')}{\hbar v_F})\zeta(x'); \tag{2.27}$$

$$c\partial_{x'}\zeta(x') = (d\frac{m_z(x')}{\hbar v_F} + a\frac{\Delta(x')}{\hbar v_F})\zeta(x'). \tag{2.28}$$

Now we look for solutions obeying the constrains from our ansatz. In fact, we only detail the calculations for the solutions of σ_x ($\nu = x$) because the remaining possibilities lead to $\zeta(x') = 0$, i.e. trivial solutions.

Let us start by looking at the spinor part of the possible solutions:

$$\begin{aligned} \psi_{+x}(x') + \psi^\dagger_{+x}(x') &\implies a = b = c = d = 1; \\ \psi_{-x}(x') + \psi^\dagger_{-x}(x') &\implies a = c = 1 \text{ and } b = d = -1; \\ i(\psi_{+x}(x') - \psi^\dagger_{+x}(x')) &\implies a = b = i \text{ and } c = d = -i; \\ i(\psi_{-x}(x') - \psi^\dagger_{-x}(x')) &\implies a = d = i \text{ and } b = c = -i. \end{aligned} \tag{2.29}$$

Inserting these constants into the differential equations and solving them gives us the following solutions (up to normalization):

$$\gamma_1(x') = (\psi_{+x} + \psi_{+x}^\dagger)\ \exp\left(\frac{1}{\hbar v_F}\int_0^{x'} m_z(u) + \Delta(u)du\right); \tag{2.30}$$

$$\gamma_2(x') = (\psi_{-x} + \psi_{-x}^\dagger)\ \exp\left(\frac{1}{\hbar v_F}\int_0^{x'} (\Delta(u) - m_z(u))du\right); \tag{2.31}$$

$$\gamma_3(x') = i(\psi_{+x} - \psi_{+x}^\dagger)\ \exp\left(\frac{1}{\hbar v_F}\int_0^{x'} (-\Delta(u) + m_z(u)du\right); \tag{2.32}$$

$$\gamma_4(x') = i(\psi_{-x} - \psi_{-x}^\dagger)\ \exp\left(\frac{1}{\hbar v_F}\int_0^{x'} (-\Delta(u) - m_z(u))du\right). \tag{2.33}$$

Thus, depending on the spatial profile of $\Delta(x')$ and $m_z(x')$, some solutions will diverge (not physical), in the same spirit of what we discussed in Sec. 2.1.3 about the QAH edge states. In passing, we note that if we take $\Delta(x) = 0$, we get back the QAH solutions but in the BdG basis, i.e.

$$\gamma_1(x') = (\psi_{+x} + \psi_{+x}^\dagger)\ \exp\left(\frac{1}{\hbar v_F}\int_0^{x'} m_z(u)du\right); \tag{2.34}$$

$$\gamma_2(x') = (\psi_{-x} + \psi_{-x}^\dagger)\ \exp\left(-\frac{1}{\hbar v_F}\int_0^{x'} m_z(u)du\right); \tag{2.35}$$

$$\gamma_3(x') = i(\psi_{+x} - \psi_{+x}^\dagger)\ \exp\left(\frac{1}{\hbar v_F}\int_0^{x'} (m_z(u))du\right); \tag{2.36}$$

$$\gamma_4(x') = i(\psi_{-x} - \psi_{-x}^\dagger)\ \exp\left(-\frac{1}{\hbar v_F}\int_0^{x'} (m_z(u)du\right). \tag{2.37}$$

If we consider that the solutions with $\exp\left(\frac{1}{\hbar v_F}\int_0^{x'} (m_z(x'))du\right)$ are physical, we can rewrite them as

$$\phi(x') = (\gamma_1(x') - i\gamma_3(x')) = \psi_{+x} \exp\left(\frac{1}{\hbar v_F}\int_0^{x'} (m_z(u))du\right) \tag{2.38}$$

and the redundant BdG solution,

$$\phi(x')^\dagger = (\gamma_1(x') + i\gamma_3(x')) = \psi_{+x}^\dagger \exp\left(\frac{1}{\hbar v_F}\int_0^{x'} (m_z(u))du\right). \tag{2.39}$$

On the other hand, if we take $m_z(x') = 0$, only two solutions represent real quantum states; for instance, if we consider $\Delta(x')/\hbar v_F = tanh(x')$, only

$$i(\psi_{+x} - \psi^{\dagger}_{+x})e^{-ln(cosh\ x')}, \tag{2.40}$$

$$i(\psi_{-x} - \psi^{\dagger}_{-x})e^{-ln(cosh\ x')}, \tag{2.41}$$

are physical solutions. In this scenario, when we have two good solutions (for $\Delta \neq 0$), we say that they are helical Majorana edge states. The adjective *helical* is used here to emphasize that when $k_y \neq 0$, one of the states propagates along one direction while the other goes in the opposite direction. Moreover, the spin of these edge states is locked with the propagation direction.

The other case that we will explore is when we have only induced superconductivity $\Delta(x')$ in one region and only a Zeeman field $m_z(x')$ in another region of the surface, e.g. $\Delta(x') = \Delta\theta(x')$ and $m_z(x') = m_z\theta(-x')$, where $\theta(x')$ is the Heaviside step function. With these considerations, only one of the four solutions will represent a quantum state, e.g., only

$$\gamma(x') = i(\psi_{-x} - \psi^{\dagger}_{-x})\ \exp\left(\frac{1}{\hbar v_F}\int_0^{x'}(-\Delta(u) - m_z(u))du\right)$$

would be a physical solution, i.e., would not diverge. We call this solution a *chiral* Majorana edge state, in contrast with the *helical* pair, i.e., instead of two counter-propagating (*helical*) solutions, there is only one solution that propagates in one direction.

Besides the number of states bounded to a domain wall, there are other differences between *chiral* and *helical* states. Namely, there is a distinction concerning time-reversal symmetry: in the *helical* case, TRS is preserved because $m_z(x') = 0$ is required. Whereas for the *chiral* case, we need a Zeeman field to leave just one physical state and therefore TRS needs to be broken. Furthermore, the *chiral* edge state has a practical interest since it could be used to create topological qubits through the braiding of chiral Majoranas fermions (24).

Note that, with the exception of the zero-energy case where $\gamma = \gamma^{\dagger}$, these edge states are indeed fermions (24), i.e., for a generic $k_y \neq 0$ (i.e., generic energy) the usual fermionic commutation relations are satisfied and $\gamma^{\dagger}_{k_y} = \gamma_{-k_y}$ instead of $\gamma^{\dagger}_{k_y} = \gamma_{k_y}$.

Another point that will be discussed in the next chapter, when we introduce the lattice version of this model, is how the bulk-edge correspondence emerges here. Straightforwardly, the problem that we will address is how to predict what happens at a given interface (with vacuum) in terms of edge states, by only looking at the bulk Hamiltonian.

Last but not least, there is another important feature of the *chiral* Majorana edge state that we will use to distinguish them from the Majorana corner states when we discuss the MCS in Ch. 4. That is, the conductance through one Majorana edge state is predicted to be $e^2/2h$ in a two-terminal measurement. We will not reproduce the calculation that yields this result here. the reader can find the calculation in Ref. (39).

2.3 Lattice model

To build a proper Hamiltonian model for the numerical calculations, we need to discretize the continuum model. Instead of doing $k_i \to \partial_i$ and using the finite differences method to numerically deal with the derivatives, we will put the Hamiltonian h_{BdG} in a fictitious lattice, c.f. (52). To this end, we must create periodicity in our model. An *ad hoc* way (justified via the tight-binding method) to do this is to map

$$k_i \longrightarrow \frac{1}{a}\sin(k_i a), \tag{2.42}$$

$$k_i^2 \longrightarrow \frac{2}{a^2}(1-\cos(k_i a)), \tag{2.43}$$

where ‘a’ is the lattice spacing. Notice that the lattice version gives the continuum model in the long wave length limit $k_i a \approx 0$.

Although our mapping works just fine, one could argue that k_i^2 should be mapped into $\frac{1}{a^2}\sin(k_i a)^2$, which would also give us back the continuum model in the same limit. However, using $\frac{1}{a^2}\sin(k_i a)^2$ corresponds to on site and next-nearest-neighbor couplings in real space***, instead of the simpler nearest-neighbor couplings from the $\frac{2}{a^2}(1-\cos(k_i a))$ version (52).

2.3.1 Fermion doubling and Wilson mass

Before we apply the previous mapping to our model for a topological superconductor, there is an important problem that must be addressed and solved: the so-called “fermion doubling” (53,54). Notice that if we transform a continuum Hamiltonian that is linear in momentum, something undesirable happens: an additional fictitious “gap” closing point appears at $k_i = \pi/a$, in the Brillouin zone. This is a problem because we would have doubled states for any energy, i.e. the dispersion would be always wrong if we wanted to look at a given energy range, Fig. 11. Unfortunately, energy resolution (near zero) is important to us, as we want to look at the density of states, quantum transport, etc.

***During the representation transformation, we Fourier transform $\sin(k_i a)^2$ to obtain $\delta(x_i + 2) + \delta(x_i - 2)$ corresponding next-nearest-neighbor coupling.

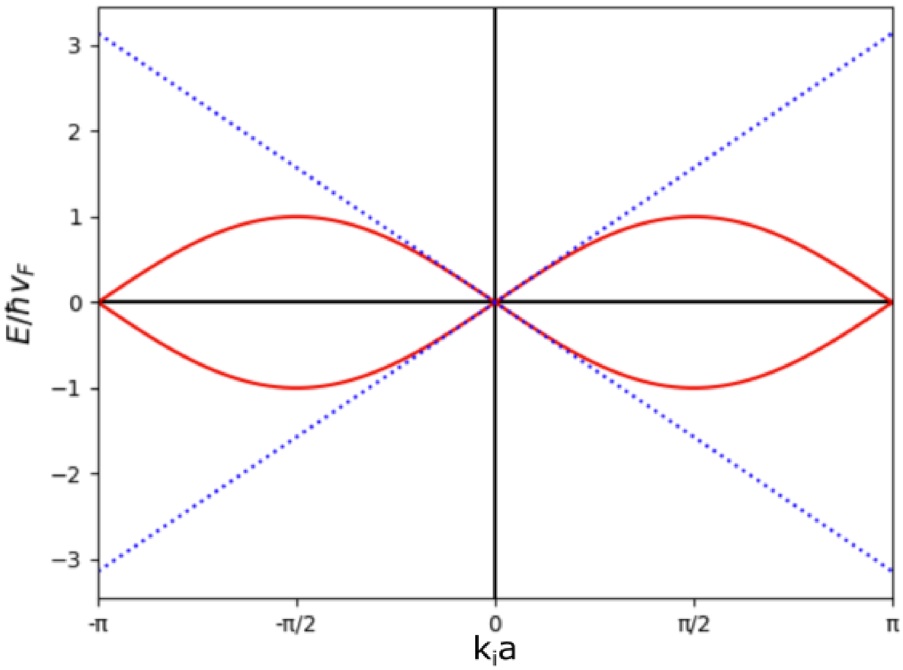

Figure 11 – Energy dispersions of a continuum Dirac Hamiltonian (blue) and its lattice version (red). At any given energy, the lattice model shows four states, while the continuum model only has two, this is the so-called fermion doubling problem. Source: By the author.

The pessimistic reader may be thinking that our method of creating a lattice version of a continuum model is doomed, as we study a Dirac like Hamiltonian (with superconductivity). However, there is a way to circumvent this problem: the introduction of the Wilson mass term, *c.f* (53,54) and references therein. The idea is to add an *ad hoc* term in our Hamiltonian that will move those states near the edge of the Brillouin zone. Thus making the lattice Hamiltonian consistent with the continuum model for small k (long wave length limit). In our 2D scenario, this term is

$$\frac{2W}{a^2}\sum_{i=x,y}(1-cos(k_i a))\,\sigma_z, \tag{2.44}$$

where W is a constant with a value such that the energy scale of this term is $\sim \hbar v_F$ (55). Note that this term has the continuum counterpart $Wk^2\sigma_z$. Moreover, for $k_i \to 0$, this term goes to 0; while for $k_i \to \pi/a$, it goes to $2W/a^2$ and will introduce a gap at that point.

As the reader may have imagined, adding this *ad hoc* term in a Hamiltonian comes at a price. The Wilson mass “trick” takes its toll in the form of a symmetry breaking. For our model, it breaks time reversal symmetry[†††], which is a small price to pay, because we already took into account the possibility of breaking TRS with a Zeeman field, $\mu_z\sigma_z$.

[†††] note that the Wilson term is even in k, as we argued in 2.1.3, this means that this term breaks TRS

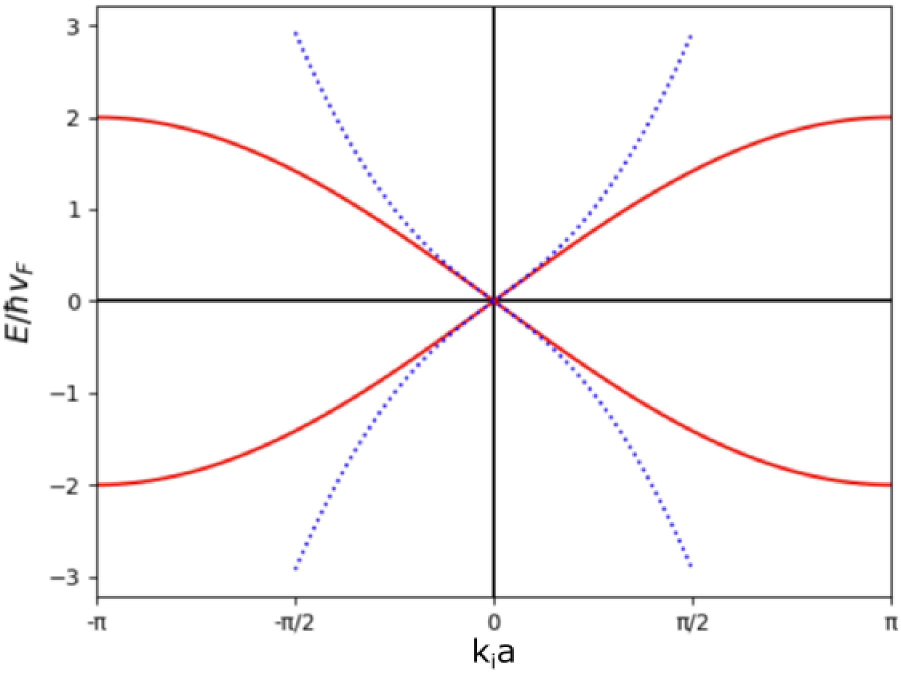

Figure 12 – Energy dispersion for the continuum Dirac model in dotted blue, and for the lattice model with the Wilson mass $W = \hbar v_F a^2/2$ in red. Now the states near $k_i a = \pi$ have been lifted and both models agree for small energy. Source: By the author.

In light of works as Ref. (56) we can imagine that this term comes from a k-dependent version of the Zeeman field, where this dependence would come from the gyromagnetic factor $g(k)$ (57). Another way to frame this term is to see it as coming from considering (which we do not describe in our model) another parallel surface that interacts with our surface and hybridizes their levels, generating an effective term like in Eq. 12. A detailed and formal description of this second picture can be found in Sec. 3.2 of Ref. (58).

2.3.2 Phase diagram

Now that we have our lattice Hamiltonian, following what we did for the continuum case in Sec. 2.2, we can write its BdG form

$$\tilde{H} = \sum_k \xi_k^\dagger \begin{pmatrix} h_{\text{lat}}(k) - \mu & \Delta i\sigma_y \\ \Delta i\sigma_y & -h_{\text{lat}}^*(-k) + \mu \end{pmatrix} \xi_k, \tag{2.45}$$

with the normal part

$$h_{\text{lat}}(k) = \frac{\hbar v_F}{a}(\sigma_x \sin k_y a - \sigma_y \sin k_x a) + \left[m_z + \frac{2W}{a^2}(2 - \cos k_x a - \cos k_y a)\right]\sigma_z, \tag{2.46}$$

where we recall that m_z is an out-of-plane Zeeman field. We can look for the possible ordinary (i.e., first order) topological phases that emerge in this system (having in mind the possible edge states that we calculated) by looking at bulk bands properties. This analysis, which was first done by Qi *et al.* (1) in this type of junction, is important to us because when we discuss the emergence of Majorana corner states, we will see that they are not predicted by the behavior of the bulk bands

Often, the main aspect investigated in ordinary topological materials is the possibility of closing and reopening a bulk gap by changing parameters of the model. The importance of this gap closing is that the set of parameters making this system gapless separates regions with different “band topologies" and therefore different topological phases. It is relevant to highlight that unless the bulk gap is closed between two points in the parameter space, they can be adiabatically connected and hence they are still in the same topological phase.

Here, by “different band topologies” we mean that at least one bulk topological property (invariant) of the band structure is different in different regions. In addition to this bulk mathematical distinction, there is a physical effect in finite geometries: the emergence of edge states (bulk-edge correspondence). In our model, the invariant that distinguishes the topology of the system for a given set of parameters is the total Chern number, which we calculate in Appendix B.

Due to the calculation that we did considering domains in the pairing function or Zeeman field, Sec. 2.2.1, we can expect three different topological phases. Each one of them corresponding to the different behaviors at an interface (with vacuum): either one or a pair of chiral Majorana edge states, or no edge states (trivial phase). Here, notice that instead of considering the possibility of a helical pair of edge states, we considered a pair of chiral Majoranas. This slight modification is due to the presence of the Wilson mass, which breaks TRS.

The equation that tells us when the bands are gapless, as shown in Ref. (1), is $\mu^2 + \Delta^2 = m_z^2$. In addition, for $\Delta = 0$ our system is mapped into the Chern insulator(46), which has known phases: normal insulator ($m_z > 0$) and QAH phase ($m_z < 0$) (58). As a topological phase transition requires a gap closing, we will see which regions in the parameter (with $\Delta \neq 0$) space are adiabatically connected to the known phases for $\Delta = 0$.

First, we notice that if $\mu > |m_z|$ and $\Delta = 0$ then the chemical potential lies within a band. Hence we have a metallic phase that is not connected to any other phase because it is gapless. Now we look at the cases with $\mu < |m_z|$: $m_z > 0$ and $m_z < 0$. The first scenario, with $m_z > 0$ is the trivial (normal) insulator, hence if we turn a superconducting pairing, such as we keep $\mu^2 + \Delta^2 < m_z^2$, the system remains in a trivial phase.

On the other hand, if $m_z < 0$ and $\Delta = 0$ we have the QAH phase and following the same idea from the trivial case, we can connect the QAH phase to the region where $\mu^2 + \Delta^2 < m_z^2$ (for $m_z < 0$) without closing the gap. Due to this property, we expect that

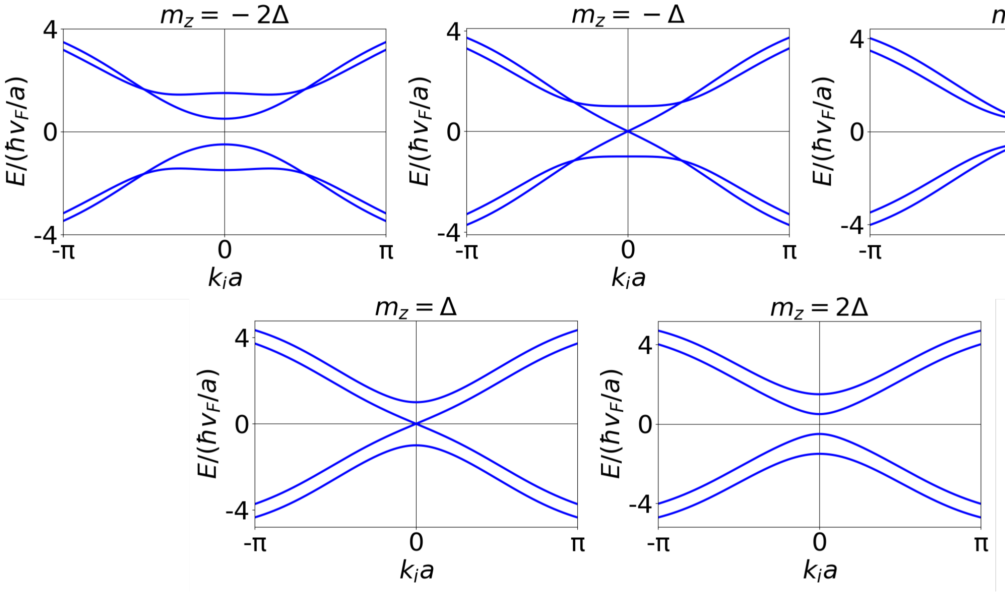

Figure 13 – Dispersion relation for different Zeeman fields m_z showing the closing points of the gap at $m_z = \pm\Delta$ (as $\mu = 0$) and the gapped regions in between, which are in different topological phases: a pair of chiral Majoranas ($m_z = -2\Delta$); a single chiral Majorana ($m_z = 0$) and trivial phase ($m_z = 2\Delta$). Here $\Delta = \hbar v_F/2a$ and $W = \hbar v_F a/2$. Source: By the author.

the QAH will be connected to a topological superconducting phase, however we have two possibilities, a phase with either: a single chiral Majorana or a pair of chiral edge states. To see which one corresponds to the $\mu^2 + \Delta^2 < m_z^2$ (for $m_z < 0$) region, we will present an intuitive argument[‡‡‡] next.

We know that this region in the parameter space is adiabatically connected to the QAH, i.e., by taking $\Delta \to 0$ we can go back to the QAH phase without closing the gap. We also know that the QAH has a Dirac fermion edge state (Sec. 2.1.3) and that this fermion corresponds to two Majorana fermions (5). Therefore, we can argue that the phase that is connected to the QAH phase is the one that hosts two Majorana states. Moreover, by exclusion, the region where $\mu^2 + \Delta^2 > m_z^2$ must correspond to the phase that hosts a single chiral Majorana edge state.

[‡‡‡] a more formal approach can be found in Ref. (1) and in Appendix B of this dissertation.

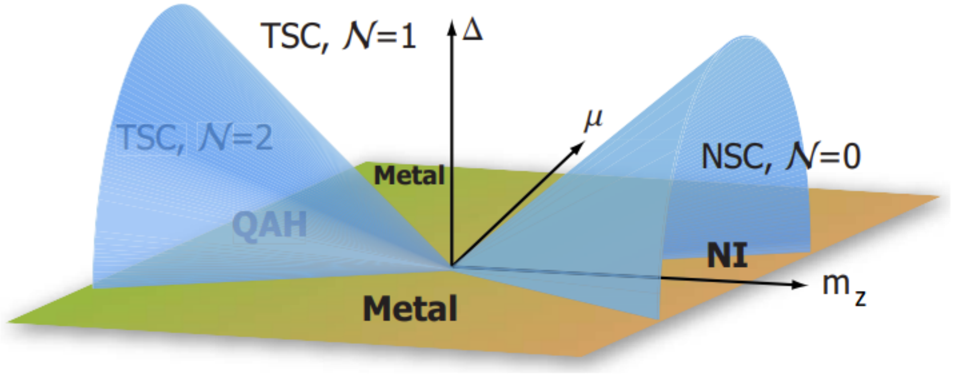

Figure 14 – Phase diagram showing the possible topological phases and their topological index (*c.f.* Appendix B). The blue cones show the condition $\mu^2 + \Delta^2 = m_z^2$, where the system is gapless. Source: Adapted from QI *et al.*(1).

2.3.3 Real space lattice model

Now that we took care of the fermion doubling problem and have some understanding of the bulk spectra, we will write the Hamiltonian in the real space representation. This is important because we want to look at a finite square geometry version of our Hamiltonian to search for the Majorana corner states. In the case of a finite system, k is no longer a good quantum number and therefore we need to go to the real space representation. To this end, we do the transformation for the fermionic operators

$$c_{\vec{r},\sigma} = \frac{1}{\sqrt{V}} \sum_{\vec{k}} c_{\vec{k},\sigma} e^{i\vec{k}\cdot\vec{r}}, \tag{2.47}$$

with $\vec{r} = (i,j)$ being a discrete real space vector in the lattice and σ the spin.

By using the relation for $c_{\vec{r},\sigma}$ and $c^\dagger_{\vec{r},\sigma}$ and taking the limit $\sum_{\vec{k}} \rightarrow \frac{V}{(2\pi)^2}\int d^2k$, we can write the normal part of our Hamiltonian model $\tilde{H}$ (Eq. 2.45) in the real space representation

$$\begin{aligned} H_{\text{lat}} = \sum_{i,j} \hbar v_f \frac{i}{2a} & \left[c^\dagger_{(i,j-1)\uparrow} c_{(i,j)\downarrow} - c^\dagger_{(i,j+1)\uparrow} c_{(i,j)\downarrow} + h.c\right] \\ -\hbar v_f \frac{1}{2a} & \left[c^\dagger_{(i-1,j)\uparrow} c_{(i,j)\downarrow} - c^\dagger_{(i+1,j)\uparrow} c_{(i,j)\downarrow} + h.c\right] \\ +(4\frac{W}{a^2} + \lambda) & \left[c^\dagger_{(i,j)\uparrow} c_{(i,j)\uparrow} - c^\dagger_{(i,j)\downarrow} c_{(i,j)\downarrow}\right] \\ -\frac{W}{a^2} & \left[c^\dagger_{(i+1,j)\downarrow} c_{(i,j)\uparrow} + c^\dagger_{(i,j+1)\downarrow} c_{(i,j)\uparrow} + h.c.\right]. \end{aligned} \tag{2.48}$$

Once we have Eq. 2.48, the BdG version with the superconducting pairing term is found by transforming the superconducting terms[§§§] into the real space representation and writing the matrix form of $\tilde{H}$ in the basis $\Theta = (c_{(1,1)\uparrow},\ c_{(1,1)\downarrow},\ c_{(2,1)\uparrow}, \ldots, c_{(N,1)\downarrow},\ c_{(1,2)\uparrow}, \ldots, c_{(N,2)\downarrow},\ \ldots, c_{(N,M)\downarrow}, c^{\dagger}_{(1,1)\uparrow}, \ldots, c^{\dagger}_{(N,M)\downarrow})$, where N and M are the number of sites in x and y directions,

$$\tilde{H} = \frac{1}{2}\Theta^{\dagger} \begin{pmatrix} h_{\text{lat}} & \Delta i\sigma_y \otimes \mathbf{I}_{(NM)} \\ \Delta i\sigma_y \otimes \mathbf{I}_{(NM)} & -h^{*}_{\text{lat}} \end{pmatrix} \Theta. \tag{2.49}$$

The symbol $\mathbf{I}_{(NM)}$ represents the $(NM) \times (NM)$identity matrix in the lattice Hilbert subspace and h_{lat} is given by $h^{\sigma,\sigma'}_{\text{lat}}[(i,j),(i',j')] = \langle 0|\, c_{(i',j')\sigma'} H_{\text{lat}} c^{\dagger}_{(i,j)\sigma}\, |0\rangle$, where $|0\rangle$ is the empty (vacuum) state.

This lattice version in real space of our model Hamiltonian (Eq. 2.49) for a QAH-SC junction will be the one that we will use to investigate the emergence of the Majorana corner states and calculate their properties (e.g., transport signatures) in Ch. 4. However, the bulk version (i.e., k-space representation) in Eq. 2.45 will also be useful to us as we will use it to calculate the symmetries of $\tilde{H}$. This will be important to indicate if the MCS are protected by any of these symmetries or not. All these properties will require techniques to perform the calculations. We will develop the necessary techniques in the next chapter.

[§§§] we consider s-wave superconductivity, thus the pairing terms are momentum independent and just couple electron and hole degrees of freedom on a given site.

3 METHODS

Now that we have described and defined the model that we want to investigate, we will develop the tools that we will use in our investigation.

We begin by doing a symmetry analysis of our lattice model, i.e., we look at the symmetries present or absent in our Hamiltonian, Eq. 2.45. This analysis is important later on when we discuss the emergence of Majorana corner states. We want to know whether these states are protected by any of these symmetries, i.e. whether preserving a symmetry implies in the preservation of the corner modes at zero-energy.

Next, we move on to the Non-equilibrium Green's functions (NEGF). This topic is extensive enough to inspire entire books, c.f. (59), developing applications and theory, e.g. Keldysh (60) and Kadanoff and Bayn (61). As no one would enjoy a detour that big, I will content myself to just define the main concepts of NEGF and how we extract useful information from them. For us, useful information will be limited to: (local) density of state (or spin) and single particle transport quantities, e.g. linear conductance.

3.1 Symmetry analysis of the lattice model

With our lattice Hamiltonian,

$$\tilde{H} = \sum_k \xi_k^\dagger \begin{pmatrix} h_{\text{lat}}(k) - \mu & \Delta i\sigma_y \\ \Delta i\sigma_y & -h^*_{\text{lat}}(-k) + \mu \end{pmatrix} \xi_k, \tag{3.1}$$

$$h_{\text{lat}}(k) = \frac{\hbar v_F}{a}(\sigma_x \sin k_y a - \sigma_y \sin k_x a) + \left[m_z + \frac{2W}{a^2}\left(2 - \cos k_x a - \cos k_y a\right)\right]\sigma_z, \tag{3.2}$$

at hand, we will explore its symmetries (spatial and non-spatial). Here we recall that our basis is $\xi_k = \left(\psi_{k\uparrow}\ \psi_{k\downarrow}\ \psi^\dagger_{-k\uparrow}\ \psi^\dagger_{-k\downarrow}\right)^T$.

Note that $h_{\text{lat}}(k)$ is the normal part of the Bloch Hamiltonian with superconductivity. However, besides particle-hole, which is enforced by the BdG formalism, we can use the normal part

$$\tilde{H}_{\text{lat}} = \sum_k \psi_k^\dagger h_{\text{lat}}(k)\psi_k \tag{3.3}$$

to explore the symmetries of $\tilde{H}$. We can choose to do our symmetry analysis this way because the s-wave pairing is transformed trivially under any other symmetry, i.e., it does not break TRS neither spatial symmetries because it is spatially uniform.

We start our analysis by stating a fact that we already mentioned in the previous section and chapter: time-reversal symmetry is broken in this model. As we discussed in Sec. 2.1.3, even terms in k proportional to any Pauli matrix break TRS in a Dirac Hamiltonian. Here all the terms proportional to σ_z are even and therefore TRS is broken. A direct verification of this fact can be done by calculating* that $[\tilde{H}_{\text{lat}}, \mathcal{T}] \neq 0$, where $\mathcal{T} = -i\sigma_y\mathcal{K}$ is the representation of the TR operation, with $\mathcal{K}$ being complex conjugation. Furthermore, as we have particle-hole symmetry but not time-reversal, their product (which is the chiral symmetry) is not a symmetry of our Hamiltonian.

In addition to the non-spatial symmetries, we need to look at the symmetries from the lattice and the products between absent symmetries, e.g., if the Hamiltonian does not have symmetries A and B, $[A, \tilde{H}_{\text{lat}}]$ and $[B, \tilde{H}_{\text{lat}}]$ are *not* zero, however it is still possible to have $[AB, \tilde{H}_{\text{lat}}] = 0$.

Spatial symmetries

As we have a square lattice, it is natural to look at the dihedral group D_4, which consists of 90° rotations and reflections through the directions parallel to the square sides or through the diagonals.

The first operation of D_4 that we will study are 90° rotations, which form the C_4 subgroup. In Cartesian coordinates, this subgroup maps $(x, y) \mapsto (-y, x)$. Therefore, its action on the creation (or annihilation) operators is

$$\mathcal{C}_4\psi_{(x,y)}\mathcal{C}_4^{-1} = \psi_{(-y,x)}, \tag{3.4}$$

where the calligraphic $\mathcal{C}_4$ is a representation of the group's action, i.e., it is a 2×2 matrix.

As we will analyze our Hamiltonian in k-space, we note that the action of $\mathcal{C}_4$ in $\psi_{(k_x,k_y)}$ is

$$\begin{aligned}\mathcal{C}_4\psi_{(k_x,k_y)}\mathcal{C}_4^{-1} &= \frac{1}{\sqrt{V}}\sum_{(x,y)}\mathcal{C}_4\psi_{(x,y)}\mathcal{C}_4^{-1}e^{-i(k_xx+k_yy)}\\ &= \frac{1}{\sqrt{V}}\sum_{(x,y)}\psi_{(-y,x)}e^{-i(k_xx+k_yy)}\\ &= \frac{1}{\sqrt{V}}\sum_{(x,y)}\psi_{(-y,x)}e^{-i(k_xx+k_yy)}\\ &= \frac{1}{\sqrt{V}}\sum_{(x',y')}\psi_{(x',y')}e^{-i(k_xy'-k_yx')}\\ &\implies \mathcal{C}_4\psi_{(k_x,k_y)}\mathcal{C}_4^{-1} = \psi_{(k_y,-k_x)}.\end{aligned} \tag{3.5}$$

To verify if C_4 is indeed a symmetry of our Hamiltonian, we assume that it is and see if this assumption leads us to a contradiction or not. Let us then assume that C_4 is a

---

[*] alternatively, one can show (46) that not having TRS is equivalent to violating the equality $\mathcal{T}h_{\text{lat}}(k)\mathcal{T}^{-1} = h_{\text{lat}}(-k)$.

symmetry of our Hamiltonian, hence $[\mathcal{C}_4, H_{\text{lat}}] = 0$, i.e., $\mathcal{C}_4 H_{\text{lat}} \mathcal{C}_4^{-1} = H_{\text{lat}}$, which implies that

$$\sum_k \mathcal{C}_4 \psi_k^\dagger h(\vec{k})_{\text{lat}} \psi_k \mathcal{C}_4^{-1} = \sum_k \psi_k^\dagger h(\vec{k})_{\text{lat}} \psi_k, \tag{3.6}$$

and can be rewritten, by using that $\mathcal{C}_4 \mathcal{C}_4^{-1} = 1$, as

$$\begin{aligned}
&\sum_k \mathcal{C}_4 \psi_k^\dagger \mathcal{C}_4^{-1} \;\; \mathcal{C}_4 h_{\text{lat}}(\vec{k}) \mathcal{C}_4^{-1} \;\; \mathcal{C}_4 \psi_k \mathcal{C}_4^{-1} = \sum_k \psi_k^\dagger h(\vec{p}) \psi_k; \\
&\Rightarrow \sum_k \psi^\dagger_{(k_y,-k_x)} \mathcal{C}_4 h_{\text{lat}}(\vec{k}) \mathcal{C}_4^{-1} \psi_{(k_y,-k_x)} = \sum_k \psi_k^\dagger h_{\text{lat}}(\vec{k}) \psi_k; \\
&\Rightarrow \sum_k \psi^\dagger_{(k_y,-k_x)} \mathcal{C}_4 h_{\text{lat}}(\vec{k}) \mathcal{C}_4^{-1} \psi_{(k_y,-k_x)} = \sum_k \psi_k^\dagger h_{\text{lat}}(\vec{k}) \psi_k; \\
&\Rightarrow \boxed{\mathcal{C}_4 h_{\text{lat}}(\vec{k}) \mathcal{C}_4^{-1} = h_{\text{lat}}(k_y, -k_x).}
\end{aligned} \tag{3.7}$$

Since we did not do any “logical leap”, this last equation is equivalent to the statement that C_4 is a symmetry of H_{lat}. Thus, if we find an operator $\mathcal{C}_4$ such as Eq. 3.7 is satisfied, we can claim that C_4 is a symmetry of our Hamiltonian. On the other hand, if we show that there is no operator that satisfies that equation, it means that our assumption is false, hence C_4 is not a symmetry of H_{lat}.

In this particular case, it is rather intuitive that the only possibility is to have $\mathcal{C}_4 = e^{\frac{-i\alpha\sigma_z}{2}}$, for a given α , because the transformation is a rotation along the z axis. More specifically, it is a 90° rotation. It turns out to be true that $\mathcal{C}_4 = e^{-i\frac{\pi}{4}\sigma_z}$ satisfies the requirement to have C_4 as a symmetry of H_{lat}. The verification is straightforward if one recalls that $e^{-i\frac{\pi}{4}\sigma_z} = \frac{1}{\sqrt{2}}(\mathrm{I} - i\sigma_z)$ and $\sigma_x\sigma_z = -i\sigma_y$ and that $\sigma_y\sigma_z = i\sigma_x$.

Note that the C_2 group, 180° rotations[†], is a subgroup of C_4; therefore, as C_4 is a symmetry group of h_{lat}, C_2 is also a symmetry. If the reader is not convinced by this syllogism, the verification is immediate if we take $\mathcal{C}_2 = -i\sigma_z$, which is equivalent to $(\mathcal{C}_4)^2$, i.e. two consecutive 90° rotations.

Next, we look at the four reflection operations M_x, M_y, M_{x+y} and M_{x-y}, with the respective operators are $\mathcal{M}_x$, $\mathcal{M}_y$, $\mathcal{M}_{x+y}$ and $\mathcal{M}_{x-y}$. These operations are defined by their action in the spatial coordinates, $M_{\vec{r}} : \vec{r} \mapsto -\vec{r}$, e.g., $M_x : (x, y) \mapsto (-x, y)$.

To verify if any of these operations correspond to symmetries in H_{lat}, we repeat the same procedure done for C_4. We find that the equations equivalent to having these symmetries are

---

[†] which is equivalent to the inversion operation

$$\begin{aligned}
\mathcal{M}_x h_{\text{lat}}(\vec{k})\mathcal{M}_x^{-1} &= h_{\text{lat}}(-k_x, k_y),\\
\mathcal{M}_y h(\vec{k})\mathcal{M}_y^{-1} &= h_{\text{lat}}(k_x, -k_y),\\
\mathcal{M}_{x+y} h_{\text{lat}}(\vec{k})\mathcal{M}_{x+y}^{-1} &= h_{\text{lat}}(k_y, k_x),\\
\mathcal{M}_{x-y} h_{\text{lat}}(\vec{k})\mathcal{M}_{x-y}^{-1} &= h_{\text{lat}}(-k_y, -k_x).
\end{aligned} \tag{3.8}$$

Before we start looking for operators for the reflections or try to show that they do not exist, we will show a visual proof of why our Hamiltonian does *not* have any mirror symmetry. The fact that will help us to build this argument is that: any reflection in a 2D object can be thought of as a rotation in 3D around the reflection axis. Within this optic, one can see that any rotation around these axes will “flip” the out-of-plane[‡] terms, i.e., as the corresponding operators to the reflections are out-of-plane rotations, they are proportional to σ_x and σ_y, which will always change the sign of the terms with σ_z.

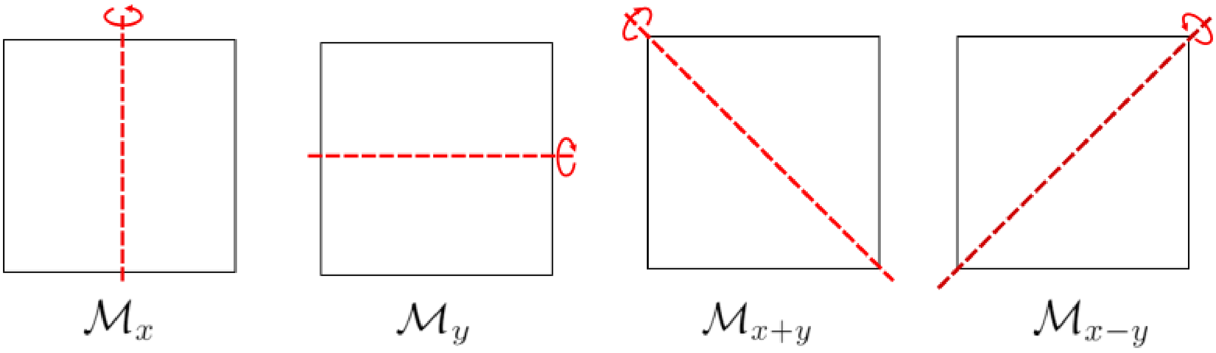

Figure 15 – Illustration of the four possible reflections symmetries in a square. It can also be seen that reflections of a 2D object can be viewed as a rotation if that object is embedded in the 3D space. Source: By the author.

We can also show that assuming any of the mirror operations to be a symmetry leads to a contradiction. For brevity, let us look only at M_x, as the same steps are valid for the remaining mirror symmetries.

Let us suppose that there exists an operator $\mathcal{M}_x$ such as $\mathcal{M}_x h(\vec{k})\mathcal{M}_x^{-1} = h_{\text{lat}}(-k_x, k_y)$ holds. This implies that,

$$\begin{aligned}
\mathcal{M}_x[&\frac{\hbar v_F}{a}(\sigma_x \sin k_y a - \sigma_y \sin k_x a) + \left[m_z + \frac{2W}{a^2}(+2 - \cos k_x a - \cos k_y a)\right]\sigma_z]\mathcal{M}_x^{-1}\\
&= \frac{\hbar v_F}{a}(\sigma_x \sin k_y a + \sigma_y \sin k_x a) + \left[m_z + \frac{2W}{a^2}(+2 - \cos k_x a - \cos k_y a)\right]\sigma_z,
\end{aligned} \tag{3.9}$$

[‡] in spin space

hence, $\mathcal{M}_x$ must map

$$\begin{aligned} \sigma_x &\mapsto \sigma_x, \\ \sigma_y &\mapsto -\sigma_y, \\ \sigma_z &\mapsto \sigma_z. \end{aligned} \tag{3.10}$$

Now, let us try to build a 2×2 operator that behaves as the mapping above requires.

The most general form of a 2×2 operator is $\vec{v} \cdot \vec{\sigma}$, with $\vec{v} = (a, b, c, d)$. The first condition is that $\mathcal{M}_x \sigma_x \mathcal{M}_x^{-1} = \sigma_x$, thus we must have $c = d = 0$. The action on σ_z is $\mathcal{M}_x \sigma_z \mathcal{M}_x^{-1} = \sigma_z$, which implies that $b = c = 0$. The remaining operation is over σ_y, $\mathcal{M}_x \sigma_y \mathcal{M}_x^{-1} = -\sigma_y$, implying that a=c=0. As we put all these conditions together, we see that $\mathcal{M}_x = 0$, which is absurd! The operator cannot be 0, as it would not satisfy $\mathcal{M}_x h(\vec{k}) \mathcal{M}_x^{-1} = h(-k_x, k_y)$, in fact it is more absurd than that because $\mathcal{M}_x$ is not even invertible. Therefore, we showed that M_x is not a symmetry of our Hamiltonian and the same can be said about the other mirror operations. In addition, the reflection around x should transform the spin operators as angular momentum operators (62), i.e., $\mathcal{M}_x \sigma_x \mathcal{M}_x^{-1} = \sigma_x$ and $\mathcal{M}_x \sigma_{y,z} \mathcal{M}_x^{-1} = -\sigma_{y,z}$ which would already be conflicting with the expected mapping of $\mathcal{M}_x$ for σ_z in Eq. 3.10.

With the analysis of the mirror operations, we exhausted the “basic” symmetries. Summarizing, our Hamiltonian H_{lat} has: PHS, C_4 and C_2 (i.e., inversion) and it lacks TRS and any mirror symmetry. However, as we mentioned in the beginning of this section, a product of two operations can be a symmetry of our Hamiltonian, although neither of the operations correspond to symmetries. Here, the products that we can investigate are between a given mirror operation and time-reversal, which are called magnetic (in-plane) reflection symmetries (63).

Magnetic mirror symmetries

We know how the creation and annihilation operators are transformed under the individual symmetries $\mathcal{T}$ and $\mathcal{M}$ (here, $\mathcal{M}$ without any subscript index represents any of the mirror operations). Hence, if we combine the action of both transformations, we find the equation that the Bloch Hamiltonian must obey to have a given $\mathcal{M}\mathcal{T}$ symmetry.

Again, let us focus on the case with the reflection along the x axis, $\mathcal{M}_x\mathcal{T}$. We know that $\mathcal{M}_x c_{(k_x,k_y)\sigma'} \mathcal{M}_x^{-1} = c_{(-k_x,k_y)\sigma'}$ and that (40) $\mathcal{T} c_{(k_x,k_y)\sigma'} \mathcal{T}^{-1} = i\sigma_y c_{(-k_x,-k_y)\sigma'}$. Combining the operations, we arrive at $(\mathcal{M}_x\mathcal{T}) c_{(k_x,k_y)\sigma'} (\mathcal{M}_x\mathcal{T})^{-1} = i\sigma_y c_{(k_x,-k_y)\sigma'}$. Performing the same steps (Eq. 3.7) as we did for the $\mathcal{C}_4$ calculation, we obtain $(\mathcal{M}_x\mathcal{T}) h_{\text{lat}}(\vec{k}) (\mathcal{M}_x\mathcal{T})^{-1} = h_{\text{lat}}(k_x, -k_y)$. Now we need to verify if this equation is true for some operator $\mathcal{M}_x$ or not.

Let us start by applying the TR operation $\mathcal{T} = -i\sigma_y\mathcal{K}$ to the Bloch Hamiltonian,

$$\begin{aligned}&\mathcal{M}_x\{\mathcal{T}[\frac{\hbar v_F}{a}(\sigma_x \sin k_y a - \sigma_y \sin k_x a) + \left[m_z + \frac{2W}{a^2}\left(+2 - \cos k_x a - \cos k_y a\right)\right]\sigma_z]\mathcal{T}^{-1}\}\mathcal{M}_x^{-1} \\ &= -\mathcal{M}_x\{-\frac{\hbar v_F}{a}(\sigma_x \sin k_y a - \sigma_y \sin k_x a) - \left[m_z + \frac{2W}{a^2}\left(+2 - \cos k_x a - \cos k_y a\right)\right]\sigma_z\}\mathcal{M}_x^{-1},\end{aligned} \tag{3.11}$$

now we need to look for an $\mathcal{M}_x$ such as,

$$\begin{aligned}-\mathcal{M}_x\{-\frac{\hbar v_F}{a}(\sigma_x \sin k_y a - \sigma_y \sin k_x a) - \left[m_z + \frac{2W}{a^2}\left(+2 - \cos k_x a - \cos k_y a\right)\right]\sigma_z\}\mathcal{M}_x^{-1} = \\ \frac{\hbar v_F}{a}(-\sigma_x \sin k_y a - \sigma_y \sin k_x a) + \left[m_z + \frac{2W}{a^2}\left(+2 - \cos k_x a - \cos k_y a\right)\right]\sigma_z.\end{aligned} \tag{3.12}$$

In this case, we find that $\mathcal{M}_x = i\sigma_x$ is the answer.

The same steps can be done to the remaining products and the conclusion will be that all the magnetic reflection operations $\mathcal{M}_x\mathcal{T}, \mathcal{M}_y\mathcal{T}, \mathcal{M}_{x+y}\mathcal{T}$ and $\mathcal{M}_{x-y}\mathcal{T}$ correspond to symmetries of H_{lat}.

3.2 Non-equilibrium Green's functions

As we mentioned at the beginning of this chapter, we will present a "practical" approach to NEGFs. In the same spirit of the Green's function in differential equation theory (64), we define the retarded Green's function for the Schrodinger equation at a given energy E for a Hamiltonian H,

$$G(E) = \lim_{\eta\to 0^+}\left(E + i\eta - H - \Sigma\right)^{-1}. \tag{3.13}$$

Here we have introduced the $i\eta$ term to shift the poles from the real axis to avoid singularities. If one had chosen the minus sign for this term, we would end up with the advanced Green's function, $G^\dagger$, which is as special as the retarded one.

The other term that we put in an *ad hoc* way (we will derive it in the next paragraph) is Σ, which represents the total self-energy. For our purposes, the self-energy effectively accounts for interactions with the environment, e.g., normal or superconducting leads coupled to the system. One could also take into account many-body interactions, e.g. electron-electron, as self-energies but we do not need to do that, since we already have an effective single particle model as derived in Ch. 2.

3.2.1 Self-energies

To elucidate the origin of the self-energy term, we perform a simplistic calculation. Let us consider a setup with one lead and a main region coupled together. We can write the Hamiltonian in terms of subspaces block matrices,

$$\mathcal{H} = \begin{pmatrix} H_L & \tau \\ \tau^\dagger & H_D \end{pmatrix}, \tag{3.14}$$

where H_L and H_D are the Hamiltonian parts in the lead and main device subspaces. The term τ connects those subspaces and couples the lead to the main part.

We will now try to find the Green's function of the relevant subspace, i.e., the main region. So we will use Eq. 3.13 and write the Green's function in terms of the subspace blocks,

$$\left[(E+i\eta)I - \begin{pmatrix} H_L & \tau \\ \tau^\dagger & H_D \end{pmatrix}\right] \begin{pmatrix} G_L & G_{LD} \\ G_{DL} & G_D \end{pmatrix} = \begin{pmatrix} I_L & \\ & I_D \end{pmatrix}, \tag{3.15}$$

where we also separated the identity matrix in the blocks.

Next, we do the matrix multiplication on the left-hand side, which gives us equations in terms of the matrix blocks,

$$((E+i\eta) - H_L)\, G_{LD} - \tau G_D = 0, \tag{3.16}$$

$$-\tau^\dagger G_{LD} + ((E+i\eta) - H_D)\, G_D = I_D, \tag{3.17}$$

and massage these equations to isolate G_D.

By defining the lead Green's function $g_L = ((E+i\eta) - H_L)^{-1}$, we find that $G_{LD} = g_L \tau G_D$. Making this identification in Eq. 3.17, let us write an expression for G_D

$$-\tau^\dagger g_L \tau G_D + ((E+i\eta) - H_D)\, G_D = I_D \tag{3.18}$$

$$\Rightarrow G_D = \Big((E+i\eta) - H_D - \tau^\dagger g_L(E)\tau\Big)^{-1}. \tag{3.19}$$

Now we define the self-energy $\Sigma(E) = \tau^\dagger g_L(E)\tau$ and identify H_D with H to regain the retarded Green's function as written in Eq. 3.13.

Another way to incorporate and interpret the self-energy is to define an effective Hamiltonian $H_{eff} = H_D + \Sigma$. The role of the self-energy in this Hamiltonian is divided in two: the Hermitian part $(\Sigma + \Sigma^\dagger)/2$ will shift the eigenenergies of the original Hamiltonian and may change the coupling between the degrees of freedom inside the device; on the other hand, the skew-Hermitian part $(\Sigma - \Sigma^\dagger)/2 \equiv \Gamma/2$, will introduce a broadening (or life-time) to H_{eff} states. Here we defined the broadening matrix Γ, which will be important when we deal with transport.

Notice that, if we know Σ, we need to invert a matrix with the size of H_D instead of $\mathcal{H}$. This fact has an important role when doing numerical calculations as it reduces considerably the computational power needed without doing any approximation on G_D.

Although calculating the exact form of the self-energy is important when modeling realistic systems[§], it can be very time-consuming (but not as much as doing the complete inversion!). To save that time, we will try to find approximate analytical expressions for the self-energies. In practice, we will trade a bit of quantitative accuracy for time, while we keep the phenomenology correct.

First, we show an expression for the normal lead and then for the superconducting one. The latter will also justify why we consider the superconductivity induced by proximity as we did in Sec. 2.2.

Normal lead self-energy

A normal lead is a trivial metal connected to our device. Therefore, we know that its corresponding self-energy Σ_N cannot introduce proximity effects into our device, e.g. spin-orbit interaction, magnetization, etc. The corresponding effect of the self-energy must be a broadening and shift in the spectra.

In a first approximation, we neglect the energy shift, because it does not change the phenomena observed in a qualitative way. Besides, we consider that the broadening is independent of energy[¶]. In other words, we take $\Sigma(E) = \Gamma/2$ with non-zero elements depending on the coupling matrix τ.

Superconducting lead self-energy

For the superconducting lead, we need to do a slightly more careful approximation before finding the expression that we will use. The superconducting lead will be a 3D s-wave superconductor, which we model using the s-wave BCS mean-field Hamiltonian, i.e.,

$$H_{SC} = \sum_{k,\sigma} \varepsilon_k c^\dagger_{k,\sigma} c_{k,\sigma} + \left(\Delta c^\dagger_{k\uparrow} c^\dagger_{-k\downarrow} + h.c.\right), \tag{3.20}$$

here $\varepsilon_k = \frac{\hbar k^2}{2m} - \mu$, and $c^\dagger_{k,\sigma}(c_{k,\sigma})$ are the usual creation (annihilation) electron operators for spin σ and momentum k. In the Bogoliubov-de Gennes formulation,

$$H_{SC} = \sum_k \varphi^\dagger_k h_{SC}(k) \varphi_k, \tag{3.21}$$

$$h_{SC}(k) = \begin{pmatrix} \varepsilon_k & i\Delta\sigma_y \\ -i\Delta\sigma_y & -\varepsilon_{-k} \end{pmatrix} \tag{3.22}$$

[§] for the reader interested in doing this kind of calculation, look the Sancho-Rubio algorithm (65), it can be very useful.

[¶] later in this section we will see that this is equivalent to considering that the lead has a constant density of states at the energy range that we are interested in.

where we choose a gauge such $\Delta \in \mathbf{R}$, without loss of generality, and the basis is $\varphi_k = \frac{1}{\sqrt{2}}\begin{pmatrix} c_{k,\uparrow} & c_{k,\downarrow} & c^\dagger_{-k,\uparrow} & c^\dagger_{-k,\downarrow}\end{pmatrix}^T$.

To obtain the self-energy, first, we calculate $g_{SC} = (E + i\eta - h_{SC}(k))^{-1}$, which we can do by directly inverting the matrix, as it is only 4×4,

$$g_{SC}(k,\omega) = \begin{pmatrix} -\frac{\omega+\varepsilon_k}{\Delta^2-\omega^2+\varepsilon_k^2} & 0 & 0 & -\frac{\Delta}{\Delta^2-\omega^2+\varepsilon_k^2} \\ 0 & -\frac{\omega+\varepsilon_k}{\Delta^2-\omega^2+\varepsilon_k^2} & \frac{\Delta}{\Delta^2-\omega^2+\varepsilon_k^2} & 0 \\ 0 & \frac{\Delta}{\Delta^2-\omega^2+\varepsilon_k^2} & \frac{\varepsilon_k-\omega}{\Delta^2-\omega^2+\varepsilon_k^2} & 0 \\ -\frac{\Delta}{\Delta^2-\omega^2+\varepsilon_k^2} & 0 & 0 & \frac{\varepsilon_k-\omega}{\Delta^2-\omega^2+\varepsilon_k^2} \end{pmatrix}, \tag{3.23}$$

with $E + i\eta \equiv \omega$. We also need to define the coupling to the main region

$$\tau_{SC} = \begin{pmatrix} \gamma & 0 & 0 & 0 \\ 0 & \gamma & 0 & 0 \\ 0 & 0 & -\gamma & 0 \\ 0 & 0 & 0 & -\gamma \end{pmatrix}, \tag{3.24}$$

where γ is a constant. For simplicity, we have considered that the main region subspace is also 4×4. If we had considered a larger subspace, the only difference would be the size of the self-energy matrix.

Recalling the self-energy definition $\Sigma_{SC} = \tau^\dagger_{SC}\; g_{SC}(k,\omega)\; \tau_{SC}$, we do this matrix product and find

$$\Sigma_{SC}(k,\omega) = \frac{|\gamma|^2}{\Delta^2 - \omega^2 + \varepsilon_k^2}\begin{pmatrix} -\omega-\varepsilon_k & 0 & 0 & \Delta \\ 0 & -\omega-\varepsilon_k & -\Delta & 0 \\ 0 & -\Delta & \varepsilon_k-\omega & 0 \\ \Delta & 0 & 0 & \varepsilon_k-\omega \end{pmatrix}. \tag{3.25}$$

So far, we did not make any simplifications or limiting assumptions for the coupled main part, but now we should make some. First, we will consider a two-dimensional main region because this is the case of our model in Ch. 2. As the superconducting lead is 3D, there is one momentum component (degree of freedom) that only exists in the superconductor, e.g. k_z. Thus we can sum over (or "trace out") that degree of freedom, so the self-energy corresponds to the contribution of the whole superconducting lead, i.e. all k_z components.

This sum will be written as an integral due to k_z being a continuum degree of freedom

$$\int dk_z \frac{1}{\Delta^2 - \omega^2 + \varepsilon_k^2} \Longrightarrow \int d\varepsilon_k \frac{dk_z}{d\varepsilon_k}\frac{1}{\Delta^2 - \omega^2 + \varepsilon^2}, \tag{3.26}$$

where we made a variable change from k_z to ε_k. Now we identify the tunneling density of states $dk_z/d\varepsilon_k = N(\varepsilon_k)$, which only depends on k_z (15) and assume that this density of states does not vary much and is approximately the tunneling DOS at the Fermi energy(15,66), i.e. $N(\varepsilon_k) \approx N(0)$. Within this approximation, we use the residue theorem and find

$$\int d\varepsilon_k \frac{dk_z}{d\varepsilon_k} \frac{1}{\Delta^2 - \omega^2 + \varepsilon^2} = N(0) \frac{\pi}{\sqrt{\Delta^2 - \omega^2}}. \tag{3.27}$$

The other terms are odd and vanish under integration. Therefore, we have an analytical expression for the superconducting lead self-energy that is independent of momentum

$$\Sigma_{SC}(\omega) = \frac{\xi}{\sqrt{\Delta^2 - \omega^2}} \begin{pmatrix} -\omega & 0 & 0 & \Delta \\ 0 & -\omega & -\Delta & 0 \\ 0 & -\Delta & -\omega & 0 \\ \Delta & 0 & 0 & -\omega \end{pmatrix}, \tag{3.28}$$

where we defined $\xi \equiv |\gamma|^2 N(0)\pi$.

As in Ref. (50), we can take the small-energy limit and consider the first-order expansion. In Dirac-like Hamiltonians (as the topological surface state derived in Sec. 2.1.2), this approximate self-energy will play the role of inducing a superconducting pairing function $\tilde{\Delta}$ and renormalizing the Fermi velocity v_F and chemical potential μ,

$$v_F \rightarrow \tilde{v_F} = \frac{v_F}{1 + \xi/\Delta}; \tag{3.29}$$

$$\mu \rightarrow \tilde{\mu} = \frac{\mu}{1 + \xi/\Delta}; \tag{3.30}$$

$$\tilde{\Delta} = \frac{\xi}{1 + \xi/\Delta}. \tag{3.31}$$

The detailed derivation of these results can be found in Appendix A.

3.2.2 Density of states

Considering that some of the readers are already familiar with (or bored by) the following common algebraic manipulations of the Green's function, I will show how to express the density of states in terms of the retarded Green's function right away and afterward do the detailed derivation.

The density of states in terms of the retarded Green's function is (67):

$$\rho(E) = -\frac{1}{\pi} Im[\mathrm{Tr}\{G(E)\}], \tag{3.32}$$

where 'Tr' is the trace operation (over all degrees of freedom).

If you are one of the readers who would like to skip the next calculations: go ahead, I take no offense. For those who want to see the origin of this expression: we start by defining the spectral representation of the retarded Green's function, which is obtained by inserting the completeness relation $I = \sum_n |\phi_n\rangle \langle\phi_n|$ twice in Eq. 3.13, where $H|\phi_n\rangle = \lambda_n |\phi_n\rangle$,

$$G(E) = \lim_{\eta\to 0^+} \sum_n \frac{|\phi_n\rangle\langle\phi_n|}{E + i\eta - \lambda_n}. \tag{3.33}$$

The identity $lim_{y\to 0}\frac{1}{x+iy} = P\frac{1}{x} - i\pi\delta(x)$, where P is the Cauchy principal value, allows us to re-write the denominator as

$$G(E) = \sum_n |\phi_n\rangle\langle\phi_n| \left(P\frac{1}{E-\lambda_n} - i\pi\delta(E-\lambda_n))\right). \tag{3.34}$$

We can already see that the second term resembles the density of states; but, first, we need to get rid of the other terms. By considering a complete basis $\sum_n |\phi_m\rangle\langle\phi_m|$, we can take the trace,

$$\begin{aligned}\mathrm{Tr}\{G(E)\} = \sum_m \langle\phi_m| G(E) |\phi_m\rangle &= \sum_{n,m} \langle\phi_m|\phi_n\rangle\langle\phi_n|\phi_m\rangle \left(P\frac{1}{E-\lambda_n} - i\pi\delta(E-\lambda_n))\right)\\ &= \sum_{n,m} \delta_{mn}\delta_{nm} \left(P\frac{1}{E-\lambda_n} - i\pi\delta(E-\lambda_n))\right)\\ &= \sum_m \left(P\frac{1}{E-\lambda_m} - i\pi\delta(E-\lambda_m))\right).\end{aligned} \tag{3.35}$$

Now, if we divide the quantity above by $-\pi$ and take the imaginary part, we identify the definition of density of states $\rho(E) = \sum_n \delta(E-\lambda_n)$ to obtain the desired equation: $\rho(E) = -\frac{1}{\pi}Im[\mathrm{Tr}\{G(E)\}]$.

Notice that if instead of taking the full trace, we took a partial trace over the degrees of freedom that are not spatial, e.g. spin, orbital, etc. and use the real space representation[‖], we would end up with the local density of states (LDOS) $\rho(r, E)$.

To illustrate the calculation of the LDOS, let us look at a simple example: a 1D chain with N sites and two orbitals[**] {a,b}. Our generic Hamiltonian and Green's function can be written in the basis $\{|\phi_1^a\rangle, |\phi_1^b\rangle, |\phi_2^a\rangle, |\phi_2^b\rangle \ldots |\phi_N^a\rangle, |\phi_N^b\rangle\}$, where the subscript is

---

[‖] we can obtain this representation by projecting the states into real space.

[**] It could be any other degree of freedom that is not spatial.

the site index and the superscript is the orbital one. Within this representation:

$$G(E) = \begin{pmatrix} g_{11}^{aa} & g_{11}^{ab} & g_{12}^{aa} & \cdots & & & \\ g_{11}^{ba} & g_{11}^{bb} & & & & & \\ g_{21}^{aa} & & g_{22}^{aa} & & & & \\ \vdots & & & g_{22}^{bb} & & & \\ & & & & \ddots & & \\ & & & & & g_{NN}^{aa} & \\ & & & & & & g_{NN}^{bb} \end{pmatrix}, \tag{3.36}$$

where the matrix elements are indexed following the Hamiltonian basis. Thus we can have diagonal elements or elements connecting different states: on-site or not and same or different orbitals, e.g., g_{12}^{aa} connects the states in the site 1 and 2 with the same orbital 'a'.

We can express the DOS in terms of matrix elements

$$\rho(E) = -\frac{1}{\pi} Im \sum_{i=1}^{N} \sum_{j=\{a,b\}} g_{ii}^{jj}, \tag{3.37}$$

and the LDOS at site 'i':

$$\rho(i, E) = -\frac{1}{\pi} Im \sum_{j=\{a,b\}} g_{ii}^{jj}, \tag{3.38}$$

.

3.2.3 **Spin texture**

We can also define a quantity that allows us to look at the real space spin texture: the local spin density

$$\rho_{s^j}(r, E) = -\frac{1}{\pi} Im \, \mathrm{Tr}\Big\{ s^j G(E) \Big\} = \sum_n s_n^j |\phi_n(r)|^2 \, \delta(E - \lambda_n). \tag{3.39}$$

Here s^j is the spin projection operator in the direction 'j' and $s_n^j \equiv \langle \phi_n | \, s^j \, | \phi_n \rangle$ is its expectation value in a given state $|\phi_n\rangle$. As the term $|\phi_n(r)|^2$ is present, we interpret the local spin density as the spin expectation value at a given position 'r' weighted by the wave-function. The derivation of 3.39 follows the same steps as the LDOS, but starting with $s^i G(E)$, instead of $G(E)$, so we will skip it.

3.2.4 **Single particle coherent transport**

Let us turn our attention to the transport quantities that we can extract from the Green's function. For these calculations, even the reader that is used to this method must be careful because the Bogoliubov-de Gennes (BdG) formulation has electrons and holes, carrying opposite charges, which is relevant for the current calculation. Besides, in the presence of superconductivity, there are Andreev processes(68,69) involving these two kinds of particles.

There are many papers that develop the NEGF in the presence of superconductivity (70–72). In particular, appendix E of Ref. (72) presents a very pedagogical derivation of the transmission amplitudes and current using NEGF.

We consider a generic BdG Hamiltonian $\mathcal{H}$ in the real space representation,

$$\mathcal{H} = \frac{1}{2}\sum_{\vec{r}} \psi^{\dagger}_{\vec{r}}\ h(\vec{r})_{BdG}\ \psi_{\vec{r}},$$

where we define the basis spinors $\psi_{\vec{r}} = \frac{1}{\sqrt{2}}\begin{pmatrix} c_{\vec{r},a_1} & c_{\vec{r},a_2} & \dots & c_{\vec{r},a_N} & c^{\dagger}_{\vec{r},a_1} & c^{\dagger}_{\vec{r},a_2} & \dots & c^{\dagger}_{\vec{r},a_N}\end{pmatrix}^T$. The set $\{a_1, \dots, a_N\}$ takes into account the set of degrees of freedom (spin, orbitals, etc.).

We will also consider m leads with self-energies Σ_j and bias V_j, where j=1,...m. The bias defines the lead occupation levels described by the Fermi-Dirac distribution, which we write as a matrix in the Nambu (particle/hole) space,

$$F_j = \begin{pmatrix} f(E, \mu - eV_j) & 0 \\ 0 & f(E, \mu + eV_j) \end{pmatrix}, \tag{3.40}$$

with μ being the chemical potential of the main region and

$$f(E, \mu \pm V_j) = \exp((E - (\mu \pm V_j))/k_B T + 1)^{-1}$$

being the usual Fermi-Dirac distribution.

We can define the current at a lead 'j' in terms of Green's functions (72,73)

$$I_j = i\frac{e}{2}\int \frac{dE}{2\pi}\,\mathrm{Tr}\Big\{(\tau_z \bigotimes I_N)\Gamma_j\left[G^{<} + F_j(G - G^{\dagger})\right]\Big\}, \tag{3.41}$$

where the $\frac{1}{2}$ factor comes from the BdG formulation, and τ_z acts on the Nambu space, such that $(\tau_z \bigotimes I_N)$ takes the electrons and holes opposite charges into account. We also used the lesser Green's function $G^{<} = G(\sum_i \Gamma_i F_i)G^{\dagger}$.

After some algebra, *c.f.* Ref. (72), we can get to the following expression:

$$\begin{aligned} I_j = \frac{e}{2}\sum_i \int \frac{dE}{2\pi} Tr\{&\Gamma^e_j G \Gamma^e_i G^{\dagger}(f^-_j - f^-_i) - \Gamma^h_j G \Gamma^h_i G^{\dagger}(f^+_j - f^+_i) \\ &+ \Gamma^e_j G \Gamma^h_j G^{\dagger}(f^-_j - f^+_j) - \Gamma^h_j G \Gamma^e_j G^{\dagger}(f^+_j - f^-_j) \\ &+ \Gamma^e_j G \Gamma^h_i G^{\dagger}(f^-_j - f^+_i) - \Gamma^h_j G \Gamma^e_i G^{\dagger}(f^+_j - f^-_i)\}. \end{aligned} \tag{3.42}$$

Here we used a compact notation for the distributions f, where the superscript '$-$ $(+)$' indicates whether we are dealing with electron (hole) distribution and the lower index shows the corresponding lead. The $\Gamma^{e(h)}$ matrices are the Γ matrices as we defined previously, but projected into the electron (hole) subspace.

Equation 3.42 may look incomprehensible at first sight but it has a clear physical interpretation. Every term can be divided into two parts: the restriction imposed by the occupations and the probability of a given process happening, i.e. the transmission amplitudes. The first part shows up as the difference of the Fermi-Dirac distributions, e.g. $(f_j^- - f_i^-)$. The later is given by the product of Γ matrices and Green's functions, e.g. $\Gamma_j^e G \Gamma_i^e G^\dagger$.

Now we describe each of the possible processes starting with the injection of an electron at lead 'j'. The first term in the first line in Eq. 3.42 represents the direct tunneling, i.e. injecting an electron into lead 'j' and removing it at lead 'i'[††]. The first term in the second line is the Andreev reflection component of the current, in other words: the contribution originated from injecting an electron at lead 'j' and getting a reflected hole at the same lead, inducing a Cooper pair into the superconducting region. In the last line, the first term represents the cross Andreev reflection, which has a similar interpretation as the usual Andreev reflection, but in this case, the other electron used to compose that Cooper pair will come from another lead 'i' and the hole will be created there. Notice that we talked about just the first term in each line, this is because the second terms represent the same ideas but changing electrons by holes, i.e. start injecting a hole instead of an electron.

[††] note that if i=j, we have $f_j - f_j = 0$ and there is no contribution to the current, as expected.

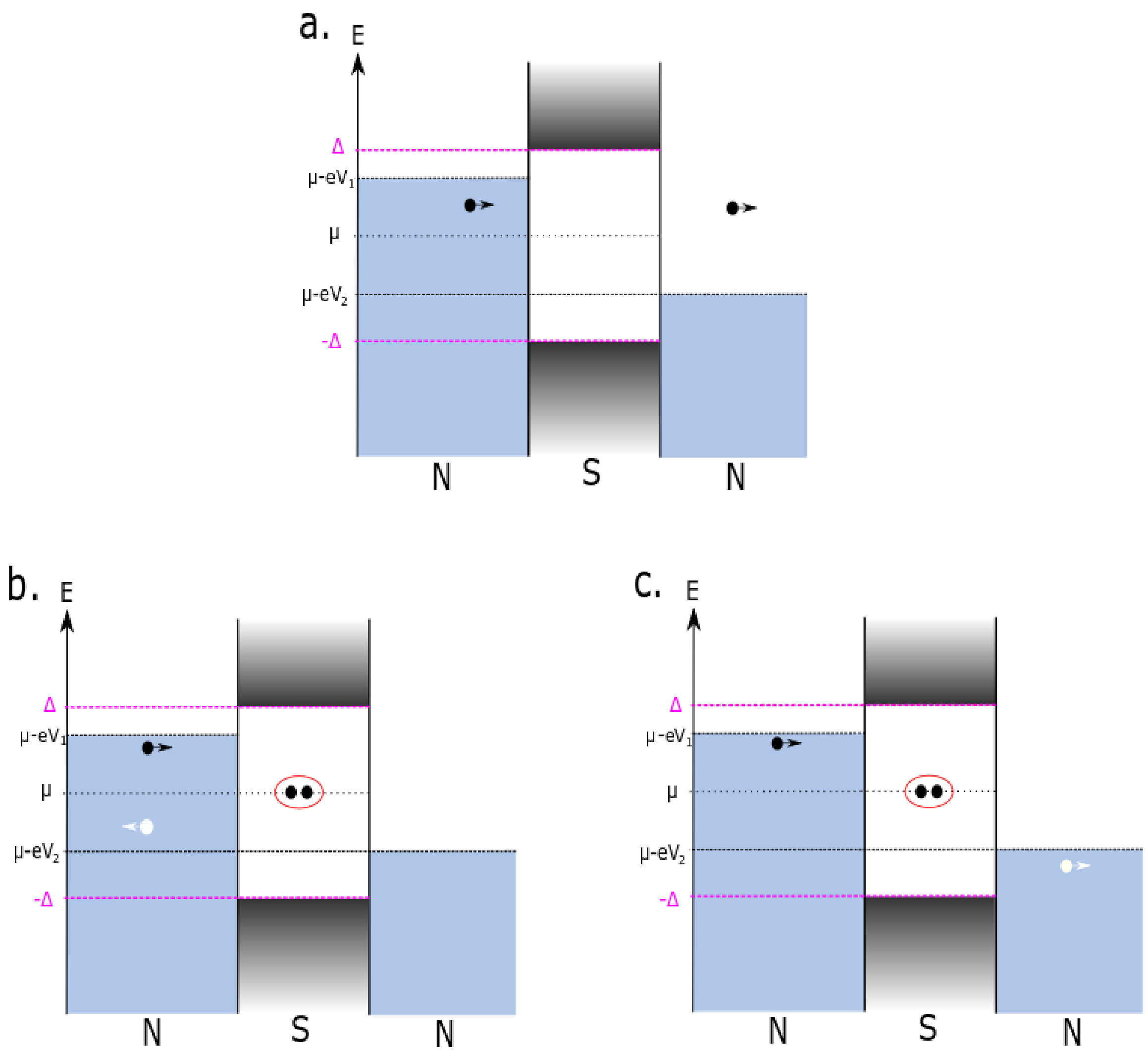

Figure 16 – The three possible processes in an N/S/N junction. All three figures show the occupation levels in the left and right normal regions (N) and the gap Δ in the superconducting region (S). **a.** shows the direct tunneling of an electron through the superconductor. This process is equal to what happens in a usual potential barrier. **b.** is the Andreev reflection, i.e. we create a Cooper pair in the superconductor by using the incident electron and another electron from the left normal region. This other electron will leave a vacancy and create a reflected hole. **c.** is similar to **b.** and shows us the cross Andreev reflection. Now the vacancy creates a hole moving forward in the right normal region. Source: By the author.

4 RESULTS AND DISCUSSION

As mentioned previously in the Introduction, the main result of this work is showing that chiral Majorana edge states can localize and morph into Majorana corner modes.

The novelty of our finding relies on the existence of Majorana corner modes *not* depending on an anisotropic "mass term" (gap), e.g. a d-wave pairing, in our Hamiltonian. As it is well-known (29–38), these terms gap out the edge states and create domain walls at the corners, i.e. the MCS emerge through "the usual way" as mentioned in the Introduction. In contrast, we have a model that, accordingly (Sec. 2.3.2) with the bulk topology and the bulk-edge correspondence, should only host either a single chiral Majorana or a pair of edge states; but, instead, it shows localized corner states for a certain set of the parameters μ and Δ.

To present and discuss this finding, we organize the next pages as follows: first, we will show the existence of the MCS and some of their features; next, we look at the superconducting pairing $e^{i\varphi(\vec{r})}|\langle c_{\vec{r}\uparrow} c_{\vec{r}\downarrow}\rangle|$ and how we can possibly relate its phase $\varphi(\vec{r})$ to the existence of the MCS. Using the knowledge about our model symmetries (calculated in Sec. 3.1), we search for symmetry (or symmetries) that might protect these corner states. Furthermore, we propose an effective phase diagram displaying a region in the parameter space (μ, Δ) corresponding to the MCS phase. We construct this map by looking at the zero-bias conductance peaks of a "corner junction". This map allows us to differentiate the zero-bias peaks of a Majorana bound state from that of a Majorana chiral edge state.

4.1 New phase: corner states

The main result of this work is the existence of Majorana corner states in a QAH/SC, hence we start to discuss our results by showing their existence. To this end, we will look at the DOS and the LDOS through the lens of the NEGF method that we developed in Ch. 3.

As we see in Fig. 17 and 18, depending on the parameters (μ, Δ), we observe chiral Majorana edge states as several DOS peaks for energies inside the gap. Here, instead of seeing the constant DOS expected from a 1D state that is linear in k, we see discrete peaks because we have a confined system.

On the other hand, we see that as we change parameters* (for the case in the Figs. 17 and 18: as we increase the chemical potential), a large DOS peak (~ 100 times larger than the edge state DOS) appears at zero-energy. By looking at the spatial profile with the LDOS, we observe four peaks, each one at a corner.

---

*we will try to consistently answer the question "when do we have MCS?" later on by using the zero-bias conductance to create a phase diagram.

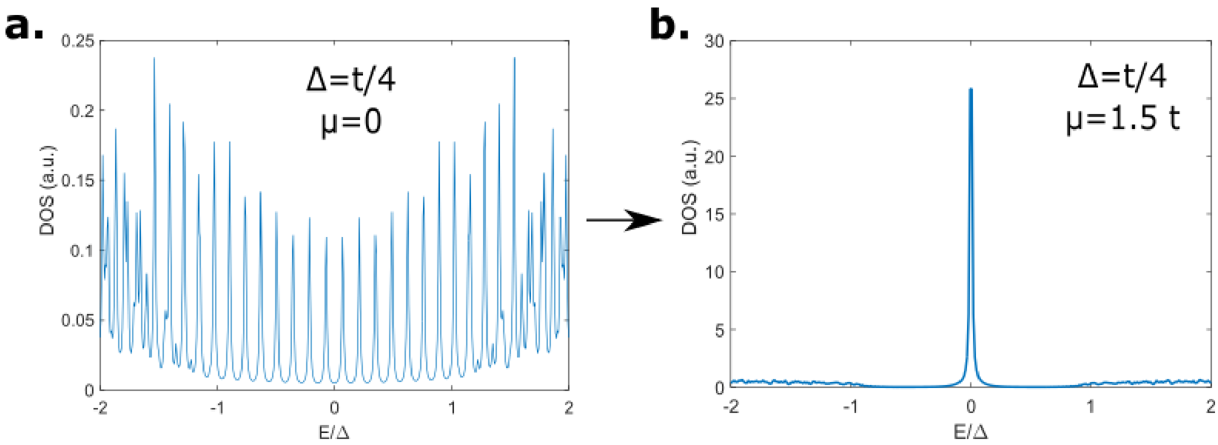

Figure 17 – Density of state for two different set of parameters. **a.** The DOS exhibits a profile with several peaks within the gap (i.e., $E < \Delta$), which correspond to Majorana chiral edge states. **b.** The DOS shows one expressive peak at $E = 0$ with a DOS 10 time bigger than the DOS of the chiral edge states in **a.** This second set of parameters is in a 2^{nd}-order TSC phase that gives us four Majorana corner states. Source: By the author.

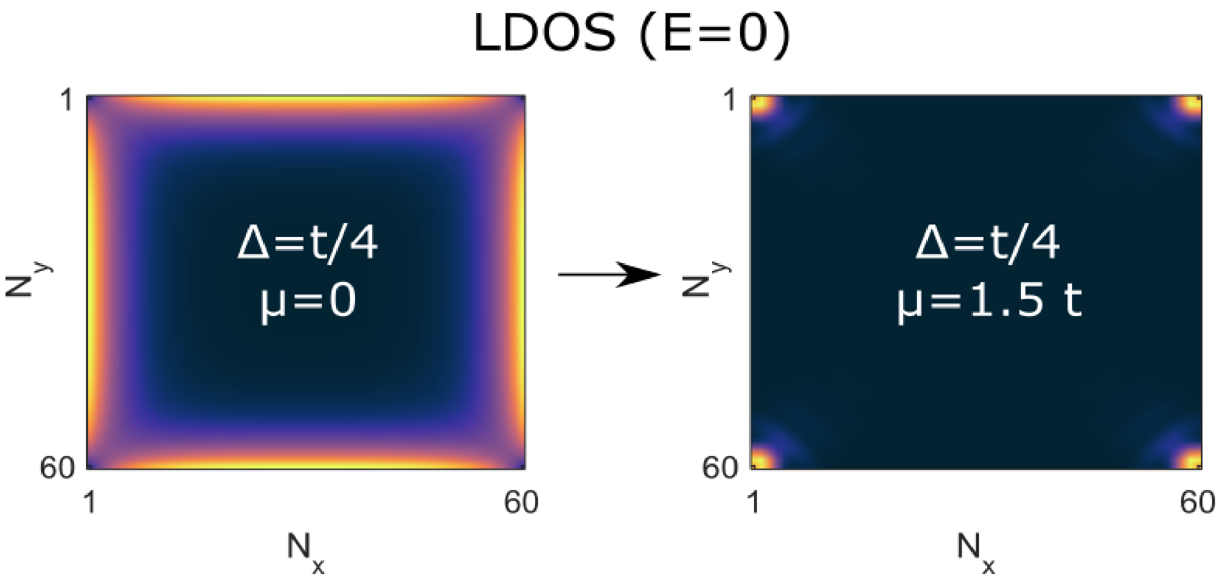

Figure 18 – Local density of states (LDOS) at zero energy showing chiral Majorana edge states (left) morphing into four Majorana corner states (right) as we move in the parameter space (μ, Δ). In this case, only the chemical potential μ vary. Source: By the author.

Alternatively, we can look at the eigenvalues from the exact diagonalization of the Hamiltonian, Fig. 19. This second technique allow us to see that in the chiral Majorana phase the lowest energy states do not go to E=0, Fig.19 **a.**, which is consistent with having a 1/2-spin state along a closed path. The reason for this energy condition is that in a closed path, an 1/2 spin solution has anti-periodic boundary conditions due to the Berry phase, (40). This boundary condition makes the edge state acquire a half integer angular momentum which shifts the lowest energy from 0, *c.f.* (18,74).

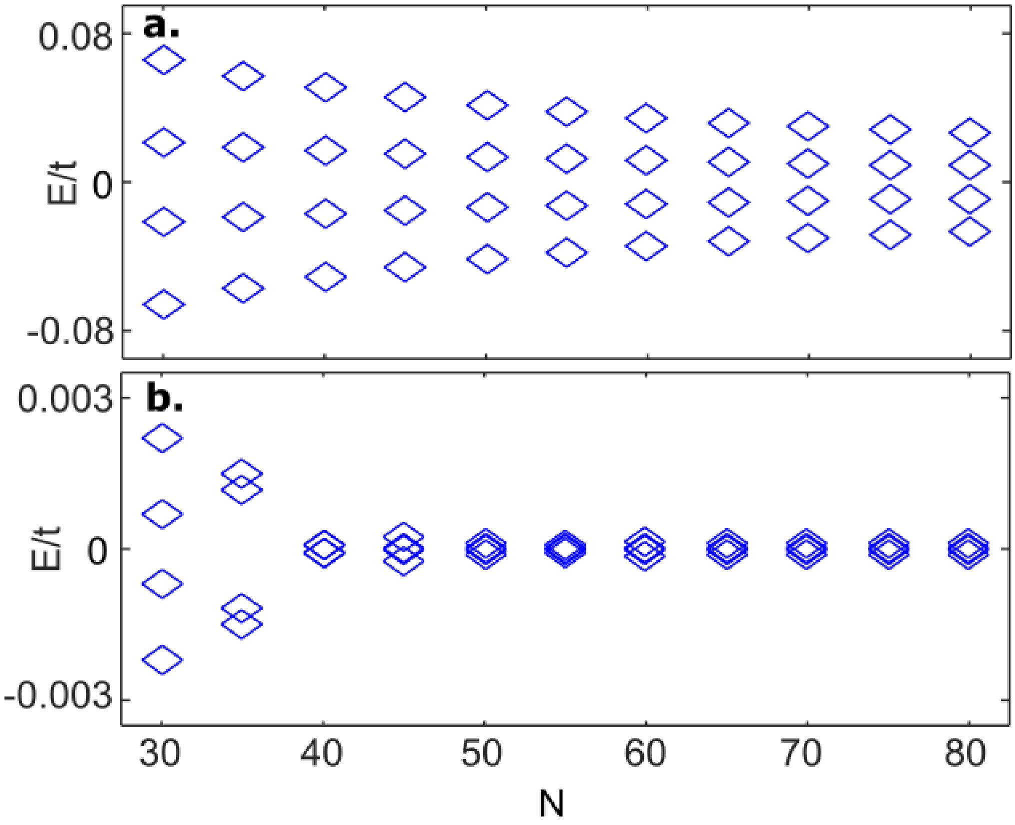

Figure 19 – Dependence of the lowest eigenenergies of our planar QAH-SC setup with the square lattice size N ($N \times N$ sites) for **a.** the chiral phase [($\mu = 0.5t$,$\Delta = 0.7t$)] and **b.** the phase hosting MCSs [($\mu = 1.5t$, $\Delta = t/4$)]. In contrast with the chiral regime, in the phase with corner states **b**, corner-mode hybridizations decrease as N increases and all the energies approach zero. This behavior indicates that these four modes become MCS for large lattice sizes. Note the difference in scale of the vertical axes in **a.** and **b.** Source: By the author.

In contrast, for parameters corresponding to the MCS phase, Fig. 19 **b.**, there are four states that asymptotically become zero-energy modes, i.e., Majorana states, as we increase the lattice size (i.e., as we decrease their hybridization). Here, it is important to observe the difference in energy scales between the lowest energy chiral Majoranas and the MCS, vertical axes in Fig. 19. This comparison allows us to contrast which states tend to zero or not. Note, that the energies of the (hybridized) MCS are at least 10 times smaller than the chiral Majoranas energies.

In addition, we notice that the energies of these states do *not* decrease monotonically, i.e., there are oscillations. This behavior is known to be characteristic of Majorana modes in other platforms, e.g., the Kitaev chain (75,76). As the hybridization comes from the wave-function overlap of Majorana states, this energy spitting is highly dependent on the parameters of the system. For some parameters the wave-functions can be orthogonal and hence there is no hybridization; in contrast, if the wave-functions happen to be parallel, the hybridization is maximized. For our model, we do not have an analytical formula for the hybridization energy but for simpler cases with two MZM, closed formulas were already found. For instance, for two Majoranas bounded to two vortices, separated by a distance R, the splitting energy is (77) $\epsilon_M \propto \cos(R/\xi)\exp(-R\xi)$, where ξ is the coherence length (5). Hence, by having in mind the cases where Majoranas hybridization was studied in detail, the dependence of the hybridization with the size of the lattice N, in Fig. 19 **b.**, that we observe suggests that these states should become Majorana modes for large lattices.

We can also look at the probability density spatial profile as a sanity check since it should be proportional to the LDOS. As expected, the wave-function spatial profile is identical to the one obtained through the LDOS, therefore we do not show it to avoid unnecessary redundancy.

Moreover, we can compare the spin texture of the chiral Majorana edge state with the Majorana corner state. Here, when we say that we are looking at the spin texture, we are in fact looking at the spatial profile of a spin operator that only acts on the particle subspace, similar to what is defined in Ref. (78). For instance, to compute the spin z component S_z at a given site with coordinates $\vec{r} = (i, j)$ for a state $|\theta\rangle$, we would need to look at

$$S_z^{\vec{r}} = \langle\theta|\vec{r}_e\rangle \langle\vec{r}_e| \hat{S}_z |\vec{r}_e\rangle \langle\vec{r}_e|\theta\rangle \,. \tag{4.1}$$

Here $|\vec{r}_e\rangle \langle\vec{r}_e| \hat{S}_z |\vec{r}_e\rangle \langle\vec{r}_e|$ is the z-component spin operator projected into the electron subspace of a given site $\vec{r}$. This operator can be written as

$$|\vec{r}_e\rangle \langle\vec{r}_e| \hat{S}_z |\vec{r}_e\rangle \langle\vec{r}_e| = |\vec{r}_e\rangle \begin{pmatrix} 1 & 0 \\ 0 & -1 \end{pmatrix} \langle\vec{r}_e| \,. \tag{4.2}$$

Note that $\langle\vec{r}_e| S_z |\vec{r}_e\rangle$ is a matrix rather than a number because the spin degree of freedom is still “free”.

Again, we can perform this calculation by using the NEGF method (Eq. 3.39) or by using the eigenstates (Eq. 4.2), obtained from the exact diagonalization, to calculate the expectation value of these spin operators. The difference between these methods is that using the NEGF gives us the spin texture for a given energy and the exact diagonalization, for a given state. To check the equivalency of these approaches, we verified that if we choose an energy close to an eigenenergy, both methods provide the same result.

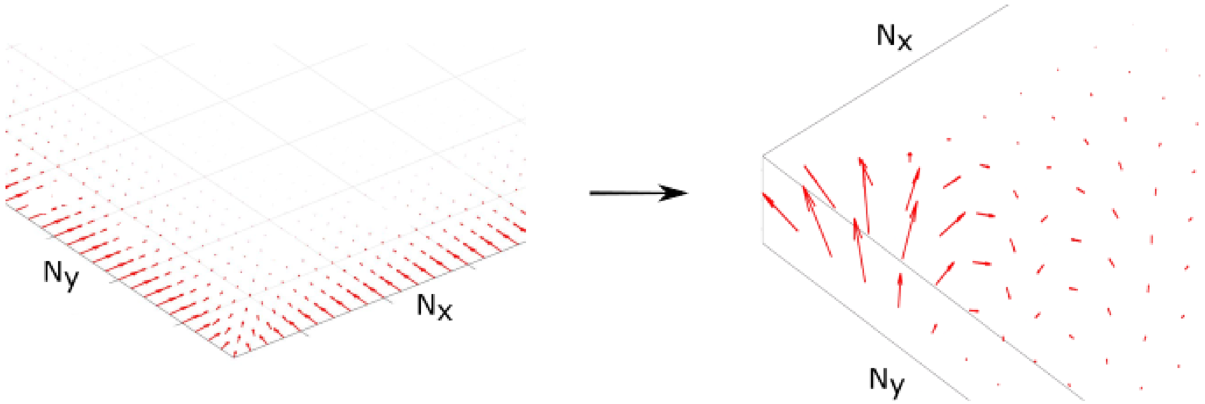

Figure 20 – Spin texture of the chiral Majorana edge states (left side) and spin texture of a Majorana corner state (right side). The arrow at a given position $\vec{r}$ represent the vector $(\langle S_x^{\vec{r}}\rangle, \langle S_y^{\vec{r}}\rangle, \langle S_z^{\vec{r}}\rangle)$. Notice that the MCS has an out-of-plane spin component and a "hedgehog" configuration. The parameters are the same as in Fig. 18. Source: By the author.

We observe that, in contrast with the chiral edge states, the MCSs have an out-of-plane spin component and assume an *asymmetric* "hedgehog" like texture similar to Néel-type skyrmion textures. We call it asymmetric because the part of the system that could make the texture rotationally symmetric does not exist due to the presence of boundaries.

At the current level of understanding about this system, this feature could be used to characterize these MCS through spin-resolved experiments(78), e.g., polarized STM. This possibility should demonstrate that the spin texture is an interesting quantity in this system. We believe that in future works one can show that this unusual spin texture may be associated with some sort of topological invariant. If this idea turns out to be true, it would establish either a bulk-corner or a bulk-edge-corner correspondence for this model or more generally for systems with the same set of symmetries.

In addition to showing the existence of Majorana corner states in our Hamiltonian, we would like to relate their existence with another fundamental change in our system. Usually, for ordinary topological phases, the emergence of edge states is connected to a topological change in the bulk bands. Unfortunately, as mentioned, we do not have access to a topological invariant to show that a global quantity is changing (either on the bulk or edges) as we go from the TSC with chiral edge states to the MCS phase.

Alternatively, here we offer a possible explanation by looking at the pairing function in the presence of edges *and* corners, where can see the formation of "mass domains" at the corners. To this end, we use the relation,

$$\langle c_{\uparrow,\vec{r}}\, c_{\downarrow,\vec{r}}\rangle = \sum_n u_{n,\vec{r},\uparrow}\, v^*_{n,\vec{r},\downarrow} \tanh\frac{E_n}{2k_B T}, \tag{4.3}$$

where k_B is the Boltzmann constant and T the temperature. The remaining coefficients come from the Bogoliubov transformation, which diagonalizes our BdG Hamiltonian,

$$\mathcal{H}_{BdG}\begin{bmatrix} u^*_{n,\vec{r}} \\ v_{n,\vec{r}} \end{bmatrix} = E_n \begin{bmatrix} u^*_{n,\vec{r}} \\ v_{n,\vec{r}} \end{bmatrix}, \tag{4.4}$$

where $E_n \geq 0$, i.e., $(u^*_{n,\vec{r}},\ v_{n,\vec{r}})^T$ are the eigenstates with positive energy. Moreover, we ignore thermal effects by taking the limit $T \to 0$, which implies $\tanh \frac{E_n}{2k_BT} \to 1$ for positive energies, including $E_n \to 0^+$.

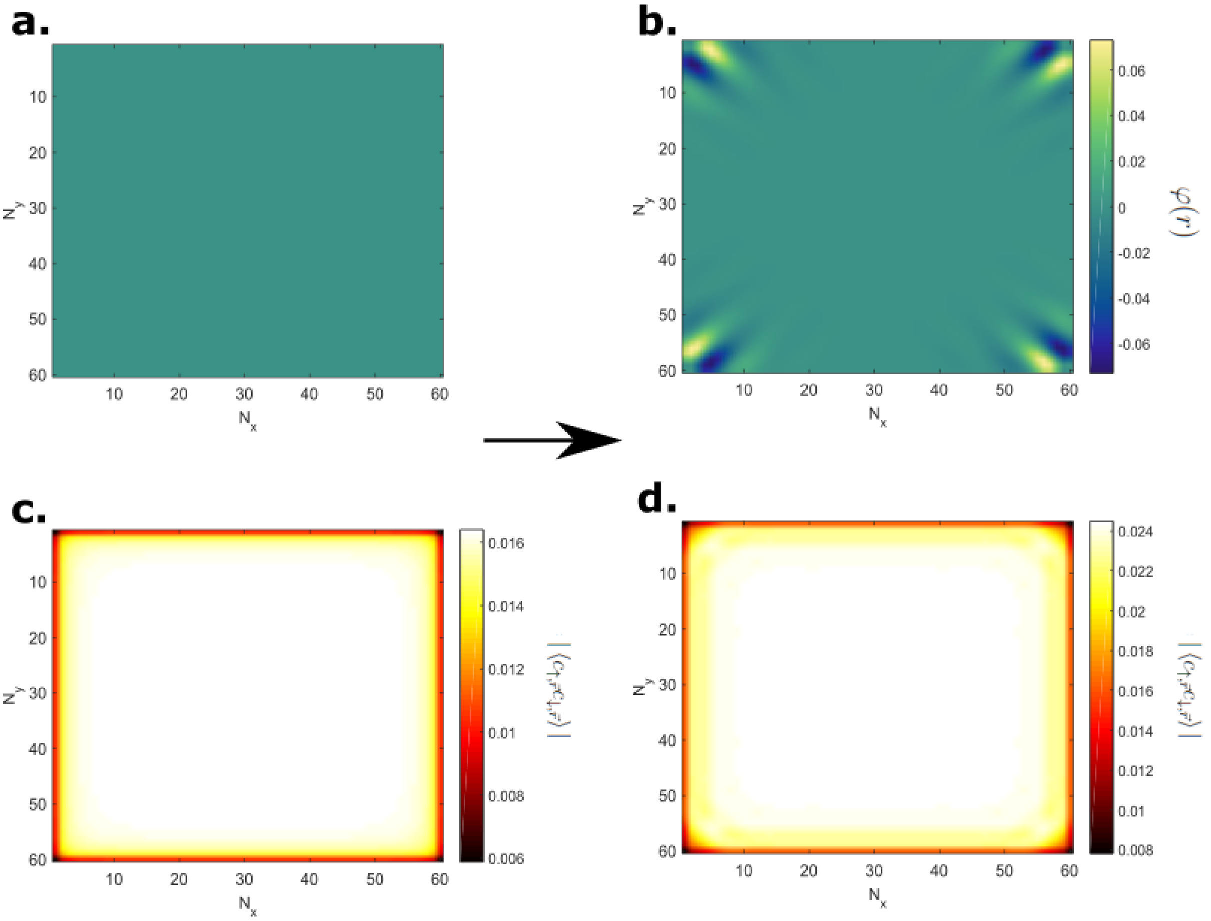

Figure 21 – On site singlet pairing function. The upper panels (**a.** and **b.**) show the complex phase $\varphi(\vec{r})$ and the lower panels (**c.** and **d.**) show the absolute value $|\langle c_{\uparrow,\vec{r}} c_{\downarrow,\vec{r}}\rangle|$. Furthermore, the left panels (**a.** and **c.**) correspond to the TSC ($\mathcal{N} = 1$) phase with chiral Majorana edge states and the right panels (**b.** and **d.**), to the 2^{nd}-order phase with Majorana corner states. The main difference between the TSC ($\mathcal{N} = 1$) and the 2^{nd}-order phase, in terms of the pairing function, is that: in high-order phase, a domain wall structure appears in the phase $\varphi(\vec{r})$ at the corners. Source: By the author.

To have a better grasp at our analysis, we write the pairing function $\langle c_{\uparrow,\vec{r}}\, c_{\downarrow,\vec{r}}\rangle$ as a complex number in polar form, i.e., $|\langle c_{\uparrow,\vec{r}}\, c_{\downarrow,\vec{r}}\rangle| e^{i\varphi(\vec{r})}$, where $\varphi(\vec{r}) \in [-\pi, \pi)$ is the phase (polar angle in the complex plane).

What we can see from the example in Figure 21 is that, for parameters corresponding to the MCS phase, the phase $\varphi(\vec{r})$ assumes values that correspond to the pairing function $|\langle c_{\uparrow,\vec{r}}c_{\downarrow,\vec{r}}\rangle|e^{i\varphi(\vec{r})}$ becoming complex. In addition, this mutation happens in a particular way: the phase $\varphi(\vec{r})$ changes sign around the corners and it is zero far from the corners. If we want to push our intuition further, we can think about corner states as being boundary (corner) states from ordinary boundary (edge) states, i.e., we can picture the corner modes as edge states of edge states, thus the name "second order".

We can think about this structure in the pairing as a (phase) domain wall, similar to what we saw in Chapter 2 when discussing edge states in different setups. However, here, interestingly, the difference of $\varphi(\vec{r})$ on opposite sides of the corner picks up small values, $\sim 0.04\pi$, meaning that only the imaginary part of the pairing function changes sign. In contrast, the phase difference in the examples discussed in Sec. 2.2.1 is π. Furthermore, we conjecture that this phase change is a boundary effect, meaning that the presence of edges *and* corners is implying in this particular arranging of the pairing function. To corroborate this point of view more work is needed, i.e., a self-consistent calculation taking into account the superconducting layer as part of the Hamiltonian and not only the induced pairing.

Note that this effect is completely different from the usual proposals for HOTSC phases (29–38). Here, we cannot do the common analytical formulation of projecting the Hamiltonian into edge state subspaces (for different edges) and show that there is a mass gap with opposite signs along adjacent edges. We cannot do this because we start with a single chiral edge state "per physical edge of the system", i.e. the projected Hamiltonian would be 1×1 and we would not see any mass term that would gap out the chiral edge mode. Furthermore, even if we look at a strip geometry where we have edge states forming a Dirac 1D cone, where we could possibly see a gap appearing in edge states (for parameters corresponding to the HOTSC phase), we do not see this gap. This means that our corner states cannot be explained by effects that happen "separately" at each edge, i.e., we do not see any unusual or unexpected behavior in a geometry that does not have physical corners (e.g., an infinite strip).

4.2 Symmetry protection

Let us now discuss the Majorana corner states in terms of the symmetries of our Hamiltonian. More precisely, let us see which symmetry, if any, protects the existence of these states against perturbations, e.g. disorder.

Here, the concept of protection refers to a conditional relationship between the existence of the corner modes (with some degree of robustness†) and the presence of a given symmetry. Notice that this relation would be similar to an "if" condition rather an "if and only if" condition.

---

† we say "some degree" because some reasonable conditions need to be assumed, e.g., the perturbation should not be strong enough to close the gap.

The symmetries present in our model, as we shown in Sec. 3.1 are: the 90° (and 180°) rotational symmetries C_4 (and C_2, i.e., inversion) and the magnetic mirror symmetries $\mathcal{M}_x\mathcal{T}$, $\mathcal{M}_y\mathcal{T}$, $\mathcal{M}_{x+y}\mathcal{T}$ and $\mathcal{M}_{x-y}\mathcal{T}$. As mentioned, we want to see which one (if any) of these symmetries protects the MCS. To this end, we will modify our Hamiltonian model to break one of the symmetries and see what happens to the corner states. If we break a given symmetry and the MCS are *not* removed, then we can say that this particular symmetry does *not* protect the corner modes. On the other hand, if we break one of these symmetries and the Majorana corner modes disappear, we can say that this symmetry was protecting these states.

The first symmetry that we will explore is the C_4 rotation. The way that we found to break it is by transforming the square lattice into a rectangular lattice, i.e., changing the lattice spacing of either the x or y direction. Note that the inversion symmetry (180° rotation) C_2 is not broken by this transformation, Fig. 22 **a.**, so we will need another way to test it.

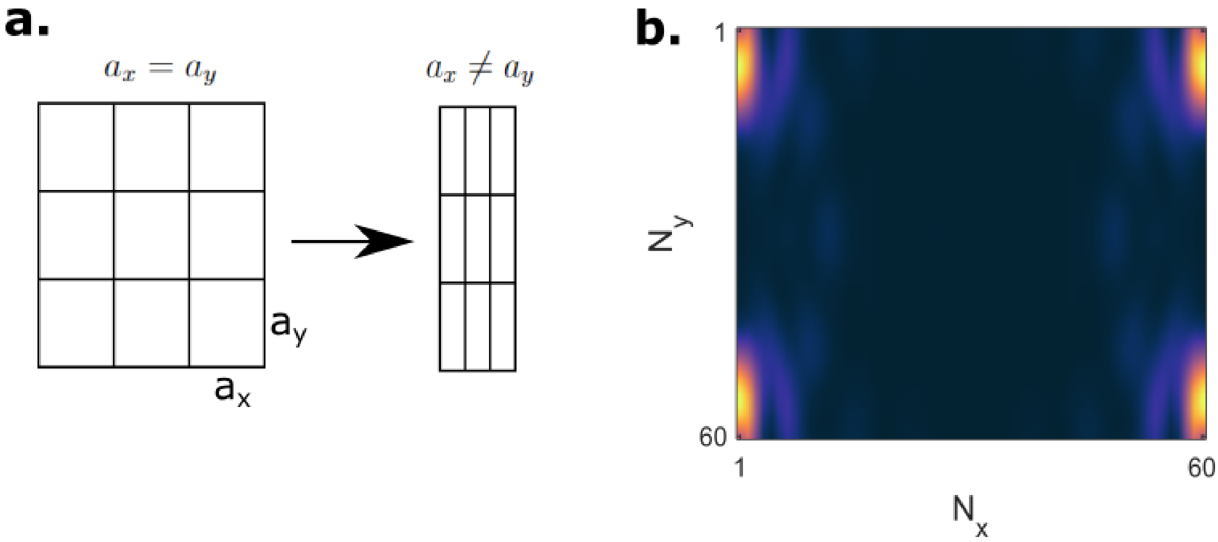

Figure 22 – **a.** transformation from a square lattice into a rectangular lattice to reduce the rotational C_4 symmetry into C_2. **b.** Lowest energy state wave-function for $a_x = a_y/3$. We see that even though the C_4 symmetry is removed, the four corner states still exist; therefore, these states are not protected by this symmetry. Source: By the author.

Figure 22 shows that the braking of C_4 does not affect the corner states. The only effect is a deformation of their spatial profile, as seen via their probability density $|\psi|^2$ in the right panel Fig. 22**b.** Hence, we can say that the MCS of our system are *not* protected by the C_4 symmetry.

Next, we look at the magnetic mirror symmetries. The "trick" that we will perform to study these symmetries is to apply an in-plane Zeeman field $m_\theta = |m_\theta|(\cos\theta\ \sigma_x + \sin\theta\ \sigma_y)$, where θ is the polar angle. We can see here that when $\theta = n\frac{\pi}{4}$ with $n \in \mathbb{N}$, all of the $\mathcal{M}\mathcal{T}$ symmetries will be broken except one, e.g., if $\theta = 0$, $m_0 = |m_0|\sigma_x$ and only $\mathcal{M}_x\mathcal{T}$ is preserved. To see this fact, we can imagine that the sign of the Zeeman field in the x direction will be "flipped" once by the $\mathcal{M}_x$ transformation and once more with $\mathcal{T}$, hence remaining invariant after the transformation $\mathcal{M}_x\mathcal{T}$.

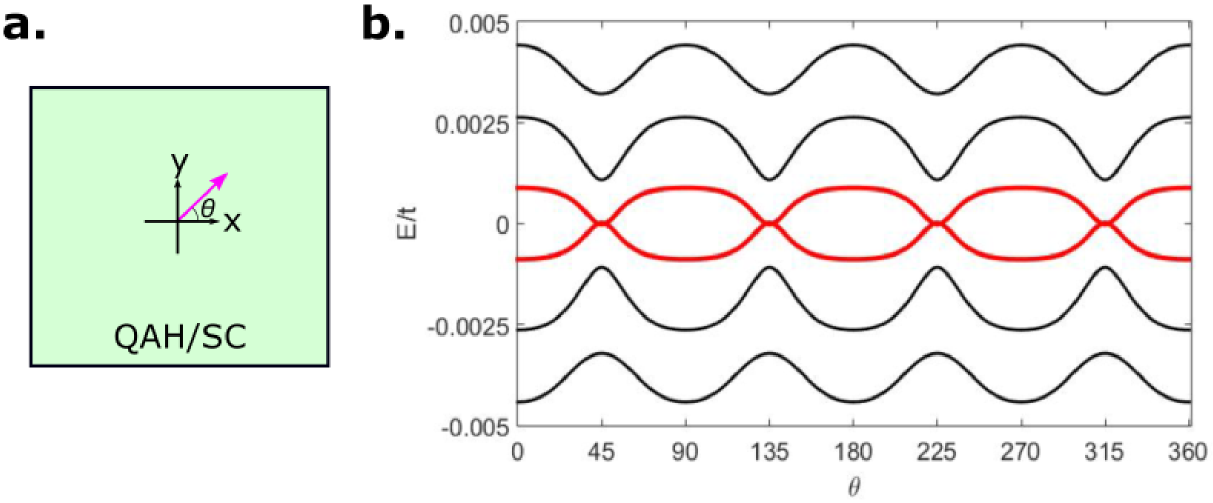

Figure 23 – **a.** schematic to show the Zeeman field direction as a function of the polar angle θ. **b.** six lowest enegy states as a function of the Zeeman field angle. We can see that for odd multiples of 45°, we have two zero-energy states, corresponding to the scenarios where either $\mathcal{M}_{x+y}\mathcal{T}$ or $\mathcal{M}_{x-y}\mathcal{T}$ is preserved. At the remaining angles, both symmetries are broken and all the Majorana corner states are removed. The parameters for the plot are $\mu = 1.4t$ $m_\theta = 0.4t$ $\Delta = t/4$ and the lattice has 90×90 sites. Source: By the author.

What we see when we look at the lowest energy states as a function of the Zeeman angle θ in Fig. 23 is that for odd multiples of 45°, $\theta = (2n+1)\frac{\pi}{4}$, we have two zero-energy states. On the other hand, for the remaining angles, we do not see zero-energy states.

By using that we can associate the angle of the Zeeman field with the preservation of one of the magnetic mirror symmetries for some angles, we see that when $\theta = (2n)\frac{\pi}{4}$ both $\mathcal{M}_{x+y}\mathcal{T}$ and $\mathcal{M}_{x-y}\mathcal{T}$ are broken but either $\mathcal{M}_x\mathcal{T}$ or $\mathcal{M}_y\mathcal{T}$ is preserved, however the zero modes are always gaped. Hence, by the syllogism that we proposed only $\mathcal{M}_{x+y}\mathcal{T}$ and $\mathcal{M}_{x-y}\mathcal{T}$ protect the MCS and the remaining magnetic reflection operations $\mathcal{M}_x\mathcal{T}$ or $\mathcal{M}_y\mathcal{T}$ do *not* have a role concerning the MCS.

Note that $\mathcal{M}_{x+y}\mathcal{T}$ and $\mathcal{M}_{x-y}\mathcal{T}$ protect the two of the corner states each. We can understand this by noticing that at the odd multiples of 45° only one of the symmetries is preserved and we also only keep one pair of zero-energy states, e.g., at 45°, just $\mathcal{M}_{x+y}\mathcal{T}$

is preserved. Moreover, by looking at the wave-function of the zero-energy states, we see that these zero-energy modes correspond to a pair of Majorana corner states and which pair is preserved depends in the direction of the Zeeman field, as we see in Fig. 24.

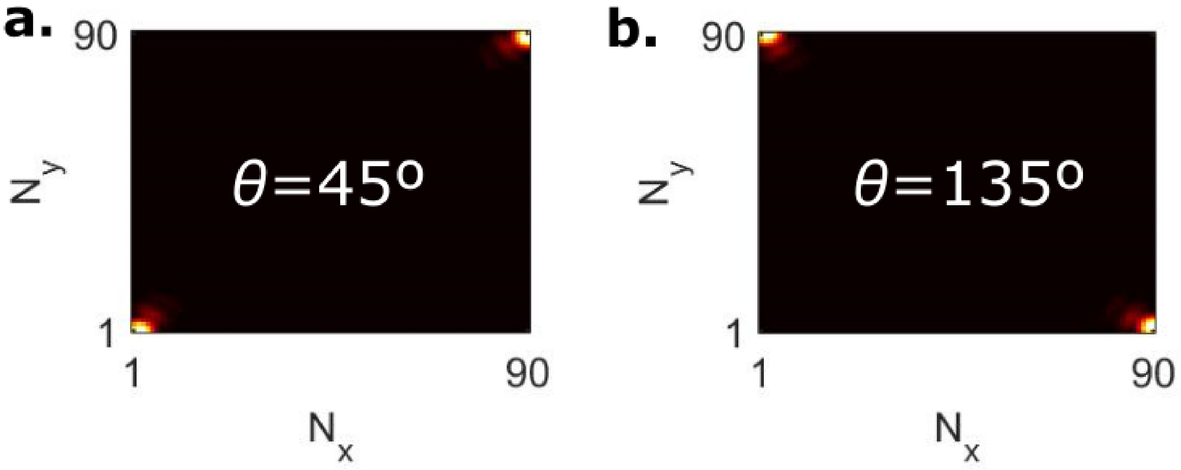

Figure 24 – **a.** wave-function of the zero energy states for the Zeeman field angle $\theta = 45°$ **b.** wave-function of the zero energy states for the Zeeman field angle $\theta = 135°$. For $\theta = 45°$ the $\mathcal{M}_{x+y}\mathcal{T}$ symmetry is preserved but not $\mathcal{M}_{x-y}\mathcal{T}$, hence only two of the corner states remain gapless. On the other hand (**b.**), for $\theta = 135°$ only $\mathcal{M}_{x-y}\mathcal{T}$ is preserved and the states switch corners. Source: By the author.

Fortunately, the remaining C_2 symmetry can be also studied with the in-plane Zeeman field. In this case, the field always breaks C_2, independently of the angle θ. Therefore, if C_2 were the symmetry offering protection to the corner states, the direction of the Zeeman field would not be relevant as C_2 would never be present. As we saw in Fig. 23**b.** the zero-energy corner modes are sensitive to θ, hence they cannot be protected by C_2.

In addition to helping us to understand the roles of the Hamiltonian's symmetries, we can imagine that it is possible to engineer devices that make use of this angular dependence with the in-plane Zeeman field. We do not need to think too hard to see that one could possibly envisage ways to braid Majoranas or create switching devices (e.g., transistors) for quantum transport by exploiting the angle dependence of an in-plane Zeeman field as discussed above.

Comments on the four-fold degeneracy of the ground state: Non-local fermions

An interesting observation is that in the limit where the corner states become indeed Majorana states (with E=0), the ground-state becomes 4-fold degenerate. Due to the fact that Majorana states do not form a Fock space, i.e. they do not define a number operator, a useful form to put this degeneracy is to combine the Majorana operators to form ordinary (non-local) fermionic operators with zero energy. As they do not cost any energy, both the occupied and unoccupied fermionic states can be added to the ground state. Here, similar to Ref. (10), we can define the operators $d_a = \gamma_{1,1} + i\gamma_{N,N}$ and $d_b = \gamma_{1,N} + i\gamma_{N,1}$ that combine the Majorana operators at a given diagonal of square geometry. Note that $\{d_i, d_j\} = 0$ and $\{d_i^\dagger, d_j\} = \delta_{ij}$. The reason to combine Majoranas in a given diagonal is that they are protected by the same symmetry (either $\mathcal{M}_{x+y}\mathcal{T}$ or $\mathcal{M}_{x-y}\mathcal{T}$), i.e., we could remove two Majoranas and still keep the definition for the operator d of the remaining states. Moreover, this choice is univocal because each MCS is only at one diagonal. In contrast, choosing to use adjacent MCS to form the fermionic operator would lead to an arbitrariness [‡], i.e., one could combine the Majorana at $(1,1)$ in a counterclockwise ($d_a = \gamma_{1,1} + i\gamma_{1,N}$ and $d_b = \gamma_{N,N} + i\gamma_{N,1}$) or clockwise ($d_a = \gamma_{1,1} + i\gamma_{1,N}$ and $d_b = \gamma_{N,N} + i\gamma_{N,1}$) form.

Now, with these non-local fermionic operators defined, we can see that our 4-fold degeneracy can be written as

$$\begin{aligned} &|0,0\rangle\,, \\ d_a^\dagger d_b^\dagger\,|0,0\rangle &= |1,1\rangle\,, \\ d_a^\dagger\,|0,0\rangle &= |1,0\rangle\,, \\ d_b^\dagger\,|0,0\rangle &= |0,1\rangle\,. \end{aligned} \tag{4.5}$$

Note that, in models such as the Kitaev chain where only 2 MZMs emerge in the topological phase there is a 2-fold degeneracy that makes the parity of the ground state indefinite. Here, we also have and indefinite parity because $|0,0\rangle$ and $|1,1\rangle$ have an even occupation number, and $|0,1\rangle$ and $|1,0\rangle$ are odd. However, in our system, each parity subspace (even and odd) have a two-fold degeneracy as there are two even states and two odd states.

In models with 2 Majorana states, their hybridization lifts the parity degeneracy, i.e., the effective Hamiltonian that describes their hybridization is proportional to the parity operator (5), $P = \sum\limits_{i=a,b} (d_i^\dagger d_i - 1/2)$. Here, if we imagine that the effective Hamiltonian to describe the hybridization between our corner states is proportional to the parity, our states should be separated only in two energies. This follows from the fact that each parity subspace is itself double degenerate. However, as we see in Fig. 19 **b.**, the MCS can be hybridized in four states with four different energies, which is a hint that there should be terms that break this additional degeneracy. In this dissertation, we will not explore this effective Hamiltonian but a possibility is that terms proportional to $d_a^\dagger d_b + h.c.$ lifts this degeneracy in each parity subspace.

[‡] in addition pair Majoranas that can be individually removed

4.3 Transport signatures

Now we will apply the NEGF method, developed in Sec. 3.2, to look for a transport signature of the MCS. The purpose behind this calculation is to find a way to tell whether a given pair of parameters (μ, Δ) corresponds to the 2^{nd}-order TSC or to the ordinary TSC with chiral Majorana edge states. As the corner states are zero-energy modes, it is rather intuitive to look for this signature as a zero-bias conductance peak. Moreover, as they are Majorana bound states, we can expect a behavior similar to Majorana bound states in other systems, e.g., the e^2/h peak in a Kitaev chain(72), in contrast to the $e^2/2h$ conductance from the chiral Majorana (39).

To perform this calculation, we consider a corner junction where each corner has one normal lead attached. In terms of the NEGF this means that we will have four self-energies $\Sigma_{1,2,3,4}$ with non-zero elements $\Gamma/2$ only in the matrix elements in subspaces that correspond to the corner sites $(1,1)$, $(1,L_y)$, $(L_x,1)$ and (L_x,L_y), Fig. 25. In addition, we will take one lead as the source and the remaining three as drains, with $V/2$ and $-V/2$ potentials, respectively. Within this choice, the terms corresponding to the cross Andreev reflection cancel out (72) because the "correct" electron state that would form a Cooper pair with the incident electron and leave a vacancy (i.e. create a hole with the same energy from the incident electron) in the drain is not present (see the calculation further below). Moreover, this choice of potential drop allows us to see our setup as a two terminal device as far as conductance measurements go.

To prove the assertion above, let us define $\Sigma_S = \Sigma_1$ and $\Sigma_D = \Sigma_2 + \Sigma_3 + \Sigma_4$ (and equivalently for the broadening matrices Γ), and look at the current expression derived in Sec. 3.2.4 at the source lead S,

$$\begin{aligned} I_S = \frac{e}{2} \sum_{i=2,3,4} \int \frac{dE}{2\pi} Tr\{ & \Gamma^e_S G \Gamma^e_i G^\dagger (f^-_S - f^-_i) - \Gamma^h_S G \Gamma^h_i G^\dagger (f^+_j - f^+_i) \\ & + \Gamma^e_S G \Gamma^h_S G^\dagger (f^-_S - f^+_j) - \Gamma^h_S G \Gamma^e_S G^\dagger (f^+_S - f^-_S) \\ & + \Gamma^e_S G \Gamma^h_i G^\dagger (f^-_S - f^+_i) - \Gamma^h_S G \Gamma^e_i G^\dagger (f^+_S - f^-_i)\}. \end{aligned} \tag{4.6}$$

We recall that, in the right side of this equation, the first line correspond to direct tunneling processes; the second line, the local Andreev reflection and the last line is the cross Andreev reflection, see Fig. 16. Furthermore, by identifying $f_2 = f_3 = f_4 \equiv f_D$ because the drain leads have the same bias applied and that $f^+_D = f^-_S$ and $f^-_D = f^+_S$, the current expression is simplified to

$$\begin{aligned} I_S = \frac{e}{2} \sum_{i=2,3,4} \int \frac{dE}{2\pi} Tr\{ & \Gamma^e_S G \Gamma^e_i G^\dagger (f^-_S - f^-_D) - \Gamma^h_S G \Gamma^h_i G^\dagger (f^+_S - f^+_D) \\ & + \Gamma^e_S G \Gamma^h_S G^\dagger (f^-_S - f^+_S) - \Gamma^h_S G \Gamma^e_S G^\dagger (f^+_S - f^-_S)\}, \end{aligned} \tag{4.7}$$

where our last identification canceled out the cross Andreev terms. In addition, we use that the trace of a product of matrices is preserved under cyclic permutations, i.e., $Tr\{\Gamma^e_S G \Gamma^e_i G^\dagger\} = Tr\{G^\dagger \Gamma^e_S G \Gamma^e_i\}$ and that the sum of two traces is the trace of their sum, i.e.

$$\begin{aligned}
&Tr\{G^\dagger\Gamma^e_S G\Gamma^e_2\} + Tr\{G^\dagger\Gamma^e_S G\Gamma^e_3\} + Tr\{G^\dagger\Gamma^e_S G\Gamma^e_4\} \\
&= Tr\{G^\dagger\Gamma^e_S G\,(\Gamma^e_2 + \Gamma^e_3 + \Gamma^e_4)\} \\
&= Tr\{G^\dagger\Gamma^e_S G\Gamma^e_D\} \\
&= Tr\{\Gamma^e_S G\Gamma^e_D G^\dagger\}.
\end{aligned} \tag{4.8}$$

Hence, we can rewrite our current at the source as coming from considering a single drain lead (which is connected to three different sites),

$$\begin{aligned}
I_S = \frac{e}{2}\int \frac{dE}{2\pi} Tr\{&\Gamma^e_S G\Gamma^e_D G^\dagger(f^-_S - f^-_D) - \Gamma^h_S G\Gamma^h_D G^\dagger(f^+_S - f^+_D) \\
&+ \Gamma^e_S G\Gamma^h_S G^\dagger(f^-_S - f^+_S) - \Gamma^h_S G\Gamma^e_S G^\dagger(f^+_S - f^-_S)\}.
\end{aligned} \tag{4.9}$$

It is important for us to know that we effectively have a two terminal setup because this allows us to use the results from Ref. (39). In that work, the authors showed that (through s-matrix calculations), for the ordinary TSC ($\mathcal{N} = 1$) phase, the chiral Majoranas should produce a conductance of $\mathcal{G} = e^2/2h$.

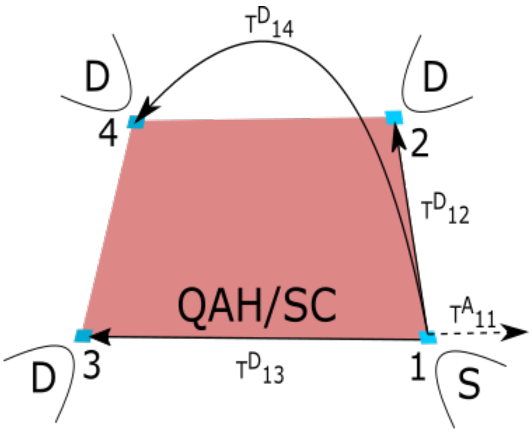

Figure 25 – Schematic of the system used in the transport calculation: a source (S) lead (1) and three drains (D), the at the zero-bias conductance is calculated between S and D. The possible transport processes are: direct tunneling between the source lead and each of the drains, indicated by solid arrows and local Andreev reflection at the source lead, indicated by the dashed arrow. A symmetric potential drop is used between the source and the drains so that cross Andreev reflection processes cancel out. Source: By the author.

Here, we will calculate that conductance and the conductance for the MCS phase by using the linear response approximation in our current formula (Eq. 4.9). To this end we recall that $f^-_S = \exp((E - \mu - eV/2)/k_B T + 1)^{-1}$. For $V \sim 0$ (linear response approximation) and zero temperature, $f_S^- - f_D^-$ and $f_S^- - f_D^+$ both can be approximated to $eV\delta(E = 0)$, where $\delta(E = 0)$ is the Dirac delta at the Fermi level. By using this approximation and the definition of zero-bias conductance $\mathcal{G} = \lim_{V\to 0} dI/dV$, we obtain

$$\mathcal{G} = \frac{e^2}{h}\left(Tr\{\Gamma_S^e G\Gamma_D^e G^\dagger\} + Tr\{\Gamma_S^e G\Gamma_S^h G^\dagger\}\right)\Big|_{E=0}. \tag{4.10}$$

Note that, as mentioned in Sec. 3.2, we can identify these terms as direct tunneling and Andreev reflection probabilities, respectively, due to the Landauer formula (79). Note that in our analysis the spin degree of freedom is summed under the trace operation and therefore we do not distinguish the spins involved in each process.

Now that we have presented our transport setup, we will look at the zero-bias conductance in the parameter space (μ, Δ). As we see in Fig. 26, we have a region where the zero-bias peak is greater than $e^2/2h$ and therefore this region cannot correspond to the ordinary TSC ($\mathcal{N} = 1$) regime with chiral Majorana edge states (which are expected to exhibit $e^2/2h$ conductance as shown at Ref. (39)). As the conductance in this region goes up to e^2/h, which can be seen as a signature of Majorana bound states, we identify this region as the 2^{nd}-order TSC phase with the MCS. Note that the zero-bias peak can also take values in the range $[e^2/2h, e^2/h]$, corresponding to Majorana corner states that are hybridized due to spatial proximity.

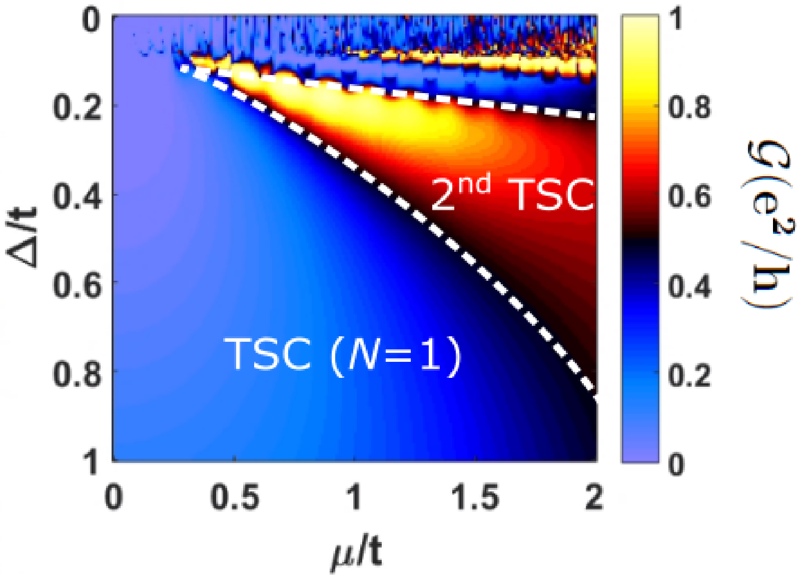

Figure 26 – Color map of zero-bias conductance peak as a function of μ and Δ for a finite square lattice. The blue region corresponds to the ordinary TSC ($\mathcal{N} = 1$), which hosts chiral Majorana edge states. The 2^{nd}-order TSC region shows where we find Majorana corner states through its transport signature $\mathcal{G} = e^2/h$. The red part of the 2^{nd}-order phase show where we have hybridized corner modes due to spatial proximity. Source: By the author.

Unsurprisingly, most of the contribution ($\sim 90\%$) for the zero-bias peak comes as local Andreev reflection at the source lead, similarly to other Majorana bound states, *c.f.* Ref. (72). The remaining of the peak comes from direct tunneling to leads respecting the chirality of the edge states, e.g., if the chiral edge state were running clockwise, we would only see a current flow to leads 3 and 4 in Fig. 25.

On the other hand, we have a region that we identify as the known TSC ($\mathcal{N} = 1$). Here the conductance can assume values between 0 and $e^2/2h$. In this case, this range of values is explained by taking into account that our system is finite in both directions. Therefore we have resonant peaks instead of a plateau. These peaks can be closer to E=0 depending on the parameters but never exactly at E=0, as we discussed previously (see the discussion about Fig. 17).

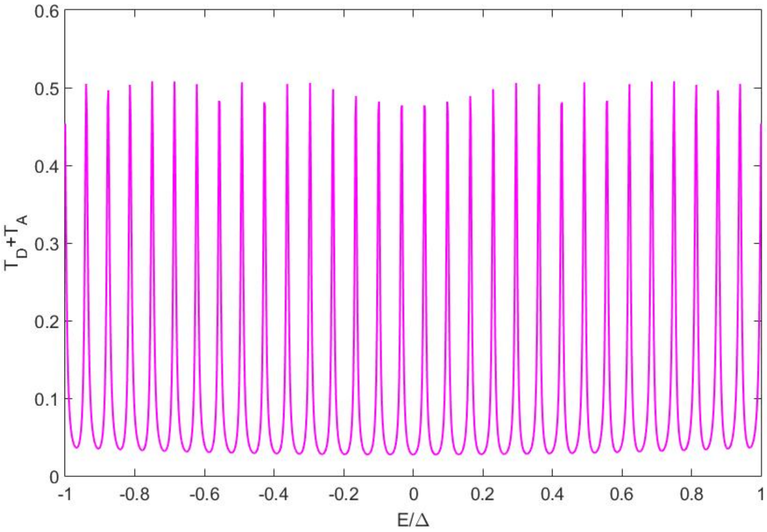

Figure 27 – Total transmission (Andreev reflection + direct tunneling) for a two terminal measurement within the chiral Majorana regime. As the system is finite in every direction, we see resonant peaks going to 0.5 rather than a constant plateau. Notice that there is no peak at E=0. Source: By the author.

5 CONCLUSION

We showed that a planar QAH-SC junction in the ordinary (first order) chiral Majorana phase (1), can exhibit a 2^{nd}-order topological superconductor phase, which was unexpected by the bulk analysis (Chern number) done by Qi *et al.* (1). Our results show a new path to high-order topological superconductivity that does not rely on considering anisotropic mass gaps to simultaneously gap out the edge states and form domain walls to "trap" Majorana corner states.

This new phase that we found exhibits four Majorana corner states, one at each corner, which were characterized via the LDOS, obtained numerically through the NEGF, and the spatial profile of the wave-function, through exact diagonalization. Furthermore, we investigated the pairing function through a simple calculation that did not consider the superconducting layer and a self-consistent order parameter calculation. We find that the phase of the pairing function changes sign across the corners, forming domain wall like structures. We tentatively correlate the emergence of this anisotropy in the pairing function in the presence of boundaries (edges *and* corners) to the existence of the 2^{nd}-order phase.

We performed an exhaustive symmetry analysis considering the spatial symmetries of a square lattice and the non-spatial symmetries of our Hamiltonian model. We concluded that the Majorana corner states in our system are protected by the pair of magnetic reflection symmetries $\mathcal{M}_{x+y}\mathcal{T}$ and $\mathcal{M}_{x-y}\mathcal{T}$. Each of these symmetries protects a pair of Majoranas. Furthermore, we can gap out two of the four corner states in a controllable way by turning on and manipulating the direction of an in-plane Zeeman field. Hence, it is conceivable (for future works) to think about realizing braiding operations using these corner states or engineering quantum transport devices.

Moreover, in the absence of a topological invariant to characterize this higher-order phase, we used the NEGF formalism in the linear response regime to determine an effective phase diagram through the zero-bias conductance peak in a "corner geometry". We find a characteristic zero-bias conductance peak of e^2/h for the Majorana corner states for a wide region in the parameter space (μ, Δ). This transport signature distinguishes the MCS from the chiral Majorana edge states predicted by Qi *et al.* (1) in the ordinary $\mathcal{N} = 1$ phase, as these edge modes are expected to produce a $e^2/2h$ conductance (39). Note that the 2^{nd}-order TSC phase lives within the chiral ($\mathcal{N} = 1$) phase. Thus our results extend the phase diagram of Ref. (1).

REFERENCES

1 QI, X.-L.; HUGHES, T. L.; ZHANG, S.-C. Chiral topological superconductor from the quantum hall state. **Physical Review B**, APS, v. 82, n. 18, p. 184516, 2010.

2 MAJORANA, E. Teoria simmetrica dell'elettrone e del positrone. **Il Nuovo Cimento (1924-1942)**, Springer, v. 14, n. 4, p. 171–184, 1937.

3 BILENKY, S. M. Neutrinos: Majorana or dirac? **Universe**, Multidisciplinary Digital Publishing Institute, v. 6, n. 9, p. 134, 2020.

4 BALANTEKIN, A. B.; GOUVÊA, A. D.; KAYSER, B. Addressing the majorana vs. dirac question with neutrino decays. **Physics Letters B**, Elsevier, v. 789, p. 488–495, 2019.

5 KITAEV, A. Y. Unpaired majorana fermions in quantum wires. **Physics-Uspekhi**, IOP Publishing, v. 44, n. 10S, p. 131, 2001.

6 READ, N.; GREEN, D. Paired states of fermions in two dimensions with breaking of parity and time-reversal symmetries and the fractional quantum hall effect. **Physical Review B**, APS, v. 61, n. 15, p. 10267, 2000.

7 IVANOV, D. A. Non-abelian statistics of half-quantum vortices in p-wave superconductors. **Physical Review Letters**, APS, v. 86, n. 2, p. 268, 2001.

8 KAUFFMAN, L. H. Majorana fermions and representations of the braid group. **International Journal of Modern Physics A**, World Scientific, v. 33, n. 23, p. 1830023, 2018.

9 NAYAK, C. *et al.* Non-abelian anyons and topological quantum computation. **Reviews of Modern Physics**, APS, v. 80, n. 3, p. 1083, 2008.

10 ALICEA, J. *et al.* Non-abelian statistics and topological quantum information processing in 1d wire networks. **Nature Physics**, Nature Publishing Group, v. 7, n. 5, p. 412–417, 2011.

11 BEENAKKER, C. Search for non-abelian majorana braiding statistics in superconductors. **SciPost Physics Lecture Notes**, p. 015, 2020.

12 KITAEV, A. Y. Fault-tolerant quantum computation by anyons. **Annals of Physics**, Elsevier, v. 303, n. 1, p. 2–30, 2003.

13 FREEDMAN, M. *et al.* Topological quantum computation. **Bulletin of the American Mathematical Society**, v. 40, n. 1, p. 31–38, 2003.

14 GENNES, P.-G. D.; PINCUS, P. A. **Superconductivity of metals and alloys**. Boca Raton: CRC Press, 2018.

15 POTTER, A. C.; LEE, P. A. Engineering a $p + ip$ superconductor: Comparison of topological insulator and rashba spin-orbit-coupled materials. **Physical Review B**, American Physical Society, v. 83, p. 184520, May 2011.

16 JACKIW, R.; REBBI, C. Solitons with fermion number ½. **Physical Review D**, American Physical Society, v. 13, p. 3398–3409, June 1976.

17 QI, X.-L.; ZHANG, S.-C. Topological insulators and superconductors. **Reviews of Modern Physics**, APS, v. 83, n. 4, p. 1057, 2011.

18 ALICEA, J. New directions in the pursuit of majorana fermions in solid state systems. **Reports on Progress in Physics**, IOP Publishing, v. 75, n. 7, p. 076501, 2012.

19 NELSON, K. *et al.* Odd-parity superconductivity in sr2ruo4. **Science**, American Association for the Advancement of Science, v. 306, n. 5699, p. 1151–1154, 2004.

20 KIDWINGIRA, F. *et al.* Dynamical superconducting order parameter domains in sr2ruo4. **Science**, American Association for the Advancement of Science, v. 314, n. 5803, p. 1267–1271, 2006.

21 XIA, J. *et al.* High resolution polar kerr effect measurements of $\mathrm{sr_2ruo_4}$: Evidence for broken time-reversal symmetry in the superconducting state. **Physical Review Letters**, American Physical Society, v. 97, p. 167002, Oct. 2006.

22 KASHIWAYA, S. *et al.* Edge states of $\mathrm{sr_2ruo_4}$ detected by in-plane tunneling spectroscopy. **Physical Review Letters**, American Physical Society, v. 107, p. 077003, Aug. 2011.

23 FU, L.; KANE, C. L. Superconducting proximity effect and majorana fermions at the surface of a topological insulator. **Physical Review Letters**, APS, v. 100, n. 9, p. 096407, 2008.

24 LIAN, B. *et al.* Topological quantum computation based on chiral majorana fermions. **Proceedings of the National Academy of Sciences**, National Academy Sciences, v. 115, n. 43, p. 10938–10942, 2018.

25 LUTCHYN, R. M.; SAU, J. D.; SARMA, S. D. Majorana fermions and a topological phase transition in semiconductor-superconductor heterostructures. **Physical Review Letters**, APS, v. 105, n. 7, p. 077001, 2010.

26 SAU, J. D. *et al.* Generic new platform for topological quantum computation using semiconductor heterostructures. **Physical Review Letters**, APS, v. 104, n. 4, p. 040502, 2010.

27 OREG, Y.; REFAEL, G.; OPPEN, F. V. Helical liquids and majorana bound states in quantum wires. **Physical Review Letters**, APS, v. 105, n. 17, p. 177002, 2010.

28 ALICEA, J. Majorana fermions in a tunable semiconductor device. **Physical Review B**, APS, v. 81, n. 12, p. 125318, 2010.

29 HSU, C.-H. *et al.* Majorana kramers pairs in higher-order topological insulators. **Physical Review Letters**, APS, v. 121, n. 19, p. 196801, 2018.

30 WANG, Y.; LIN, M.; HUGHES, T. L. Weak-pairing higher order topological superconductors. **Physical Review B**, American Physical Society, v. 98, p. 165144, Oct. 2018.

31 WU, Y.-J. *et al.* In-plane zeeman-field-induced majorana corner and hinge modes in an s-wave superconductor heterostructure. **Physical Review Letters**, American Physical Society, v. 124, p. 227001, June 2020.

32 YAN, Z.; SONG, F.; WANG, Z. Majorana corner modes in a high-temperature platform. **Physical Review Letters**, American Physical Society, v. 121, p. 096803, Aug. 2018.

33 ZHU, X. Tunable majorana corner states in a two-dimensional second-order topological superconductor induced by magnetic fields. **Physical Review B**, American Physical Society, v. 97, p. 205134, May 2018.

34 ZHANG, R.-X. *et al.* Higher-order topology and nodal topological superconductivity in fe(se,te) heterostructures. **Physical Review Letters**, American Physical Society, v. 123, p. 167001, Oct. 2019.

35 LIU, T.; HE, J. J.; NORI, F. Majorana corner states in a two-dimensional magnetic topological insulator on a high-temperature superconductor. **Physical Review B**, American Physical Society, v. 98, p. 245413, Dec. 2018.

36 YAN, Z. Majorana corner and hinge modes in second-order topological insulator/superconductor heterostructures. **Physical Review B**, American Physical Society, v. 100, p. 205406, Nov. 2019.

37 KHALAF, E. Higher-order topological insulators and superconductors protected by inversion symmetry. **Physical Review B**, American Physical Society, v. 97, p. 205136, May 2018.

38 GEIER, M. *et al.* Second-order topological insulators and superconductors with an order-two crystalline symmetry. **Physical Review B**, American Physical Society, v. 97, p. 205135, May 2018.

39 CHUNG, S. B. *et al.* Conductance and noise signatures of majorana backscattering. **Physical Review B**, APS, v. 83, n. 10, p. 100512, 2011.

40 BERNEVIG, B. A.; HUGHES, T. L.; ZHANG, S.-C. Quantum spin hall effect and topological phase transition in hgte quantum wells. **Science**, American Association for the Advancement of Science, v. 314, n. 5806, p. 1757–1761, 2006.

41 ZHANG, H. *et al.* Topological insulators in bi 2 se 3, bi 2 te 3 and sb 2 te 3 with a single dirac cone on the surface. **Nature Physics**, Nature Publishing Group, v. 5, n. 6, p. 438–442, 2009.

42 LIU, C.-X. *et al.* Model hamiltonian for topological insulators. **Physical Review B**, APS, v. 82, n. 4, p. 045122, 2010.

43 LIND, H.; LIDIN, S.; HÄUSSERMANN, U. Structure and bonding properties of $(\mathrm{Bi_2Se_3})_m(\mathrm{Bi_2})_n$ stacks by first-principles density functional theory. **Physical Review B**, American Physical Society, v. 72, p. 184101, Nov. 2005.

44 DRESSELHAUS, M. S.; DRESSELHAUS, G.; JORIO, A. **Applications of group theory to the physics of solids**. Berlin: Springer, 2008.

45 LEE, H.; YAZYEV, O. V. Interplay between spin–orbit coupling and crystal-field effect in topological insulators. **Journal of Physics:** condensed matter, IOP Publishing, v. 27, n. 28, p. 285801, 2015.

46 BERNEVIG, B. A. **Topological insulators and topological superconductors**. New Jersey: Princeton University Press, 2013.

47 SCHNYDER, A. P. *et al.* Classification of topological insulators and superconductors in three spatial dimensions. **Physical Review B**, American Physical Society, v. 78, p. 195125, Nov. 2008.

48 LU, H.-Z. *et al.* Massive dirac fermions and spin physics in an ultrathin film of topological insulator. **Physical Review B**, APS, v. 81, n. 11, p. 115407, 2010.

49 VIRTANEN, P.; RECHER, P. Signatures of rashba spin-orbit interaction in the superconducting proximity effect in helical luttinger liquids. **Physical Review B**, American Physical Society, v. 85, p. 035310, Jan. 2012.

50 SAU, J. D. *et al.* Robustness of majorana fermions in proximity-induced superconductors. **Physical Review B**, American Physical Society, v. 82, p. 094522, Sept. 2010.

51 STANESCU, T. D. *et al.* Proximity effect at the superconductor–topological insulator interface. **Physical Review B**, APS, v. 81, n. 24, p. 241310, 2010.

52 SHEN, S.-Q. **Topological insulators**: Dirac equation in condensed matter. Berlin: Springer, 2018.

53 KOGUT, J. B. The lattice gauge theory approach to quantum chromodynamics. **Reviews of Modern Physics**, APS, v. 55, n. 3, p. 775, 1983.

54 VAFEK, O.; VISHWANATH, A. Dirac fermions in solids: From high-t c cuprates and graphene to topological insulators and weyl semimetals. **Annual Review of Condensed Matter Physics**, Annual Reviews, v. 5, n. 1, p. 83–112, 2014.

55 ZHOU, Y.-F. *et al.* Two-dimensional lattice model for the surface states of topological insulators. **Physical Review B**, APS, v. 95, n. 24, p. 245137, 2017.

56 LI, H. *et al.* Manipulation of dirac band curvature and momentum-dependent g factor in a kagome magnet. **Nature Physics**, Nature Publishing Group, p. 1–6, 2022.

57 COHEN, M.; BLOUNT, E. The g-factor and de haas-van alphen effect of electrons in bismuth. **Philosophical Magazine**, Taylor & Francis, v. 5, n. 50, p. 115–126, 1960.

58 LIU, C.-X.; ZHANG, S.-C.; QI, X.-L. The quantum anomalous hall effect: theory and experiment. **Annual Review of Condensed Matter Physics**, Annual Reviews, v. 7, p. 301–321, 2016.

59 POURFATH, M. **The non-nquilibrium Green's function method for nanoscale device simulation**. Berlin: Springer, 2014. v. 3.

60 KELDYSH, L. V. *et al.* Diagram technique for nonequilibrium processes. **Soviet Physics JETP**, v. 20, n. 4, p. 1018–1026, 1965.

61 KADANOFF, L. P.; BAYM, G. **Quantum statistical mechanics**: Green's function methods in equilibrium and nonequilibrium problems. Boca Raton: CRC Press, 2018.

62 CHIU, C.-K. *et al.* Classification of topological quantum matter with symmetries. **Reviews of Modern Physics**, APS, v. 88, n. 3, p. 035005, 2016.

63 SHIOZAKI, K.; SATO, M. Topology of crystalline insulators and superconductors. **Physical Review B**, APS, v. 90, n. 16, p. 165114, 2014.

64 ARFKEN, G. B.; WEBER, H. J. **Mathematical methods for physicists**. Maryland: American Association of Physics Teachers, 1999.

65 SANCHO, M. P. L.; SANCHO, J. M. L.; RUBIO, J. Quick iterative scheme for the calculation of transfer matrices: application to mo (100). **Journal of Physics F:** metal physics, IOP Publishing, v.14, n. 5, p. 1205–1215, May 1984.

66 DANON, J.; FLENSBERG, K. Interaction effects on proximity-induced superconductivity in semiconducting nanowires. **Physical Review B**, APS, v. 91, n. 16, p. 165425, 2015.

67 DATTA, S. **Electronic transport in mesoscopic systems**. Cambridge: Cambridge University Press, 1997.

68 ANDREEV, A. The thermal conductivity of the intermediate state in superconductors. **Soviet Physics JETP**, v. 46, n. 5, p. 1823–1828, 1964.

69 BLONDER, G. E.; TINKHAM, M.; KLAPWIJK, T. M. Transition from metallic to tunneling regimes in superconducting microconstrictions: Excess current, charge imbalance, and supercurrent conversion. **Physical Review B**, American Physical Society, v. 25, p. 4515–4532, Apr. 1982.

70 SRIRAM, P. *et al.* Supercurrent interference in semiconductor nanowire josephson junctions. **Physical Review B**, APS, v. 100, n. 15, p. 155431, 2019.

71 SUN, Q.-f.; XIE, X. Quantum transport through a graphene nanoribbon–superconductor junction. **Journal of Physics**: condensed matter, IOP Publishing, v. 21, n. 34, p. 344204, 2009.

72 LEUMER, N. *et al.* Linear and nonlinear transport across a finite kitaev chain: An exact analytical study. **Physical Review B**, APS, v. 103, n. 16, p. 165432, 2021.

73 MEIR, Y.; WINGREEN, N. S. Landauer formula for the current through an interacting electron region. **Physical Review Letters**, American Physical Society, v. 68, p. 2512–2515, Apr. 1992.

74 STONE, M.; ROY, R. Edge modes, edge currents, and gauge invariance in p x+ i p y superfluids and superconductors. **Physical Review B**, APS, v. 69, n. 18, p. 184511, 2004.

75 LEUMER, N. *et al.* Exact eigenvectors and eigenvalues of the finite kitaev chain and its topological properties. **Journal of Physics:** condensed matter, IOP Publishing, v. 32, n. 44, p. 445502, 2020.

76 SARMA, S. D.; SAU, J. D.; STANESCU, T. D. Splitting of the zero-bias conductance peak as smoking gun evidence for the existence of the majorana mode in a superconductor-semiconductor nanowire. **Physical Review B**, American Physical Society, v. 86, p. 220506, Dec. 2012.

77 CHENG, M. *et al.* Splitting of majorana-fermion modes due to intervortex tunneling in a p x+ i p y superconductor. **Physical Review Letters**, APS, v. 103, n. 10, p. 107001, 2009.

78 STANESCU, T. D.; TEWARI, S. Spin polarization of majorana zero modes and topological quantum phase transition in semiconductor majorana nanowires. **Journal of the Indian Institute of Science**, v. 96, n. 2, p. 107–120, 2016.

79 LANDAUER, R. Spatial variation of currents and fields due to localized scatterers in metallic conduction. **IBM Journal of Research and Development**, IBM, v. 1, n. 3, p. 223–231, 1957.

80 QI, X.-L.; WU, Y.-S.; ZHANG, S.-C. Topological quantization of the spin hall effect in two-dimensional paramagnetic semiconductors. **Physical Review B**, APS, v. 74, n. 8, p. 085308, 2006.

APPENDIX A – EFFECTS OF A SUPERCONDUCTING LEAD ON DIRAC HAMILTONIANS

Here, we show that the effect of considering a superconducting layer in proximity to a material described by a Dirac Hamiltonian only induces an effective pairing $\tilde{\Delta}$ and a re-scale in the chemical potential and the Fermi velocity.

Let us consider a Dirac-like Hamiltonian $h(k) = \hbar v_F \vec{A} \cdot \vec{\sigma} - \mu$, where μ is the chemical potential, $\vec{\sigma} = (\sigma_x, \sigma_y, \sigma_z)$ is the Pauli matrices vector and represents spin 1/2 and $\vec{A}$ is a vector with linear dependence in momentum. We consider the region described by this Hamiltonian as the main region and couple it to an s-wave superconductor, which will appear as a self-energy

$$\Sigma_{SC}(\omega) = \frac{\xi}{\sqrt{\Delta^2 - \omega^2}} \left(-\omega\tau_0 + \Delta i \tau_y \right), \tag{A.1}$$

we recall that τ_i with $i = 0, x, y, z$ are the Pauli matrices acting on the Nambu space and that $\xi = |\gamma|^2 N(0)\pi$.

Therefore, the retarded Green's function is

$$\begin{aligned} G &= \left[\omega - h(k) - \Sigma_{SC}\right]^{-1}, & \text{(A.2)} \\ &= \left[\omega - h(k) - \frac{\xi}{\sqrt{\Delta^2 - \omega^2}} \left[-\omega\tau_0 + \Delta i \tau_y\right]\right]^{-1}, & \text{(A.3)} \end{aligned}$$

regrouping the ω term lead us to

$$G = \left[\omega \left(1 + \frac{\xi}{\sqrt{\Delta^2 - \omega^2}}\right) - h(k) - \frac{\xi}{\sqrt{\Delta^2 - \omega^2}} \Delta i \tau_y \right]^{-1}. \tag{A.4}$$

Now we do the re-scaling,

$$G = \left(1 + \frac{\xi}{\sqrt{\Delta^2 - \omega^2}}\right)^{-1} \left[\omega - \frac{h(k)}{\left(1 + \frac{\xi}{\sqrt{\Delta^2 - \omega^2}}\right)} - \frac{\xi}{\sqrt{\Delta^2 - \omega^2}} \frac{\Delta i \tau_y}{\left(1 + \frac{\xi}{\sqrt{\Delta^2 - \omega^2}}\right)}\right]^{-1}. \tag{A.5}$$

To have a compact equation, we defined $Z = \left(1 + \frac{\xi}{\sqrt{\Delta^2 - \omega^2}}\right)^{-1}$,

$$G = Z \left[\omega - Z\ h(k) - (1 - Z)\Delta i \tau_y\right]^{-1}. \tag{A.6}$$

If we now take the small-energy limit, $Z \to (1 + \xi/\Delta)^{-1}$, we find the results in Eq. 3.29, 3.30 and 3.31,

$$\begin{aligned} &Z\ h(k) \to (1 + \xi/\Delta)^{-1} (\hbar v_F \vec{A} \cdot \vec{\sigma} - \mu) \\ &= \hbar \tilde{v_F} \vec{A} \cdot \vec{\sigma} - \tilde{\mu} \end{aligned} \tag{A.7}$$

and

$$(1 - Z)\Delta \to \frac{\xi}{\frac{\xi}{\Delta} + 1} \equiv \tilde{\Delta} \tag{A.8}$$

APPENDIX B – TOTAL CHERN NUMBER

Here, we will show how to calculate the bulk topological invariant of our model. In order to simplify our expressions, we will make two simplifications: first, we will take the continuum limit of the lattice model $k_i a \approx 0$ and assume $a = W = \hbar v_F = 1$. With these considerations, our Hamiltonian reads

$$\begin{pmatrix} k_y\sigma_x - k_x\sigma_y + (m_z + k^2)\,\sigma_z - \mu & i\Delta\sigma_y \\ -i\Delta\sigma_y & k_y\sigma_x + k_x\sigma_y - (m_z + k^2)\,\sigma_z + \mu \end{pmatrix}. \tag{B.1}$$

Notice that now, our continuum model includes the effect of the Wilson mass term proportional to $k^2\sigma_z$, and hence the model does not have TRS and it is regularized (1). The latter feature will allow us to calculate a non-diverging total Chern number (17).

Before we (define and) calculate the Chern number, we change the basis of our Hamiltonian to $\frac{1}{\sqrt{2}}(\psi_{k\uparrow} + \psi^\dagger_{-k\downarrow}, \psi_{k\downarrow} + \psi^\dagger_{-k\uparrow}, -\psi_{k\uparrow} + \psi^\dagger_{-k\downarrow}, -\psi_{k\downarrow} + \psi^\dagger_{-k\uparrow})^T$, in which our Hamiltonian reads

$$\begin{pmatrix} k^2 + \Delta + m_z & -k_y - ik_x & 0 & \mu \\ -k_y + ik_x & -k^2 - \Delta - m_z & \mu & 0 \\ 0 & \mu & k^2 - \Delta + m_z & -k_y - ik_x \\ \mu & 0 & -k_y + ik_x & -k^2 + \Delta - m_z \end{pmatrix}. \tag{B.2}$$

Furthermore, we do a 90° rotation that will simplify our expression later on. This transformation is written as

$$U = \begin{pmatrix} e^{-i\frac{\pi}{4}\sigma_z} & 0 \\ 0 & e^{i\frac{\pi}{4}\sigma_z} \end{pmatrix}. \tag{B.3}$$

Using it, we transform our Hamiltonian into

$$\begin{pmatrix} \Delta + k^2 + m & k_x - ik_y & -\mu & 0 \\ k_x + ik_y & -\Delta - k^2 - m & 0 & -\mu \\ -\mu & 0 & -\Delta + k^2 + m & k_x - ik_y \\ 0 & -\mu & k_x + ik_y & \Delta - k^2 - m \end{pmatrix}. \tag{B.4}$$

Notice that for $\mu = 0$, our Hamiltonian becomes block diagonal and is equivalent to two copies of the QAH. The upper block with mass $(m_z + \Delta)$ and the lower one with $(m_z - \Delta)$.

In this particular case, we use that a given 2×2 diagonal block can be written as $d^i\sigma_i$ and define the normalized $\mathbf{d}$ vector $\hat{\mathbf{d}}$ to calculate the Chern number(80)

$$\mathcal{N} = \frac{1}{4\pi}\int\int dk_x dk_y \hat{\mathbf{d}} \cdot \partial_x\hat{\mathbf{d}} \times \partial_y\hat{\mathbf{d}}, \tag{B.5}$$

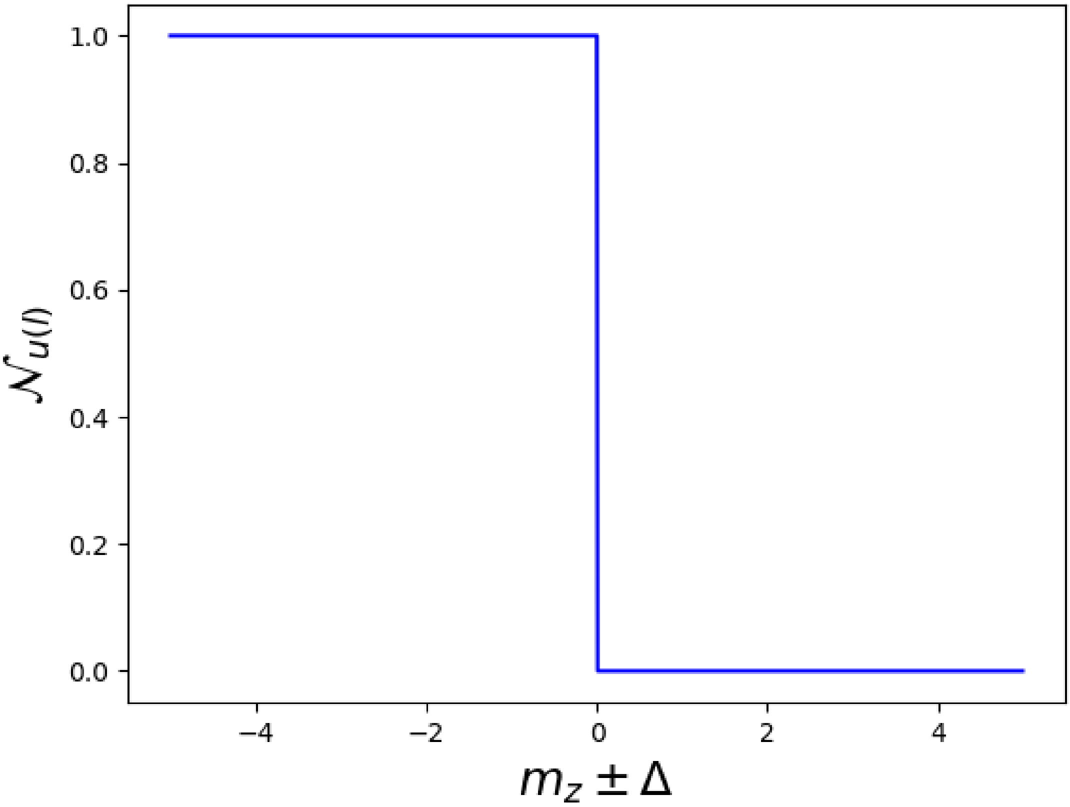

Figure 28 – Chern number calculated for the upper (lower) 2 × 2 diagonal block of the Hamiltonian. If the mass $m_z \pm \Delta$ is negative we have a non-trivial phase and the Chern number is 1. Source: by the author.

for the upper block and for the lower block and sum them to obtain the total Chern number. Note that this is valid only for $\mu = 0$ where the Hamiltonian assumes this block diagonal form. The general cases with $\mu \neq 0$ can be obtained through adiabatic connection, i.e., by changing parameters and looking at which regions of the parameter space (μ, m_z, Δ) are connected without passing through a gap closing.

Now we calculate the Chern number by identifying the vector $\mathbf{d} = (k_x, k_y, k^2 + (m_z \pm \Delta))$ for the upper (+) and lower (-) blocks,

$$\mathcal{N}_{u/l} = \frac{1}{4\pi} \int \int dk_x dk_y \frac{(m_z \pm \Delta) - k_x^2 - k_y^2}{\left[\left((m_z \pm \Delta) + k_x^2 + k_y^2\right)^2 + k_x^2 + k_y^2\right]^{3/2}}. \tag{B.6}$$

this integral gives us two possibilities (for each block), as we see in Fig. 28. Either $\mathcal{N}_{u(l)}$ is 0 or 1, depending on the sign of the mass gap of the block.

As we have two possibilities for each block, we have 3 possibilities for the total Chern number, which is the sum $\mathcal{N}_u + \mathcal{N}_l$ and each of these possibilities corresponds to a distinct topological phase with different edge states (when we consider an edge, i.e., a finite or semi-infinite geometry):

- 0, which happens for $m_z > 0$ and $|m_z| > |\Delta|$. This is the trivial phase and would not show edge states;
- 1, which happens when one of the blocks is trivial and the other one is not, i.e., $|\Delta| > |m_z|$. This phase would show a single propagating Majorana edge state;
- 2, when both N_u and N_l are 1. This occurs when $m_z < 0$ and $|m_z| > |\Delta|$ and would exhibit a pair of propagating Majorana edge modes, i.e. a pair of chiral Majoranas.

Note that for $\Delta = 0$, we have two copies (due to BdG) of the normal part of our Hamiltonian, which we know can be either in the QAH or trivial insulator phase. We obtain the QAH phase for $m_z < 0$ and the trivial phase for $m_z > 0$.

The classification above was a direct result of the calculation of the total Chern number. To study the general case with $\mu \neq 0$, we look at the behavior of the gap for different parameters in the continuum model. This gap analysis allows us to see which regions of the parameter space with $\mu = 0$ are adiabatically connected to the general case with $\mu \neq 0$. The results below are "summarized" as Fig. 14 in the main text.

As discussed in the main text, the equation $\mu^2 + \Delta^2 = m_z^2$ defines where the spectrum is gapless and separates different topological phases. When $\Delta = 0$, it is clear that for $|\mu| > |m|$ we have a metallic phase since the Fermi level is in one of the bulk bands. Otherwise, we have a QAH or trivial insulator phase, depending on the sign of m_z.

For $\Delta \neq 0$, we first look to the $\mathcal{N} = 1$ phase where $|\Delta| > |m_z|$. By adding a chemical potential we never make $\mu^2 + \Delta^2 = m_z^2$, as $|\Delta| > |m_z| \Rightarrow \mu^2 + \Delta^2 > m_z^2$. Note that changing the chemical potential will never make the gap close and reopen. Therefore the subspace where $|\Delta| > |m_z|$ and $\mu = 0$ can be adiabatically connected to the region where $\mu \neq 0$ and $|\Delta| > |m_z|$, i.e., the region where $|\Delta| > |m_z|$ and $\mu \neq 0$ is in the $\mathcal{N} = 1$ phase.

The other cases with $\Delta \neq 0$ occur for $|\Delta| < |m_z|$, the $\mathcal{N} = 2$ ($m_z < 0$) and the $\mathcal{N} = 0$ ($m_z > 0$) phases. In both cases $\Delta^2 < m_z^2$. If we consider $\mu \neq 0$, the gap will close at a critical value $|\mu_C| = \sqrt{m_z^2 - \Delta^2}$, such as $\mu_C^2 + \Delta^2 = m_z^2$, and reopen for chemical potentials with absolute value greater than $|\mu_C|$. Therefore, as long as we are below this critical value, i.e., $\mu^2 + \Delta^2 < m_z^2$, we can adiabatically connect the $\mu \neq 0$ region to $\mathcal{N} = 2$ (for $m_z < 0$) and to $\mathcal{N} = 0$ (for $m_z > 0$). Note that above $|\mu_C|$, we have $\mu^2 + \Delta^2 > m_z^2$ and we cross to the $\mathcal{N} = 1$ phase.